Hydrodynamics of Stirred Gas-Liquid Dispersions

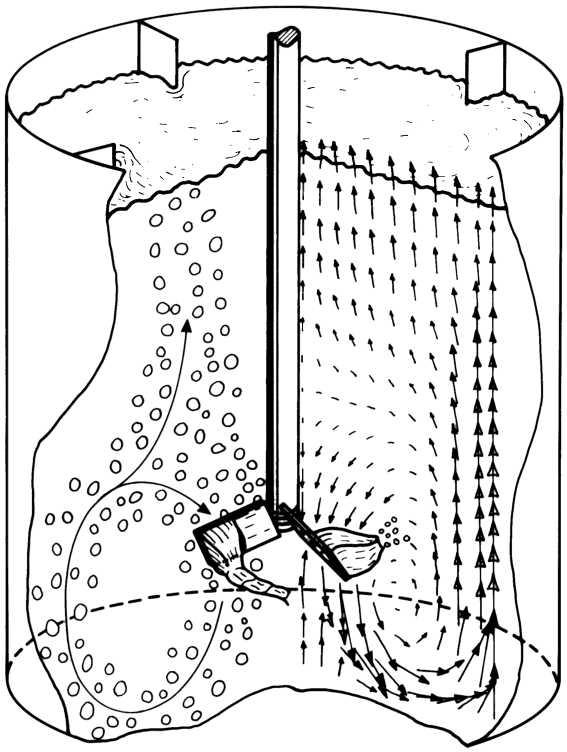

A. Bakker

1992

Foreword

This is the scanned version of my 1992 Ph.D. dissertation. The scan resolution has been kept relatively low to keep file size small. However, it should be possible to make easily readable prints.

This PDF file is available for download at my website titled “the Colorful Fluid Mixing Gallery” at http://www.bakker.org/cfm.

Compared to the original printed version, two typographical errors were corrected: one in figure 33 on page 42 and one in equation 17 on page 55.

Most of the material in this dissertation has also been published in the following three articles:

- Bakker A., Van den Akker H.E.A. (1994) *Gas-Liquid Contacting with Axial Flow Impellers*. Chemical Engineering Research and Design, TransIChemE Vol. 72, Number A4, July 1994, page 573-582.

- Bakker A., Van den Akker H.E.A. (1994) *Single-Phase Flow in Stirred Reactors.* Chemical Engineering Research and Design, TransIChemE Vol. 72, Number A4, July 1994, page 583-593.

- Bakker A., Van den Akker H.E.A. (1994) *A Computational Model for the Gas-Liquid Flow in Stirred Reactors.* Chemical Engineering Research and Design, TransIChemE Vol. 72, Number A4, July 1994, page 573-582.

For questions, I can be reached at the following e-mail address: ab@fluent.com.

Met vriendelijke groeten,

André Bakker
February 17, 2002

Hydrodynamics of Stirred

Gas-Liquid Dispersions

Hydrodynamics of Stirred

Gas-Liquid Dispersions

PROEFSCHRIFT

ter verkrijging van de graad van Doctor
aan de Technische Universiteit Delft,
op gezag van de Rector Magnificus,
prof. drs. P.A. Schenck, in het openbaar
te verdedigen ten overstaan van een
commissie aangewezen door het
College van Dekanen
op 17 februari 1992 te 14.00 uur
door

Andries Bakker

geboren op 24 september 1964 te Urk

Natuurkundig Ingenieur

Dit proefschrift is goedgekeurd door de promotor
prof.dr.ir. H.E.A. van den Akker

When citing from this thesis the following reference should be used:

A. Bakker, 1992
Hydrodynamics of Stirred Gas-Liquid Dispersions
Ph.D. Thesis, Delft University of Technology, The Netherlands

Kramers Laboratorium voor Fysische Technologie
Delft University of Technology
Prins Bernhardlaan 6
2628 BW, Delft, The Netherlands

Cover picture: Artist's impression, by A. Schinkel, of the flow pattern in a gassed stirred reactor equipped with a pitched blade turbine.

In der wetenschap geeft het niets rares!

Prof. Zbygniew Prlwytzkofski

CONTENTS

Chapter 4 - A Computational Model for the Gas-Liquid Flow in Stirred Reactors

Chapter 5 - Description of the Internal Structure of Stirred Gas-Liquid Dispersions

SAMENVATTING

Het onderzoek aan gas-vloeistof-menging in geroerde reactoren heeft zich lange tijd geconcentreerd op stromingsvisualisatie en op het meten van gemiddelde grootheden zoals het energieverbruik, de totale gasfraktie en de totale stofoverdracht. Hoewel zo ontwerpregels en stromingsdiagrammen opgesteld kunnen worden, is het moeilijk om fysisch inzicht te verkrijgen in de processen die zich in het gas-vloeistof-mengsel afspelen.

In het huidige onderzoek wordt de aandacht gericht op de stroming van het gas-vloeistof-mengsel, en de invloed van het stromingspatroon op de ruimtelijke verdeling van de afhankelijke grootheden, zoals de gasfraktie, de stofoverdracht, de belgrootte en de energiedissipatie. Zowel radiaal als axiaal pompende roerders zijn in het onderzoek betrokken.

In dit proefschrift worden eerst de stromingsregimes en de diverse soorten caviteiten beschreven, zoals deze zijn waargenomen bij axiaal pompende roerders. De meeste axiaal pompende roerders kennen drie hoofd-stromingspatronen. Bij lage gasdebieten is de stroming stabiel en symmetrisch. Bij toenemend gasdebiet ontstaan precesserende, asymmetrische stromingspatronen. Bij nog hogere gasdebieten kan de roerder het gas niet meer dispergeren en raakt "flooded". Diverse roerders en gasinlaten zijn vergeleken op basis van vermogensopname, gasfraktie en stofoverdracht. Zowel het roerdertype als de gasinlaat beïnvloeden de stofoverdracht.

Om een basis te hebben voor verder onderzoek aan het dispergeren van gas bij lage debieten, waarbij de gas-vloeistof stroming stabiel is, zijn de één-fase-stromingspatronen berekend. Dit is gedaan met het algemene stromingsprogramma FLUENT. Deze berekende stromingspatronen komen goed overeen met experimentele gegevens, vooropgesteld dat het juiste turbulentiemodel wordt gebruikt en dat de berekeningen gedaan worden op een drie-dimensionaal rooster. Deze één-fase-stromingen vertonen een aantal onverwachte en nog niet eerder gerapporteerde kenmerken. Vooral de preciese configuratie van de keerschotten is van belang. Op één-fase-stromingspatronen gebaseerde beschrijvingen van het mengproces kunnen dan ook alleen succesvol zijn indien het drie-dimensionale karakter van de stroming en de

inhomogeniteit van de turbulentie in de beschrijving betrokken worden.

Er is een rekenmodel opgesteld voor de stroming van het gas-vloeistof-mengsel bij lage gasdebieten. Op basis van dit model is een computercode ontwikkeld, genaamd GHOST! (Gas Holdup Simulation Tool!). GHOST! berekent lokale waarden van de belgrootte, de gasfraktie, de stofoverdracht op basis van balansvergelijkingen, een krachtenbalans op de bellen en de met FLUENT berekende één-fase-stromingspatronen. Verificatie van de berekeningen gebeurt aan de hand van met glasvezelprobes verkregen experimentele gegevens.

De experimentele gegevens en de berekeningen worden gecombineerd om zo een beeld te krijgen van de ruimtelijke verdeling van het gas, de belgrootte en de stofoverdracht. Met alle geteste roerders blijkt de ruimtelijke verdeling van het gas inhomogeen te zijn. Gebieden met veel gas en met weinig of geen gas liggen vaak vlak bij elkaar. De combinatie van deze inhomogene gasverdeling en inhomogene turbulentieverdeling leidt tot grote variaties in de lokale stofoverdracht. Pieken in de stofoverdracht zijn in de uitstroom van de roerder te vinden. De stofoverdracht in de gas-vloeistof bulk is daarentegen erg laag.

Het zal waarschijnlijk nooit mogelijk zijn om homogene gas- en turbulentieverdelingen te creëren. Bij pogingen om de stofoverdracht te verhogen zal men zich moeten richten op het aanpassen van de posities van de extremen in de ruimtelijke verdelingen van de afhankelijke grootheden. De combinatie van lokale metingen van belangrijke grootheden en numerieke stromingsberekeningen lijkt de enige methode om verder inzicht te krijgen in de processen die zich afspelen in een geroerde reactor.

SUMMARY

Research in the area of gas-liquid mixing in stirred vessels has for a long time concentrated on visual flow studies and on the measurement of overall properties such as the power consumption, the overall gas holdup and the overall mass transfer rate. Although design correlations and flow regime maps can be obtained in this way, it is difficult to gain insight in the basic mechanisms of the dispersion of gas in the gas-liquid bulk.

In the present work attention is focused on the description of the gas-liquid flow pattern and the effect of this flow pattern on the spatial variation of the dependent properties, as there are the gas holdup, the mass transfer rate, the bubble size and the energy dissipation rate. Both radial flow impellers and axial flow impellers are studied.

In this thesis a description of the flow regimes and cavity structures found with axial flow impellers is given first. It turns out that with most axial flow impellers three main flow regimes exist. At low gassing rates, stable symmetrical flow patterns are found. At increasing gassing rate precessing asymmetrical flow patterns can be observed. At still higher gassing rates the impeller is no longer capable of dispersing the gas and becomes flooded. Various impellers and gas spargers were compared on the basis of power consumption, overall gas holdup and overall mass transfer rate. It was found that both impeller type and gas sparger type can affect the overall mass transfer rate.

The single-phase flow patterns as induced by the impellers have been calculated to serve as a basis for further study on the gas dispersion process at low gas flow rates, when the gas-liquid flow is stable. This was done with the aid of the general fluid flow code FLUENT. Provided the right turbulence model is used and the computations are performed on fully three-dimensional grids, the predicted flow patterns compare well with own experimental data. It will be shown that the single-phase flow patterns exhibit unexpected features not reported on before. Especially the exact baffle configuration was found to have a strong impact on the flow pattern. Therefore it is concluded that descriptions of the mixing process based on single-phase flow patterns can only be successful if the three-dimensionality

of the flow and the inhomogeneity of the turbulence is taken into account.

A predictive model for the gas-liquid flow at low gas flow rates has been developed. On the basis of this model a code named GHOST! (Gas Holdup Simulation Tool!) has been written. GHOST! computes local and overall values of the bubble size, the gas holdup and the mass transfer rate on the basis of conservation equations, a force balance on the gas bubbles and the single-phase flow patterns as calculated with the aid of FLUENT. The predicted data are validated with own experimental data gathered with optical fiber probes.

The experimental data and the predicted gas distributions are combined to give a picture of the spatial distribution of the gas, the bubble size and the mass transfer rate. It turns out that with all impellers investigated the spatial gas distribution is far from homogeneous. Regions with a high gas holdup can exist close to regions with very little or no gas. The combination of this inhomogeneous gas distribution and the inhomogeneous turbulence distribution leads to wide variations in the local mass transfer rate. Peaks in the mass transfer rates are found in the outflow of the impellers. Very low mass transfer rates are found in the gas-liquid bulk.

As it is unlikely that it will ever become possible to create homogeneous gas and turbulence distributions in stirred vessels, it is concluded that further optimization of the mass transfer performance will have to concentrate on matching the positions of the extremes in the spatial distributions of the dependent quantities. The combination of local measurements of important quantities and Computational Fluid Dynamics seems to be the only method to gain further insight in the processes occurring in a stirred reactor.

CHAPTER 1

INTRODUCTION

1.1 HISTORY AND GOALS

The "Kramers Laboratorium voor Fysische Technologie" has got a long tradition in the research of stirred mixing vessels. Since the laboratory was set up in 1948 research has been done into various aspects of the operation of these types of chemical and biological reactors. In the early years work concentrated on the operation of mixing vessels for liquid-liquid mixing and extraction. Later on solids suspension and gas dispersion also received attention.

Especially gassed stirred vessels are known for their complex flow structure and the experimental difficulties in analyzing this type of flow. Because of these difficulties it was not until the 1970s that it was discovered that the gassed flow pattern is strongly influenced by the formation of gas filled cavities behind the impeller blades (van't Riet, 1975). This work later led to the development of flow regime maps for the design of gassed stirred tanks (Warmoeskerken, 1986). Until then most work had concentrated on the gas-dispersing characteristics of radial pumping impellers like the Rushton turbine. During the 1980s, however, several manufacturers developed axially pumping impellers with profiled blades. At the same time the Netherlands Organization for Applied Research (TNO) was working on the Leeuwrik impeller. The Leeuwrik impeller was meant to be a high-efficiency hydrofoil impeller which dispersed the gas from strong trailing vortices.

These new, profiled impellers were alleged to have several advantages, such as more homogeneous turbulence distributions, lower shear levels and higher mass transfer rates. Further, large improvements in bioreactor performance as a result of the use of these new impellers were reported.

These developments led to the initiation of the present research project (Smith and Warmoeskerken, 1985). Originally this project was intended to be

an experimental investigation into the performance of such profiled axial flow impellers, including the Leeuwrik impeller, in both single-phase flow systems and multi-phase flow reactors.

Soon after the project had been started in October 1987, it became clear that an experimental performance comparison of a large set of commercially available impellers would be of limited and temporary value if it would not lead to an increased understanding of the basic mechanisms of the gas dispersion process.

Furthermore, various new tools had become available for the analysis of single-phase and multi-phase flow systems. In the experimental sphere the knowledge of Laser Doppler Velocimetry (LDV) had reached a stage at which it could routinely be used in single-phase flows. Besides, a lot of progress was being made in the field of Computational Fluid Dynamics (CFD) (Colenbrander, 1989) and several fluid flow codes for single-phase flow computations had come on the market. For the analysis of gas dispersions optical fiber probes were being developed in the Kramers Laboratorium.

As a result of these circumstances it was decided to redefine the goals of this project. The first goal was to arrive at a qualitative description of the single-phase flow and the gas-liquid flow in stirred mixing vessels. The second goal was to develop predictive, quantitative models for these flows and the mass transfer rate.

1.2 ORGANIZATION OF THE THESIS

In Chapter 2 the results of an investigation of the gas-liquid hydrodynamics of stirred tanks equipped with (profiled) axial flow impellers are reported. Three different flow regimes are distinguished. Only at low gas flow rates, when the gas-liquid flow is dominated by the liquid flow pattern as induced by the impeller, the flow pattern is steady-state and the gas well-dispersed. The mass transfer performance of these axial flow impellers was compared with that of disc turbines, which, as already mentioned, have been the subject of extensive investigations in the past.

In Chapter 3 the results of a computational study on the single-phase flow with both radial pumping and axial pumping impellers are described. All computations were carried out with the commercially available fluid flow code FLUENT and the results were validated with experimental LDV data. These

single-phase flow patterns serve as a basis for further study of the gas dispersion process in those hydrodynamic regimes where the flow is stable.

Chapter 4 deals with the development of a predictive model for the gas-liquid flow in stirred vessels. This model is incorporated in a code named GHOST! (Gas Holdup Simulation Tool!) which calculates local values of gas holdup, bubble size and mass transfer rate on the basis of conservation equations and the single-phase flow patterns computed in Chapter 3. The computational results are validated against experimental data gathered with optical fiber probes.

Finally, in Chapter 5 a qualitative description is given of the spatial distribution of the gas holdup, the bubble size and the mass transfer rate in stirred mixing vessels. This description results from using a combination of experimental data and GHOST! results. Conclusions about further possible optimization of gassed stirred tanks are drawn.

In Appendix A a description of the mass transfer measurement method is given. In Appendix B the optical fiber probes for bubble measurements are described.

1.3 ACKNOWLEDGEMENTS

All investigations were financially supported by the Netherlands Technology Foundation (STW, project DTN 40.0566).

This work has profited of the large expansion of the computational facilities of the Kramers Laboratorium, which was made possible by a donation by Shell Nederland B.V. in 1989.

All the work was carried out at the Kramers Laboratorium voor Fysische Technologie, a subgroup of the Department of Applied Physics at Delft University of Technology. The assistance of the staff of this laboratory is highly appreciated.

Several students contributed to this thesis as part of their graduation work. Their names are Frank van Veen, Arie-Jan Stronkhorst and Marc Goedemans. Their contribution is gratefully acknowledged.

Further, I would like to express my gratitude to Jaap van Raamt for his enthusiastic assistance in the experimental part of this project.

CHAPTER 2

GAS-LIQUID CONTACTING WITH AXIAL FLOW IMPELLERS

ABSTRACT

This chapter focuses on the gas-dispersion characteristics of axial flow impellers. Various impellers are compared: an inclined blade impeller with flat blades, a Lightnin A315 impeller and a Leeuwrik impeller. The goal is to gain insight in the gas-dispersion properties of such axial flow impellers. Therefore the effects of impeller position and sparger geometry on flow pattern, power consumption and mass transfer are studied in a vessel being 0.444 m in diameter, using liquids of different viscosity.

The power consumption is strongly related to the different flow patterns and different types of cavities. Under certain conditions time-dependent, asymmetrical flow patterns can occur. The sparger type influences both the power needed to prevent flooding and the overall mass transfer coefficient k_la. The liquid viscosity does not affect the basic hydrodynamic phenomena in the vessel for viscosities not exceeding 80 mPas.

2.1 INTRODUCTION

Stirred reactors are often used for dispersing gases into liquids. Although traditionally many of these gas-liquid reactors are equipped with simple impellers like the radially pumping disc turbine, the development of so-called hydrofoil impellers has led to an increased interest in the use of axial flow impellers. In general, the manufacturers claim that at a given power input such modern hydrofoil impellers are capable of dispersing more gas and of yielding higher mass-transfer coefficients than traditional impellers. As data in the open literature about these hydrofoil impellers are scarce, it is difficult to assess these claims.

This chapter focuses on the gas-dispersion characteristics of axial flow impellers in general, and hydrofoil impellers in particular. Apart from a

simple pitched blade turbine (PBT), the so-called Leeuwrik impeller and the Lightnin A315 were tested (fig. 1). The goal was to gain insight in the gas-dispersion properties of such profiled and non-profiled axial flow impellers by linking power consumption and mass transfer to the flow pattern and the impeller hydrodynamics. Hence, the relation between flow pattern, power consumption and mass transfer have been studied in a vessel being 0.444 m in diameter using liquids of different viscosity and various sparger types.

2.2 LITERATURE

Because of the industrial importance of gas-liquid stirred vessels, their hydrodynamics has been the subject of extensive research (Nienow, 1990) and several reviews on this subject can be found in the literature (Smith, 1985, Joshi *et al.*, 1982, Nienow *et al.*, 1986). Especially the hydrodynamic properties of the radially pumping disc turbine have been investigated thoroughly. This has led to a proposal for improving the design by curving the blades (Warmoeskerken and Smith, 1989). The disc turbine is very effective in dispersing gas by breaking up the gas bubbles, but it has a relatively low hydraulic efficiency, which results in a low "flow per unit power". Further disadvantages of the disc turbine are the high levels of the shear stress in the vicinity of the impeller, a non-uniform distribution of energy dissipation rate in the vessel (Laufhütte and Mersmann, 1985) and a low gas-holdup in the lower part of the vessel (Mann and Hackett, 1988, Weetman, 1989, see also Chapter 5).

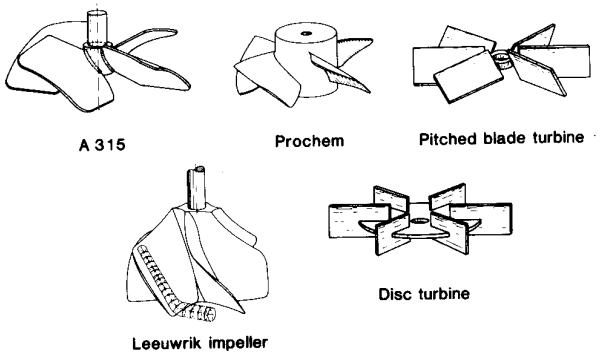

Figure 1 *Different impeller types.*

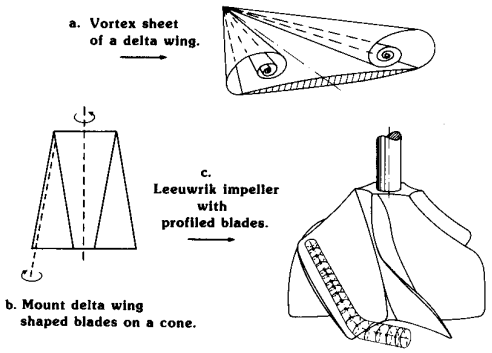

Figure 2 *The design of the Leeuwrik impeller.*

Therefore research is shifting towards the properties of axially pumping impellers which have a higher hydraulic efficiency and effect a more uniform distribution of energy dissipation rate in the vessel. These impellers further create lower levels of shear stress in the vicinity of the impeller. Axial flow impellers can be conveniently classified into two groups: simple impellers with flat inclined blades (pitched blade turbines), and so-called hydrofoil impellers with profiled blades. Examples of the latter are the Prochem hydrofoil and the Lightnin A315, both impellers looking very alike (fig. 1). Although axial flow impellers can be used pumping upwards, in this project they will only be studied in the downwards pumping mode.

During the present research project an inclined blade impeller, an A315 impeller and the Dutch Leeuwrik impeller were tested. The design of the Leeuwrik impeller was carried out by the Netherlands Organization for Applied Scientific Research TNO (Vermeulen and Pohlmann, 1980). This impeller is meant to create a large liquid flow as well as strong trailing vortices behind the impeller blades. The large flow should increase the homogeneity of the dispersion whereas the vortices should decrease the size of the recirculated bubbles. The plan form of the blades is based on the shape of a delta wing. Wings of this type yield a large lift and produce strong trailing vortices (fig. 2a). These delta wings are mounted on a hub (fig. 2b). Profiling the blades and adjusting the pitch gives the shape of the Leeuwrik impeller (fig. 2c). Bakker and Van den Akker (1990a) visualized the trailing vortex in the cavitation tunnel described by Van Oossaanen (1974) at the Department of Marine Engineering in Delft, see fig. 3.

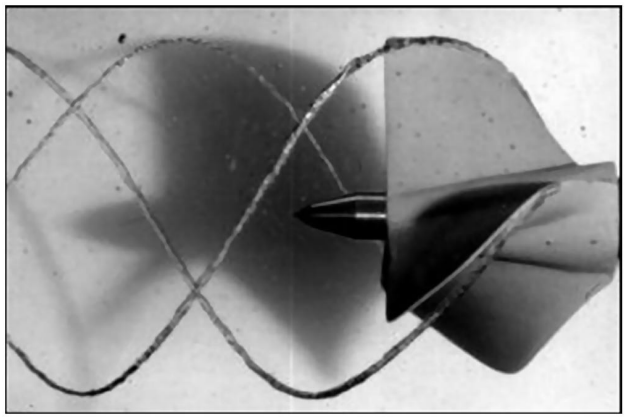

Figure 3 *The trailing vortex behind the blade of a three-bladed Leeuwrik impeller as visualized in the cavitation tunnel at the Department of Marine Engineering at Delft University of Technology. The vortex is filled with vapor.*

The use of pitched blade turbines and disc turbines for two-phase and three-phase mixing has been extensively discussed by Chapman *et al.* (1983a,b). These authors found that large torque fluctuations could occur when pitched blade turbines are used in the downwards pumping mode. Further they compared the gas-handling characteristics and power consumption of various impeller types.

Warmoeskerken *et al.* (1984) gave a description of the hydrodynamic properties and of the process of cavity formation with such pitched blade turbines (fig. 4).

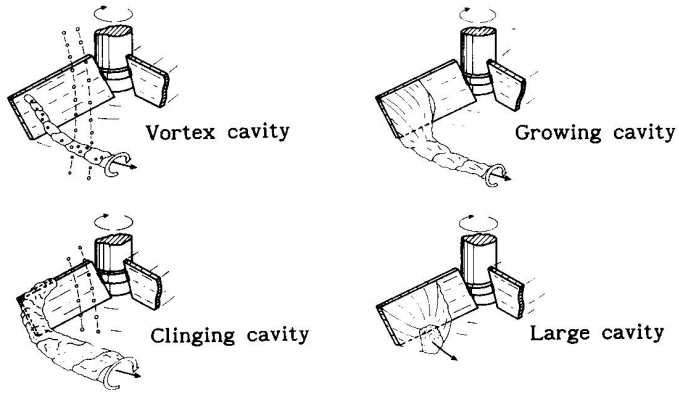

Figure 4 *The cavity formation process with pitched blade turbines (Warmoeskerken et al., 1984)*

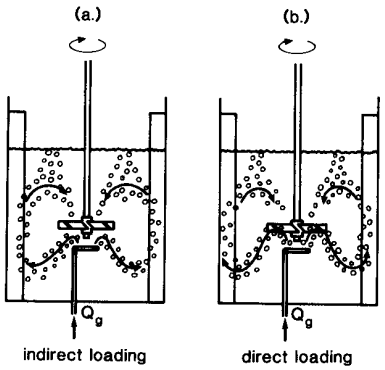

Figure 5 *Gas loading regimes (Warmoeskerken et al., 1984)*

They distinguished two gas loading regimes: indirect loading and direct loading (fig. 5). Indirect loading occurs when the gas is pumped downwards and enters the impeller only upon recirculation. At high gassing rates, however, the downward liquid flow will not be sufficiently strong to overcome and deflect the rising gas flow; hence the gas will rise directly into the impeller. This situation is called direct loading. These authors also reported that the mass transfer efficiency of a downwards pumping pitched blade turbine, based on the power demand, is at least as good as that of disc turbines.

Information about hydrofoil impellers in the open literature is relatively scarce. Oldshue *et al.* (1988) reported that the A315 is capable of dispersing 86% more air than a disc turbine at the same power input. In a water/air system mass transfer could be enhanced by 30% on the average by using an A315 system rather than a conventional disc turbine system. Later, Lally and Post (1991) reported a much smaller difference between the A315 and the disc turbine. According to their results an improvement of ± 5% in mass transfer rate can be achieved by using an A315 instead of a disc turbine. McFarlane (1989) studied the gassed flow pattern of the Prochem hydrofoil impeller. She found that instabilities occurred and that the gassed flow pattern could be asymmetrical, but gave no explanation for this observation.

Bakker and Van den Akker (1990a) compared a downwards pumping pitched blade turbine, a Lightnin A315 and a profiled Leeuwrik impeller on basis of pumping efficiency, gas handling capacity and mass transfer. They found that the A315 had the highest pumping efficiency and was the most energy efficient with respect to dispersing gas.

2.3 IMPELLER DESIGN CONSIDERATIONS

The impeller in a gassed stirred vessel has to meet several requirements. The ideal impeller would both effect a strong liquid flow with homogeneously distributed turbulence levels, create a homogeneous gas dispersion, and in the meantime break up the gas bubbles to increase the interfacial area. Since no impeller will be capable of meeting all these requirements, two main design strategies can be followed.

The first strategy leads to the design of radially pumping impellers like the disc turbine and the concave bladed turbine (Warmoeskerken and Smith, 1989). These impellers have got a relatively low pumping efficiency and create extremely large shear stresses in the impeller region. As a result of their flow pattern, all the gas sparged into the vessel enters the impeller before being dispersed in small bubbles. Although the liquid velocities effected by the disc turbine are relatively low and the turbulence distribution is far from homogeneous, the small bubble size created by the impeller leads to small bubble slip velocities. As a consequence the bubbles follow the main liquid flow relatively well, and significant levels of gas recirculation can be reached.

The second strategy is to try to increase the homogeneity of the gas dispersion and the mixing by increasing the liquid velocities and the turbulence levels in the liquid bulk. This can be done by designing an impeller with a high pumping efficiency. The pumping efficiency can be optimized by designing impellers with narrow profiled blades, like an air-wing. An example of such an impeller is the Lightnin A6000 impeller (Salzman *et al.*, 1988). Unfortunately, one of the problems with the use of such axially pumping impellers is that due to early cavity formation the pumping capacity will decrease with increasing gassing rate. Thus, for such impellers to be able to operate, the sensitivity for gassing has to be decreased. This can be done by increasing the so-called solidity ratio of the impeller, as with the Lightnin A315 impeller and the Prochem hydrofoil.

The often used solidity ratio SR (Oldshue, 1989) is defined as the total blade area $n_b A_b$ (!) divided by the area of the circle that encloses the projection in axial direction of the impeller onto a plane:

$$SR = \frac{n_b A_b}{\frac{\pi}{4} D^2} \qquad (1)$$

An impeller with a high solidity ratio is capable of operating at a high pressure loading, which is advantageous in gas-liquid systems and equally in high viscosity fluids.

The advantage of a high solidity ratio can be described in more detail by looking at the thrust F_T delivered by the impeller. The thrust F_T induces a mean circulatory flow through the vessel, the strength of which strongly depends on the flow resistance. This resistance results from the vessel geometry (D/T ratio, bottom profile, impeller-bottom clearance, baffle design etc.). Therefore the impeller has to overcome a pressure difference $\langle \Delta p_f \rangle$, which is proportional to the velocity head of the circulatory flow:

$$\langle \Delta p_f \rangle = K_w \, \tfrac{1}{2} \, \rho \, \langle v_{ax} \rangle^2 \tag{2}$$

To maintain this pressure difference the impeller must deliver a thrust F_T:

$$F_T = \tfrac{\pi}{4} \, (D^2 - d_{hub}^{\,2}) \, \langle \Delta p_f \rangle \tag{3}$$

In addition, the thrust F_T is proportional to the thrust loading, $\langle \Delta p_b \rangle$, being the average pressure increase over the impeller blades from suction side to pressure side. Hence:

$$F_T = n_b \, A_{b,\perp} \langle \Delta p_b \rangle \tag{4}$$

Here $A_{b,\perp}$ denotes the projected area of one blade. Combining equations (2), (3) and (4) results in:

$$\langle \Delta p_b \rangle = \frac{F_T}{n_b \, A_{b,\perp}} = K_w \, \tfrac{1}{2} \, \rho \, \langle v_{ax} \rangle^2 \, \frac{\tfrac{\pi}{4} \, (D^2 - d_{hub}^{\,2})}{n_b \, A_{b,\perp}} \tag{5}$$

It is necessary to keep $\langle \Delta p_b \rangle$ as low as possible for two reasons. The first reason is that at a low $\langle \Delta p_b \rangle$ stalling will occur less easily. Stalling is the loss of pumping capacity due to separation of the boundary layer at the suction side of the impeller blade. The second reason is that due to the lower pressure at the suction side of the impeller blade, gas will accumulate there and this will eventually lead to the formation of large gas filled cavities and consequently to loss of pumping capacity. In case of a low $\langle \Delta p_b \rangle$ this will occur less easily and the impeller pumping capacity will be

less dependent on the gassing rate. It will therefore be clear from eq. (5) that a high projected blade area ratio $R_{b,\perp}$

$$R_{b,\perp} = \frac{n_b A_{b,\perp}}{\frac{\pi}{4}(D^2 - d_{hub}^2)} \tag{6}$$

will increase the performance of the system. This roughly corresponds with increasing the solidity ratio. The advantage of a large $R_{b,\perp}$ is confirmed by the fact that it has repeatedly been found that pitched blade turbines in gassed systems perform better when the number of blades is increased. Frijlink *et al.* (1990), for example, found that six bladed inclined blade turbines performed better with respect to suspending solids in gassed systems than four bladed impellers.

Note that the projected blade area ratio is not the only parameter affecting cavity formation and stalling and that these processes will also depend on the shape of the impeller blades.

The values for the solidity ratio, $R_{b,\perp}$ and the number of blades are listed in table 1, together with the impeller power number:

$$Po = \frac{P}{\rho N^3 D^5} \tag{7}$$

and the impeller pumping number:

$$Fl_l = \frac{Q_l}{N D^3} \tag{8}$$

Here P is the power consumption of the impeller and Q_l is the liquid flow rate through the impeller. It can be seen that the Leeuwrik impeller has by far the largest solidity ratio, but that the difference in blade area ratio between the A315 and the Leeuwrik is only small. The impeller pumping number is calculated from LDV data (Chapter 3). No correlation between SR or $R_{b,\perp}$ and Po or Fl is found.

Table 1 *Solidity ratio, blade area ratio and other details.*

Impeller	SR	$R_{b,\perp}$	n_b	D(m)	Po	Fl_l
A315	90%	77%	4	0.178	0.76	0.74
LS6	160%	80%	6	0.168	2.55	-
PBT	60%	45%	6	0.176	1.55	0.81

2.4 EXPERIMENTAL SET-UP

A flat-bottomed perspex vessel of diameter T = 0.444 m was used in all experiments. The vessel was equipped with four baffles (width W = 0.077 T, mounted at a distance 0.023 T from the wall). The liquid height H was equal to the tank diameter T. Experiments were done with distilled water and glycerol solutions of viscosities η = 36 mPas (ρ = 1190 kgm^{-3}) and η = 80 mPas (ρ = 1220 kgm^{-3}). The diameter of the impellers was D = 0.4 T. The impellers were placed either at a distance C = $\frac{3}{4}$ D or a distance C = D from the vessel bottom. The blade width for the pitched blade turbine was B_w = 0.2 D.

The power demand was calculated from the impeller rotational speed and the torque exerted by the impeller. The torque was determined with a Vibro-torque transducer mounted in the shaft. The overall gas-holdup could be determined with an ultrasonic liquid level meter. A few solids suspension experiments were carried out, in which the minimum power consumption necessary for the suspension of 1 mass% solids was determined according to the 1-second criterion (Zwietering, 1958).

Several spargers were tested: a pipe sparger (PS), a small ring sparger (SRS, d_s = 0.4 D), a large ring sparger (LRS, d_s = 0.75 D) and a quadruple pipe sparger (QPS). The QPS was configured to the design of Weetman (1989). The distance between the ring spargers and the impeller could be varied. A schematic view of the spargers and the vessel is shown in figures 6 and 7.

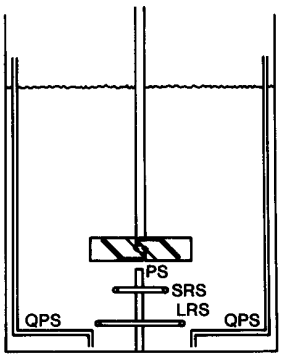

Figure 6 *The four investigated sparger types, a pipe sparger (PS), a small ring sparger (SRS), a large ring sparger (LRS) and a quadruple pipe sparger (QPS).*

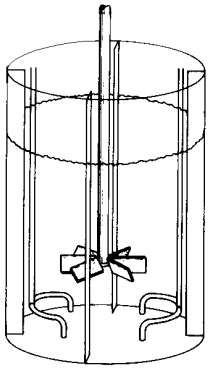

Figure 7 *The quadruple pipe sparger.*

The mass transfer coefficient $k_l a$ was determined using a dynamic measurement method, assuming perfect mixing in the gas-phase (appendix A). The experiments were performed in distilled water. The superficial gas velocity was v_{sg} = 0.01 m/s. The mass transfer experiments reported in this chapter were performed with the impeller mounted at a clearance C/D = 0.75.

2.5 HYDRODYNAMICS

2.5.1 The Gassed Flow Pattern and Impeller Hydrodynamics

In this section, first the experiments performed with water will be reported and later the influence of an increase in viscosity will be discussed.

The gassed flow pattern as a function of impeller speed and of gassing rate has been studied visually. Further, the process of cavity formation has been photographed. This has been done for all three impellers investigated. It turned out that the characteristics of the pitched blade turbine and the A315 impeller are very similar, but that the flow patterns found with the Leeuwrik impeller are quite different. So, first the characteristics of the A315 will be discussed, and then they will be compared with the Leeuwrik impeller.

The results for the A315 are illustrated in figure 8. At low gassing rates and/or high impeller speeds, the gassed flow pattern is symmetrical. Gas reaches the impeller only due to recirculation (indirect loading) and vortex cavities are formed (fig. 8A). If the impeller speed is decreased, or the gassing rate increased, the gas is still pumped downwards (indirect loading) but the impeller is not capable anymore of recirculating all the gas, the gas escapes from the vessel on one side in a large gas cloud while on the other side the gas is recirculated in a small loop. As a result the flow pattern is asymmetrical and the gas cloud can be seen precessing through the vessel with a period between approximately 1 and 30 minutes, depending on exact sparger geometry, gassing rate and impeller speed. In this situation growing cavities are formed (figure 8B).

At still higher gassing rates the impeller is not capable of deflecting the rising gas flow and gas rises into the impeller directly (direct loading). In this situation large cavities are formed (figure 8C) and the flow pattern is dominated by the rising gas flow rather than by the impeller. This situation can also be called flooding. The transitions between the flow

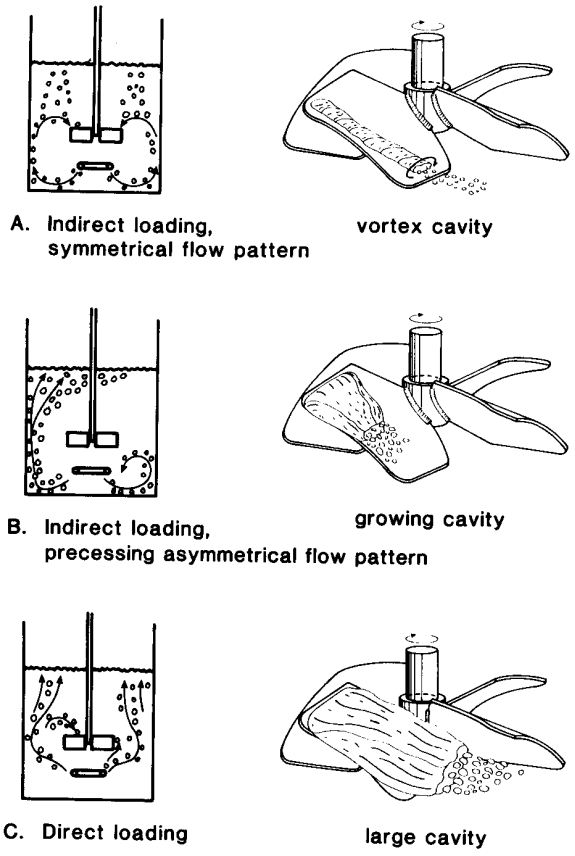

Figure 8 *The cavity formation process and the flow regimes for the A315.*

patterns are not sharp and often give rise to oscillations. Especially the indirect loading to direct loading transition was found to result in large torque fluctuations. This has already been observed for pitched blade turbines by Chapman *et al.* (1983a).

In general the different flow patterns and hydrodynamic regimes of the A315 and the inclined blade impeller are very alike. The asymmetrical flow pattern was also found with the inclined blade impeller, which has not been reported before in the literature. The clinging cavities which are formed with the inclined blade impeller (Warmoeskerken *et al.*, 1984) were not observed with the A315. This may be an indication that the vortices formed at the blade edges are stronger with the PBT than with the A315.

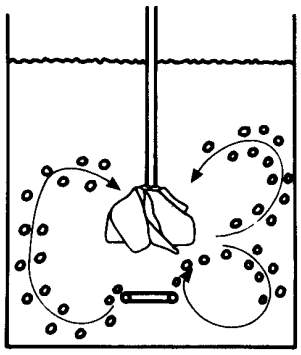

Figure 9 *The two operating modes of the Leeuwrik impeller, axially pumping (left) and radially pumping (right).*

The Leeuwrik impeller turns out to have two modes of operation: axially pumping and radially pumping, see fig. 9. At low gassing rates this impeller creates an axial flow pattern and vortex cavities are formed. At increasing gassing rates large cavities are formed and the flow pattern switches from a pure axial flow to a pure radial flow, like with the disc turbine. This transition is very sharp. Thus the Leeuwrik impeller differs from the PBT and the A315. With the latter two impellers the pumping capacity decreases on gassing, but they maintain an axial flow pattern as opposed to the Leeuwrik impeller which is has more stable operation modes.

2.5.2 The Asymmetrical Flow Pattern

The precessing asymmetrical flow pattern depicted in figure 8B is quite interesting. Such asymmetries were already observed for other hydrofoil impellers (McFarlane, 1989) and can also be seen with pitched blade turbines. Further, these time dependent asymmetries have been observed on an industrial scale in the gold cyanidation process (Koen, 1990). This suggests that these asymmetries are inherent to a lot of systems equipped with single axial flow impellers.

The asymmetrical flow pattern consists of a gas cloud rising up on one side of the vessel, and a short gas circulation loop on the other side of the vessel. Further, different types of vortices can be observed (figure 10). The gas cloud is either stable, and stays on one side of the vessel, or it

precesses slowly around the vessel. For the PBT the direction of precession was always equal to the direction of rotation of the impeller. In contrast, for the A315 the direction of precession was often opposite to the direction of rotation of the impeller.

The mechanism behind the precessing motion is still unclear, especially for those cases where the direction of precession is opposite to the direction of rotation of the impeller. Bakker and Van den Akker (1990b) suggested a mechanism for those cases where the impeller rotational direction and the precessing direction are the same.

This mechanism can be described in detail with the help of the sketch in figure 10. It is essential to understand that in a vessel equipped with an axial flow impeller two opposite kinds of vortex motion are interacting. The impeller induces both a tangential flow and an axial flow. Due to the tangential flow, vertical vortices are formed behind the baffles. On the other hand, the axial flow generates horizontal vortices lying near to the vessel bottom. The interaction between these horizontal and vertical vortices may lead to instabilities and an asymmetrical flow condition, depending on the ratio of the strength of the main, axial flow and the strength of the secondary, tangential flow.

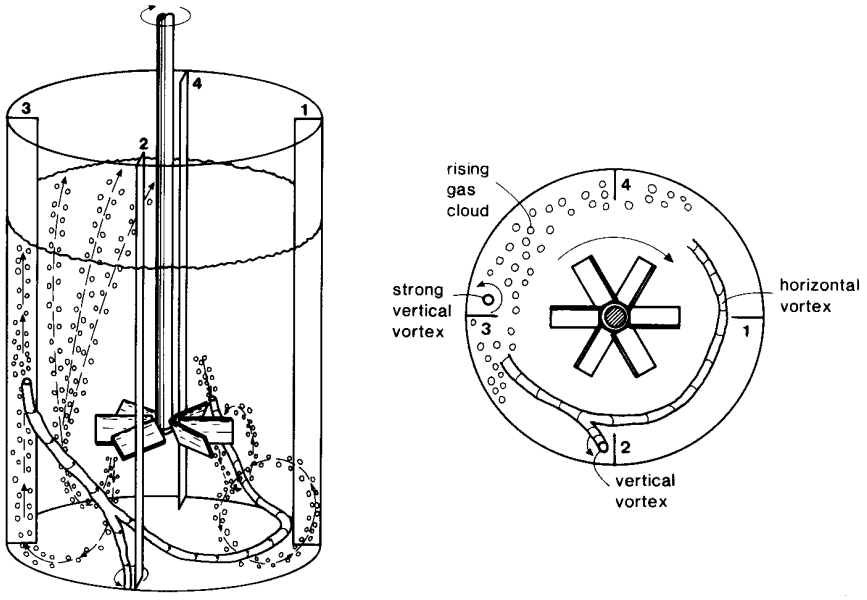

Figure 10 *The vortex system and the precessing asymmetrical flow pattern.*

At low gassing rates the impeller acts as an efficient pump and the flow pattern in the vessel is dominated by the axial flow, and the associated circulation loops with the horizontal vortex in the center. Under these conditions instabilities may not get the opportunity to grow. At increasing gassing rate the pumping efficiency of the impeller decreases due to cavity formation: the strength of the axial flow induced by the impeller decreases faster than the strength of the tangential flow. At the same time, the momentum of the gas entering the vessel increases. The rising gas flow disturbs the recirculation loops and promotes and strengthens the long vertical vortices induced by the tangential flow. These effects together lead to the asymmetrical flow pattern depicted in figure 10.

In this case the horizontal vortex caused by the axial flow lies near the bottom in front of baffle 1. Behind baffle 2 a vertical vortex is formed which bends sideways and joins with the horizontal vortex. Due to both the rising gas flow and the tangential flow caused by the impeller a strong vertical vortex is created behind baffle 3. The gas leaves the vessel in a cloud which roughly lies between baffle 3 and 4. There is no tangential vortex to be seen behind baffle 4 since the direction of rotation of this would-be vortex is opposed by the horizontal vortex in front of baffle 1. Due to the tangential motion induced by the impeller the diagonal vortex between baffle 2 and 3 is gradually bending more horizontal, towards baffle 3. At the same time the gas cloud from baffle 3 to 4 shifts gradually in the direction of baffle 4 to baffle 1 and the vertical vortex behind baffle 3 also bends

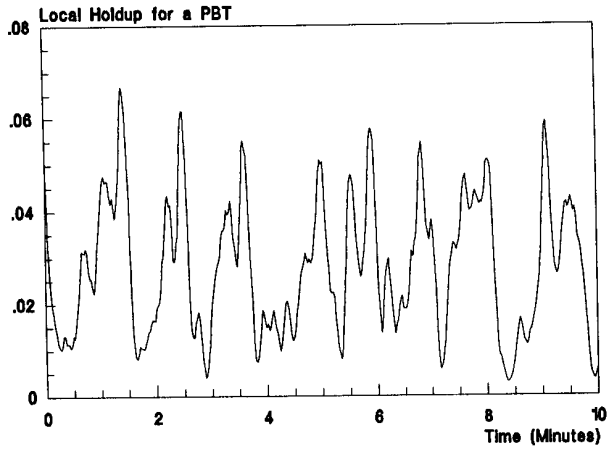

Figure 11 *Time dependent local gas holdup with the pitched blade turbine (N = 5 Hz, v_{sg} = 0.0067 m/s, 2r/T = 0.7, z/H = 0.6)*

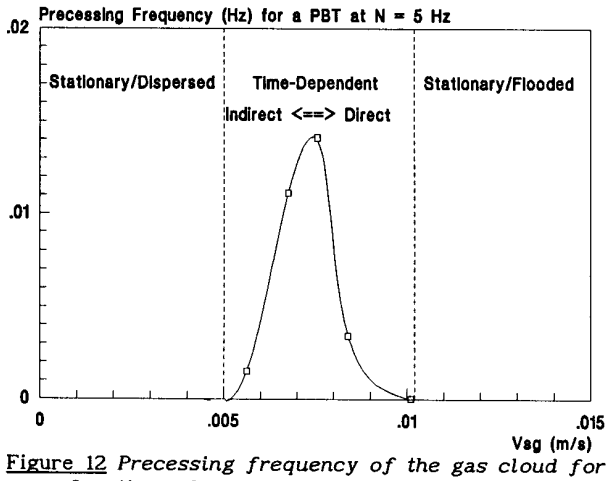

Figure 12 *Precessing frequency of the gas cloud for the pitched blade turbine as a function of superficial gas velocity.*

gradually in the direction of baffle 4. Due to the fact that now a small vertical vortex behind baffle 4 is formed since more gas is rising up there the horizontal vortex in front of baffle 1 moves towards baffle 2, and joins with the vertical vortex behind baffle 3. As a consequence the whole flow pattern, including the rising gas cloud and the horizontal/vertical vortex system, slowly precesses in the direction of rotation of the impeller.

The period of precession depends on gassing rate, impeller speed, power consumption and sparger position. Typical values range from one minute to thirty minutes. To investigate these phenomena further, the local gas holdup at $2r/T = 0.7$ and $z/H = 0.6$ has been measured with an optical fiber probe (appendix B) in the plane midway between the baffles. A typical signal is shown in figure 11. It can be seen that there is a strong fluctuation in the local gas holdup as a result of the periodicity in the flow pattern. The precessing frequency has been calculated from the holdup signals with the aid of Fast Fourier Transforms. Figure 12 shows the precessing frequency of the gas cloud for a pitched blade turbine (PBT) as a function of superficial gas velocity at a constant impeller speed. It can be seen that three regimes can be distinguished, steady-state and dispersed, low frequency time-dependent, and steady state and flooded. The highest precessing frequency is found near the indirect loading to direct loading transition.

These are preliminary results and a lot of questions regarding these time-dependent flow patterns remain to be answered. Therefore these phenomena will be the subject of further study.

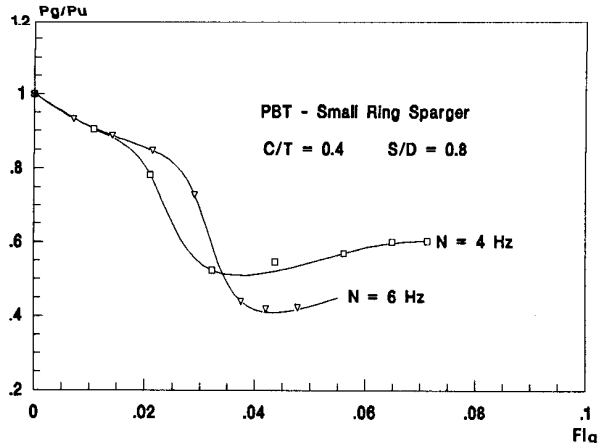

Figure 13 *Power curves for the PBT at constant impeller speed.*

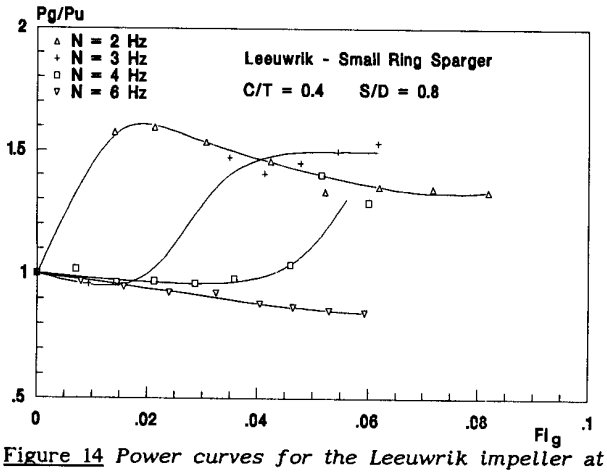

Figure 14 *Power curves for the Leeuwrik impeller at constant impeller speed.*

2.5.3 The Link with Power Consumption

The effect of gassing on power consumption is the direct result of changes in the impeller hydrodynamics and the flow patterns as discussed above, and can be illustrated by the P_g/P_u vs. Fl_g curves for different impeller speeds.

Figure 13 shows the P_g/P_u curves at constant impeller speeds for the PBT. With the PBT the power consumption shows a steep decrease, which was visually found to be related to the indirect to direct loading transition, at a gas flow number Fl_g between 0.02 and 0.04, depending on impeller speed. The Leeuwrik impeller on the other hand, shows an increase in power consumption at this transition due to the switch from a pure axial flow to a pure radial flow (fig. 14).

Figure 15 shows the P_g/P_u curve at a constant impeller speed of N = 5 s^{-1} for the A315. The different regions in this curve correspond with the three different flow patterns and the different types of cavities described before (see also figure 8). As with the PBT, the formation of large cavities at the indirect/direct loading transition corresponds with a strong drop in power consumption, see also fig. 16.

The curves of the gassed power number Po_g vs. gas flow number Fl_g at a constant superficial gas velocity look quite different. Figure 17 shows the gassed power at three different superficial gas velocities for the PBT with a large ring sparger. When at a certain gassing rate the impeller speed is increased, starting from a low speed (high Fl_g), Po_g decreases until a minimum is reached, probably due to an increase in cavity size. This minimum corresponds with the indirect/direct loading transition. After the large cavities have disappeared at this critical flow number $Fl_{g,c}$, corresponding

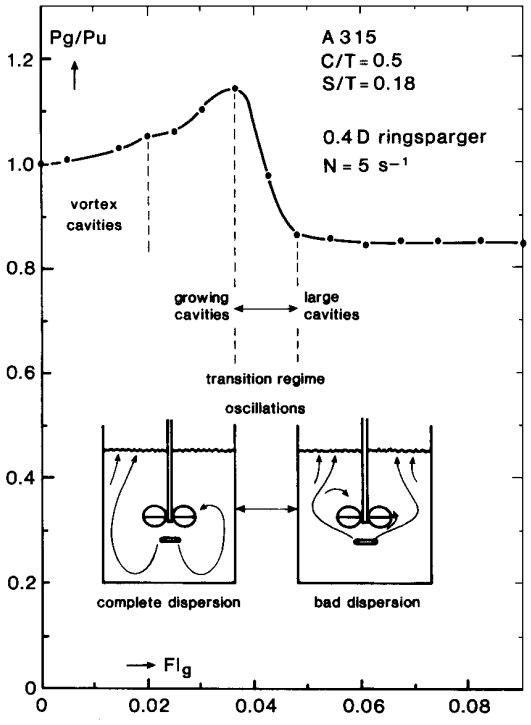

Figure 15 *The relation between the gassed power consumption, the gassed flow pattern and the cavity formation process.*

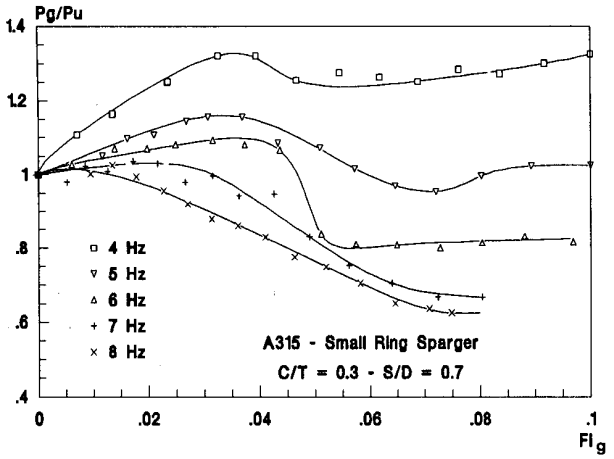

Figure 16 *Power curves for the A315 at constant impeller speed.*

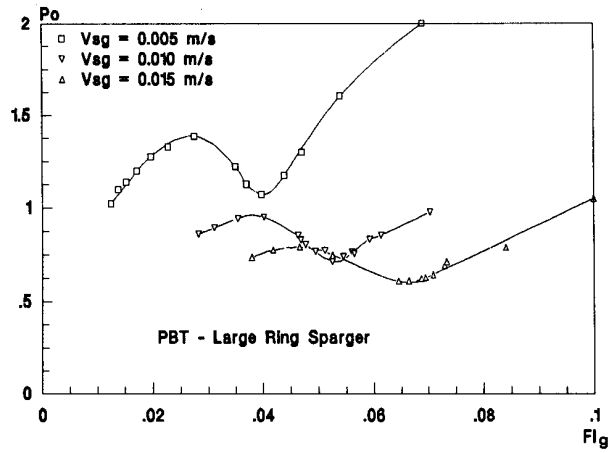

Figure 17 *Power curves for the PBT at constant superficial gas velocity.*

with a critical specific power consumption $\langle \varepsilon_c \rangle = P_c/V_l$, the power number increases at increasing impeller speed until a maximum is reached. When the impeller speed is increased even further Po_g decreases again, due to an increase in gas recirculation. The power curves for the A315 are very much similar to those of the PBT (fig. 18) although the transitions are less pronounced. When the quadruple pipe sparger is used the regime transitions are even smoother (fig. 19).

In general it can be concluded that the gassed power consumption depends both on the impeller type and sparger configuration, due to differences in the induced flow patterns and cavity structures.

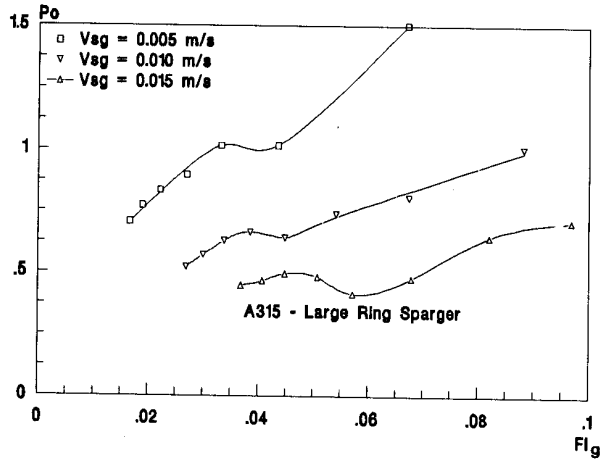

Figure 18 *Power curves for the A315 at constant superficial gas velocity (large ring sparger).*

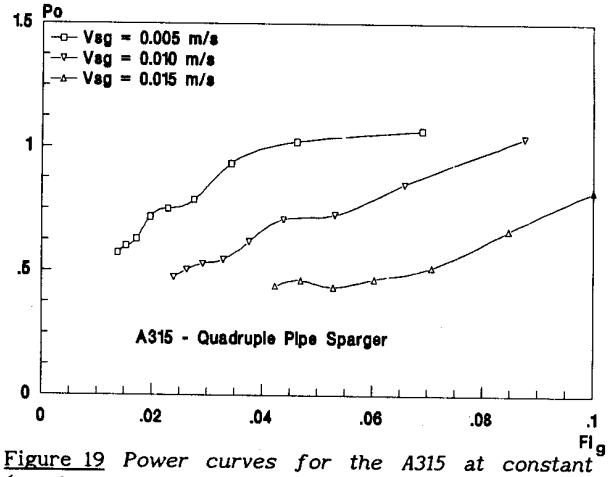

Figure 19 *Power curves for the A315 at constant superficial gas velocity (quadruple pipe sparger).*

2.5.4 Influence of Impeller Type

The impellers are compared on basis of the minimum power consumption necessary for full gas dispersion $\langle \varepsilon_c \rangle = P_c/V_l$, and on the minimum power consumption $\langle \varepsilon_{jsg} \rangle$ necessary to suspend 1 mass% of solids.

Figure 20 shows $\langle \varepsilon_c \rangle$ for all three impellers compared as a function of v_{sg}. It can be seen that the Leeuwrik impeller has the worst performance: the axial-radial flow transition occurs relatively early. At v_{sg} = 0.005 m/s the difference between the PBT and the A315 is small, but at higher gassing rates

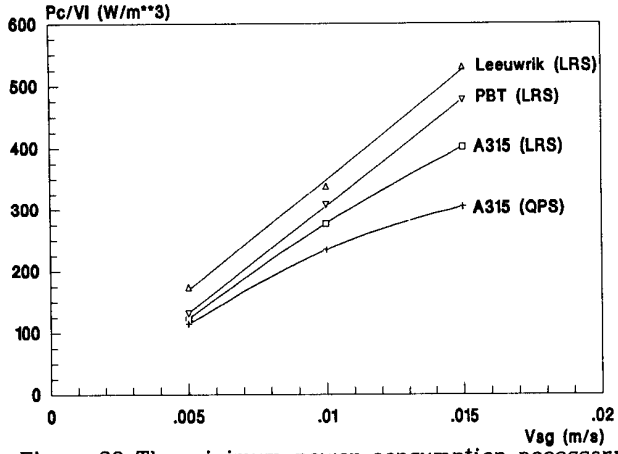

Figure 20 *The minimum power consumption necessary to prevent direct loading.*

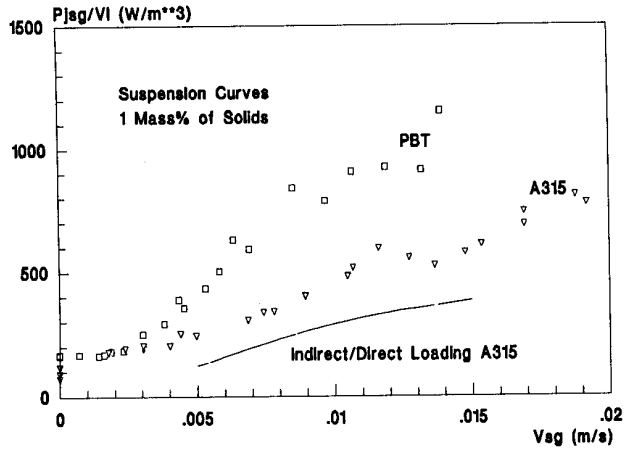

Figure 21 *The minimum power consumption necessary to suspend 1 mass% of solids (density is 2500 kgm^{-3}, particle diameter is 0.1 mm). The line indicates the indirect to direct loading transition for the A315.*

the A315 gives a better performance. This may be due to the fact that the A315 is capable of maintaining a stronger liquid flow at high gassing rates than the pitched blade turbine.

This can be verified by inspection of the suspension curves of the impellers. Since suspension is a flow controlled process, suspension experiments with low solids concentrations can be used as a measure of the strength of the liquid flow. Fig. 21 shows $\langle \varepsilon_{jsg} \rangle$ as a function of v_{sg}. At low gassing rates there is no significant difference to be found between the PBT and the A315, but at high gassing rates the A315 gives the best performance. This means that under gassed conditions the A315 needs less

energy to create a certain liquid flow than the pitched blade turbine. The line drawn in the graph indicates the indirect to direct loading transition for the A315. It can be seen that for full solids suspension it is necessary that the impeller is operated in the indirect loading regime, and in fact that full solids suspension is a more strict demand than full gas dispersion.

2.5.5 The Effect of Sparger Configuration

The performance of various spargers has been tested with the A315 and the PBT with water. Since the results were very much similar, the main conclusions will be illustrated with the A315 data only. Fig. 22 shows a comparison between the power curves for the small ring sparger (SRS) and the pipe sparger (PS). It is clear that the power drop in the curves occurs earlier for the pipe sparger than for the ring sparger. This means that with the ring sparger less power is needed for dispersing a certain amount of gas.

Fig. 23 shows the effect of impeller to sparger separation distance S. When this distance is increased the power drop takes place at a higher gassing rate. Again this means that with respect to the power needed to disperse a certain amount of gas a large separation distance is beneficial.

Figure 24 shows a comparison between the small ring sparger and the large ring sparger (LRS) for a liquid viscosity of η = 36 mPas. The steepest power drop occurs for the smaller ring sparger and the smaller separation distance. The minimum power consumption $<\varepsilon_c>$ necessary for preventing the impeller from flooding has been determined as a function of gassing rate for

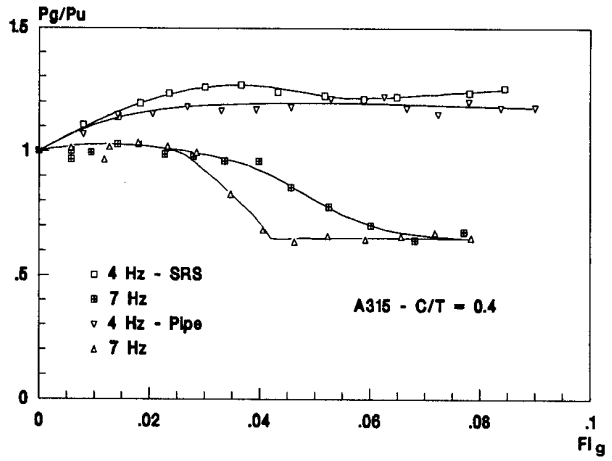

Figure 22 *Power curves for the A315 with a small ring sparger and a pipe sparger at constant impeller speed.*

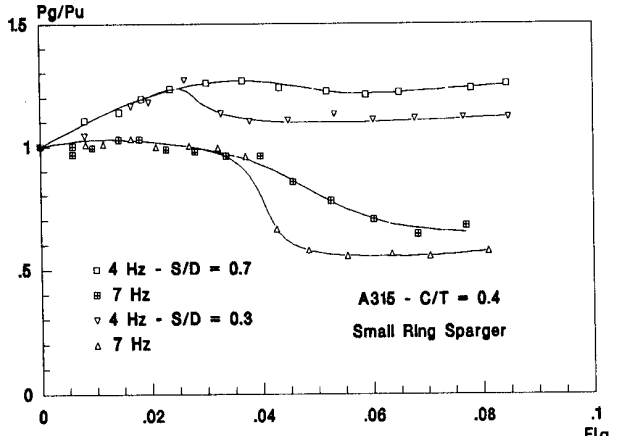

Figure 23 *Power curves for the A315, small ring sparger, two impeller to sparger separation distances, constant impeller speed.*

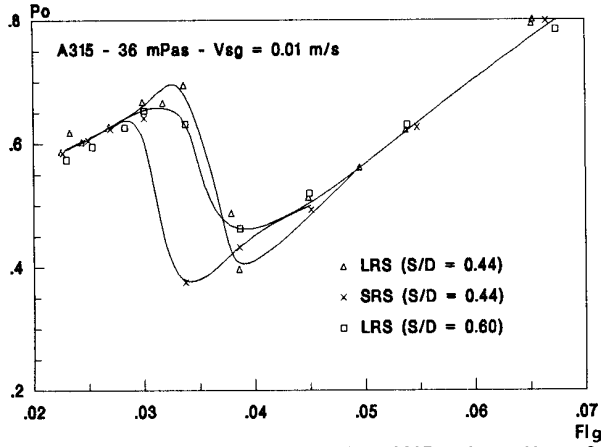

Figure 24 *Power curves for the A315, viscosity of 36 mPas, three spargers configurations, constant superficial gas velocity.*

the quadruple pipe sparger (QPS) and the large ring sparger mounted at S = 0.6 D (fig. 20). It is clear that at low gassing rates there is hardly any difference between these two sparger configurations but that at high superficial gas velocities the QPS performs better than the LRS.

In general it can be concluded that less power is needed to prevent the impeller from flooding when the gas input is moved outwards or further away from the impeller (fig. 6). This may be attributed to two effects. First moving the sparger outwards and/or downwards will lead to a lower gas holdup below the impeller, and to a lower overall gas holdup. This results in a lower static pressure difference which has to be overcome by the impeller; as a consequence flooding will occur less easily. The second effect is related

to the momentum of the input gas. The rising gas will induce an upward fluid motion, which opposes the downward flow below the impeller. The momentum of the input gas has less effect when the gas is supplied in the high velocity region close to the vessel bottom.

2.5.6 Influence of Liquid Viscosity

The Po_g vs. Fl_g curves have been measured for different liquid viscosities, for the A315 impeller with the LRS mounted at an impeller to sparger separation distance S = 0.6 D (fig. 25). Although there are quantitative differences with respect to the positions of the minima and maxima, the basic shape of the curves is the same for all viscosities.

The power curves for the PBT at 80 mPas are also very much similar with those measured for distilled water (fig. 26). The power curves for the Leeuwrik impeller at a constant superficial gas velocity look different from those of the PBT and the A315 due to the different flow regimes which can be distinguished with this impeller. With the Leeuwrik impeller the curves for 80mPas (fig. 27) show a strong increase in power consumption at the transition from axial flow to radial flow. This flow transition was also found with water. Hence it can be concluded that for all three impellers investigated the hydrodynamic processes in the vessel are the same for liquid viscosities within the investigated range from η = 1 mPas to η = 80 mPas.

It is quite interesting to see that for the the A315 the critical power consumption $\langle \varepsilon_c \rangle = P_c/V_l$ increases almost linearly with liquid viscosity within the investigated range (fig. 28).

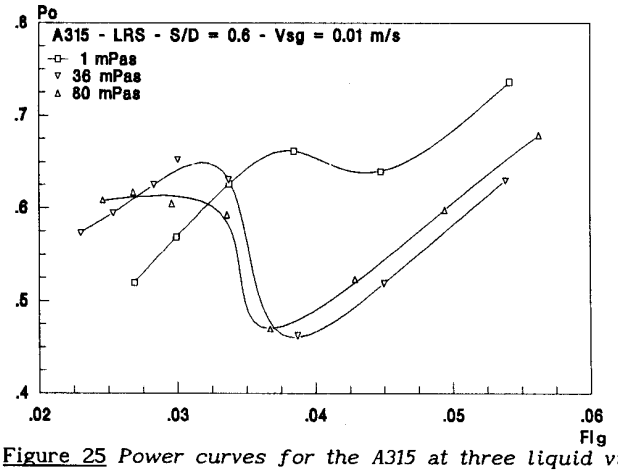

Figure 25 *Power curves for the A315 at three liquid viscosities.*

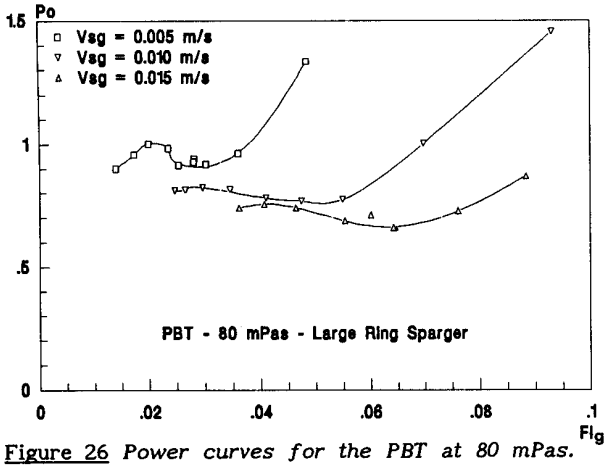

Figure 26 *Power curves for the PBT at 80 mPas.*

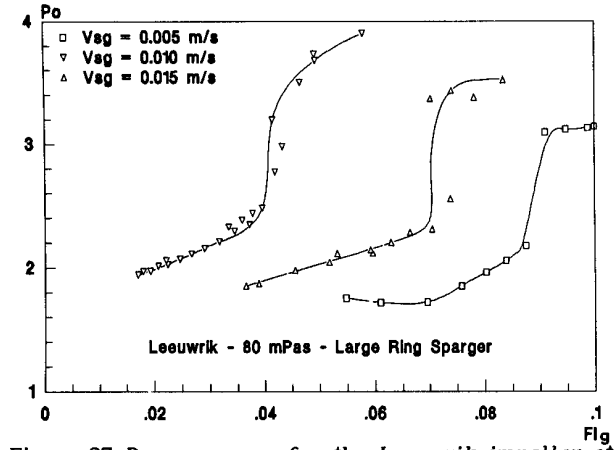

Figure 27 *Power curves for the Leeuwrik impeller at 80 mpas.*

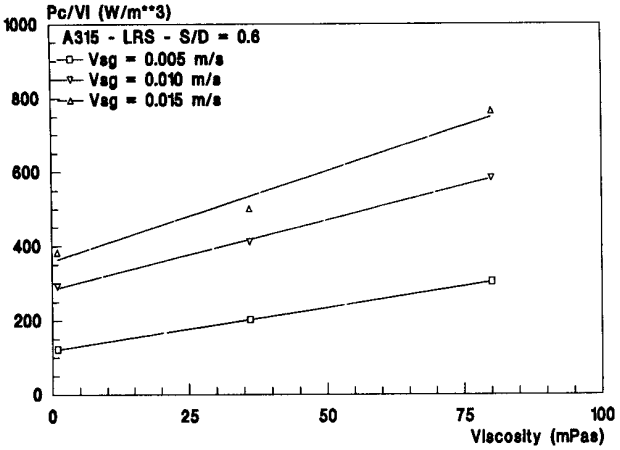

Figure 28 *Minimum power consumption to prevent direct loading vs. viscosity, A315*

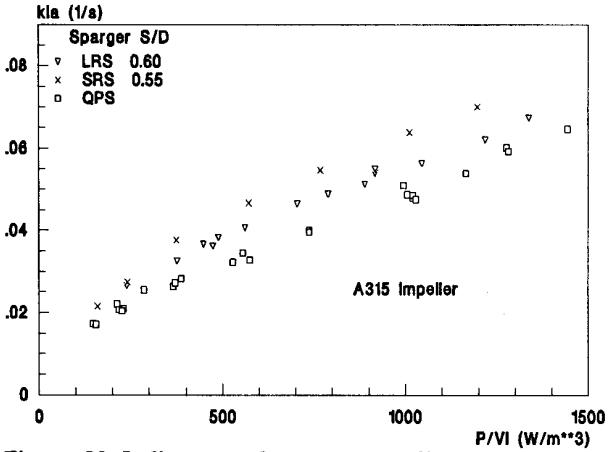

Figure 29 *Influence of sparger configuration on $k_l a$ (A315, v_{sg} = 0.01 m/s).*

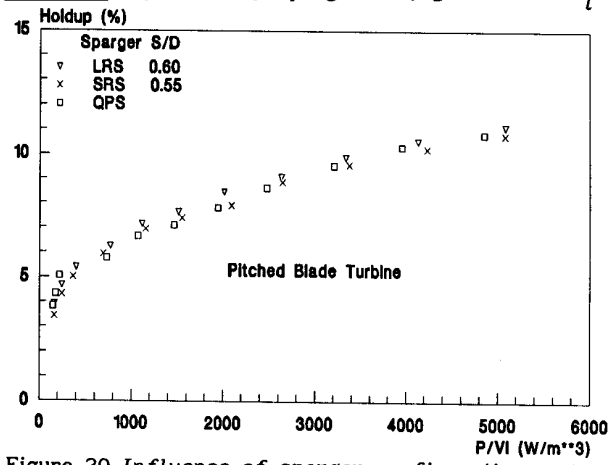

Figure 30 *Influence of sparger configuration on holdup (PBT, v_{sg} = 0.01 m/s).*

2.6 MASS TRANSFER AND GAS-HOLDUP

The quadruple pipe sparger (QPS), the large ring sparger (LRS) placed at S = 0.6 D and the small ringsparger (SRS) at S = 0.5 D were also compared with respect to mass transfer performance (fig. 29). It can be seen from fig. 29 that all data points for the SRS are above all data points for the LRS, which are all lying above the data points for the QPS. This means that there is a significant influence of sparger type on the mass transfer coefficient.

On the other hand the influence of sparger type on gas holdup is not as clear. For the PBT no significant influence of the sparger type on gas holdup was found (fig. 30), whereas for the A315 (fig. 31) the holdup curves for the different sparger types tend to separate for power consumptions between 1000 and 4000 w/m^{-3} but without any clear order.

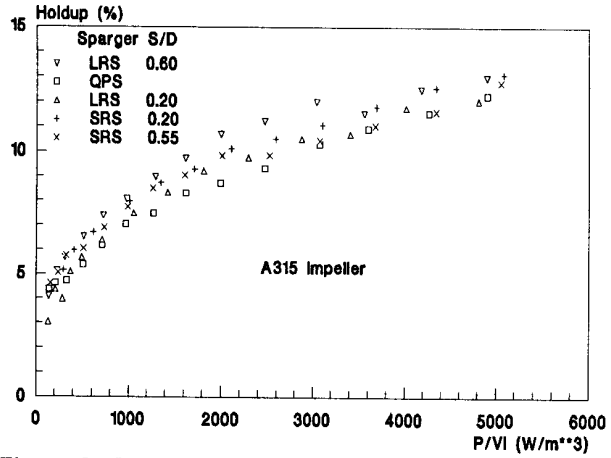

Figure 31 *Influence of sparger configuration on holdup (A315, v_{sg} = 0.01 m/s)*

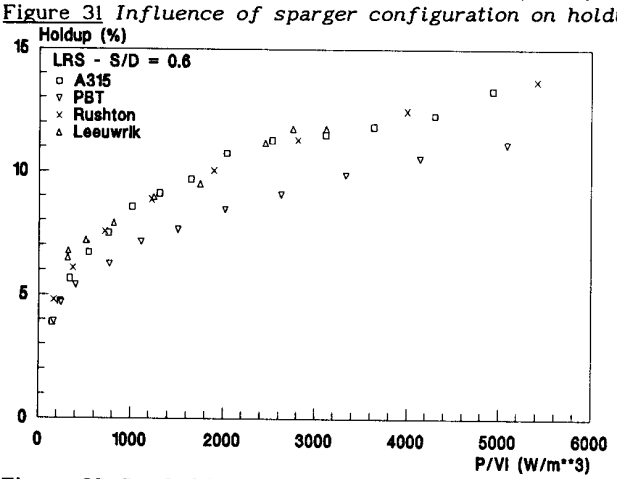

Figure 32 *Gas holdup for various impellers (v_{sg} = 0.01 m/s)*

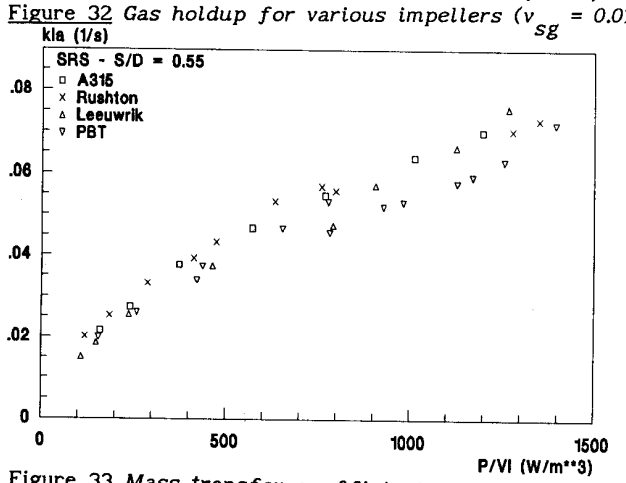

Figure 33 *Mass transfer coefficient for various impellers (v_{sg} = 0.01 m/s).*

The diffuse effects of sparger type on the overall gas holdup might be due to the fact that there are several opposed mechanisms interacting. When the sparger is mounted close to the impeller this will lead to a high gas holdup below the impeller. This will, however, affect the static pressure difference which has to be overcome by the impeller. As a result the impeller pumping capacity may decrease, what will lead to a reduced recirculation rate. Further the high holdup in the turbulent region below the impeller will, in water, lead to an increase in the coalescence rate and consequently to larger bubbles. Since large bubbles have larger rise velocities, they will escape from the vessel faster, which again leads to a lower gas holdup. Further, there are effects of a secondary flow loop below the pitched blade turbine (Frijlink *et al.*, 1990, see also Chapter 3). The position of the sparger with respect to this secondary recirculation loop will also affect the gas holdup below the impeller. It will depend on the exact geometry, impeller type, impeller speed and gassing rate how the overall gas holdup is affected by the sparger type and position.

This suggests that the influence of sparger type on k_la may not fully be attributed to a difference in overall gas holdup, but is merely due to the distribution of the gas in the vessel. The mass transfer rate will not only depend on the gas holdup and bubble size but also on the value of k_l. Since the turbulence distribution will be non-homogeneous, significant differences in k_l throughout the vessel can be expected. Concentrating the gas in the outflow of the impeller, where turbulence levels and k_l are large will lead to an increase in k_la. To be able to give a more detailed explanation of how geometrical changes affect k_la, it will be necessary to analyze the local distributions of the gas holdup, bubble size and turbulence intensity.

In § 2.5.5 it was found that with respect to the minimum power consumption necessary to disperse the gas and the stability of the system, it is advantageous to use a large sparger mounted far away from the impeller. It has now become clear that it will depend on what should be optimized, stability of operation or mass transfer performance, which sparger type should be chosen.

In figures 32 and 33 the four impellers are compared on basis of overall gas holdup and k_la. It turns out that the difference between the A315, the Leeuwrik impeller and the DT is small but that the PBT has the worst performance of the impellers investigated. The fact that there are only small differences between the A315, the Leeuwrik impeller and the DT may be an indication that both the gas dispersion strategies described in § 2.3 may

work. Both creating very small bubbles, but a relatively weak liquid flow (disc turbine) and creating a relatively strong liquid flow but with only little bubble break-up by the impeller (A315) can lead to high mass transfer coefficients. The fact that the PBT has got the worst performance is probably caused by it's relatively low pumping efficiency under gassed conditions, when compared with the A315.

2.7 CONCLUSIONS

The hydrodynamic properties of three axial flow impellers have been investigated. Different flow patterns and different types of cavities were found and were shown to be strongly related to the power consumption.

The flow patterns found for the PBT and the A315 were very similar. At low gassing rates the gas is well dispersed and stable. The gas enters the impeller only after it is recirculated (indirect loading). When the gassing rate is increased, the gas will still be dispersed, but the system becomes unstable and slowly precessing asymmetrical flow patterns are found. The frequency of precession is dependent on the gassing rate, the impeller speed and the sparger geometry. A mechanism based on the interaction between horizontal and vertical vorticity is suggested for this time dependent behavior. When the gassing rate is increased further the gas will enter the impeller directly (direct loading) before it is dispersed, and only little gas recirculation occurs.

As opposed to the A315 and the PBT, the Leeuwrik impeller turned out to have two stable operating modes: axially pumping at low gassing rates and radially pumping at high gassing rates.

The influence of the liquid viscosity on the hydrodynamics has been investigated for viscosities ranging from η = 1 mPas to η = 80 mPas. Within this range no qualitative changes in the basic flow patterns and the hydrodynamic regimes of the impellers were observed. The minimum power consumption to prevent the impeller from flooding, however, showed an almost linear increase with liquid viscosity.

The advantage of a large solidity ratio has been explained in detail in terms of the average pressure difference over the impeller blades. Although blade shape is also important, generally speaking an impeller with a large solidity ratio will be less susceptible to a decrease in pumping capacity when cavities are formed.

Different sparger types have been compared. It turns out that less power is needed to disperse the gas when the gas inlet is moved outwards and/or closer to the vessel bottom. Those sparger configurations which are most effective in dispersing the gas, however, were found to yield a lower overall gas holdup and a lower mass transfer coefficient $k_l a$ than other sparger configurations. This is probably due to changes in the gas distribution and turbulence distribution throughout the vessel. In general, a 0.75 D ring sparger mounted at a separation distance S = 0.6 D will be a good compromise between gas handling capacities and mass transfer performance.

Of the three axial flow impellers investigated, the A315 has the best overall performance. The differences in $k_l a$ between the disc turbine, the A315 and the Leeuwrik impeller are negligible in those regimes where all the impellers are capable of dispersing the gas. The PBT yields a lower gas holdup and $k_l a$ than the other impellers. The A315 does perform better than the PBT with respect to solids suspension under gassed conditions.

The analysis of the gas-liquid hydrodynamics of stirred mixing vessels presented in this chapter has led to several new insights. However, it has also become clear that the methods employed in this chapter have their limits. Although they are very useful for classifying flow patterns and hydrodynamic regimes and for impeller comparison, it is very difficult to increase the fundamental understanding of the processes occurring inside the stirred gas-liquid dispersion, thus new methods have to be developed. It is expected that the application of experimental methods which allow the measurement of local properties of the gas-liquid dispersion, in combination with Computational Fluid Dynamics (CFD) and the development of appropriate models for the gas-liquid flow can overcome these problems. This will be the subject of Chapters 3 to 5.

CHAPTER 3

SINGLE PHASE FLOW IN STIRRED REACTORS

ABSTRACT

Single-phase flow patterns in stirred reactors were investigated both computationally, with FLUENT, and experimentally, by Laser Doppler Velocimetry (LDV). This was done for three different impeller types, viz. two axial flow impellers and a disc-turbine. The effect of geometrical modifications to the vessel geometry was studied as well. Especially the exact baffle arrangement has a strong impact on the flow pattern. It will be shown that the single-phase flow patterns exhibit unexpected features not recognized before.

An accurate numerical computation requires full three dimensional grids. Further, anisotropic turbulence models, in this case the Algebraic Stress Model, give better predictions than the k-ε turbulence model. When these requirements are met, the predicted flow patterns compare very well with the experimental data. Thus a quick assessment of the influence of geometrical variables can be made just using numerical simulations.

3.1 INTRODUCTION

In this chapter the single-phase flow in stirred vessels is described. One of the conclusions of the previous chapter is that it is difficult to get insight in the processes in a gassed stirred tank by investigating overall quantities. The description of the single-phase flow in the stirred vessel given here, will serve as a starting point for modeling the local gas-liquid flow in the tank in later chapters.

Since experimental velocity and turbulence measurements are time consuming and not always possible, the single-phase flow patterns will be studied by means of calculations performed with the general fluid flow code

FLUENT. One of the advantages of this method is that the amount of information which can be generated by such calculations is by far larger than what generally can be reached by performing experiments. For example, FLUENT calculates all the turbulence properties throughout the flow field, including all the Reynolds stresses and the energy dissipation rate, something which is virtually impossible to achieve by LDV experiments.

In this chapter, the influence of grid size, turbulence modeling and numerical techniques on the computational results will be studied by comparing various standard cases with experimental velocity measurements. Three different impellers are used, a disc-turbine, an A315 impeller and a pitched blade turbine. Results from calculations on two-dimensional grids will be compared with those of computations on fully three-dimensional grids. The influence of the turbulence model will be investigated.

3.2 LITERATURE

The developments in the field of Computational Fluid Dynamics (CFD) have led to an increased interest in the numerical computation of the flow field in stirred tank reactors, starting with Harvey and Greaves (1982). These authors modeled the flow generated by a disc turbine on a two-dimensional grid. Although their results had a qualitative appeal, they did not compare very well with literature data. Later on, Placek *et al.* (1985, 1986) also modeled the flow in a turbine stirred tank using a modified three-equation k-ε model. Their results showed a reasonable extent of agreement with velocity measurements near the vessel wall, performed with a pitot tube. Pericleous and Patel (1987) modeled the flow with a disc turbine as well as the flow with axial flow impellers. Due to the use of a simple one-equation turbulence model, their velocity calculations had a limited accuracy only.

As far as the present author knows, Middleton *et al.* (1986) were the first to present full 3-dimensional computations of the flow in a turbine stirred tank in the open literature. These authors also used the calculated single-phase flow patterns as a basis for predicting the chemical reaction yield in such vessels. Ranade and Joshi (1989a,b, 1990a,b) published an interesting series of papers about the single-phase flow in vessels equipped with disc turbines and several types of pitched blade turbines. They presented extensive data sets of velocity measurements done with an LDV

system, and performed a large series of flow computations done with an in-house code. Hutchings *et al.* (1989) used FLUENT for flow predictions in vessels equipped with disc turbines and Lightnin A315 impellers. For the disc turbine, the predicted flow patterns compared quite well with the experimental data. Due to the fact that the computations for the A315 were done on a two-dimensional grid instead of on a full 3-dimensional grid, the predicted flow patterns for this impeller did not compare too well with the experimental data. Kresta and Wood (1991) presented a model for the turbulent kinetic energy and the turbulent energy dissipation rate at the vertical swept boundary of a disc turbine. They reported that their calculations with FLUENT gave a good prediction of the behavior of the turbulent kinetic energy and its dissipation rate in the discharge zone of the impeller.

All the authors mentioned above performed their calculations using isotropic turbulence models, mostly the k-ε model. The turbulence in a stirred vessel is, however, far from isotropic. Apart from anisotropic turbulence generation due to the strong rotational character of the flow, the flow is periodic, due to the fact that the impeller blades pass the baffles. Van 't Riet *et al.* (1976) pointed out that this results in periodic velocity fluctuations, a phenomenon called pseudo-turbulence. It may be clear that the best simulation results are to be expected when time-dependent calculations are done, in combination with the use of an anisotropic turbulence model. Unfortunately this is far beyond current computational capabilities.

Placek *et al.* (1986) therefore proposed a three equation k-ε model, which regards the pseudo turbulence as isotropic turbulence of a different length and time scale. This approach was not followed here, but it is clear that the kinetic energy of the pseudo turbulence in the outflow of the impeller should be included in the boundary conditions. To account for the anisotropy of the turbulence in the flow field, the Algebraic Stress Model (Rodi, 1980, Boysan, 1984) was used for modeling the Reynolds stresses.

3.3 EXPERIMENTAL

Since CFD has not yet reached the stage in which the calculated flow patterns can always be regarded as correct without any experimental validation, there remains a need for experimental velocity data. Further, for fluid flow calculations in a stirred tank experimentally

determined impeller boundary conditions are needed.

Therefore, a series of velocity measurements were performed with a two-dimensional TSI fiberflow laser-doppler system. The system incorporates two TSI-IFA 550 flow analyzers, a 4W Argon-Ion laser from Spectra-Physics and a 80386 MS-Dos computer. Data acquisition and data analysis have been performed with TSI-Find software.

For fast data acquisition the system was operated in the random sampling mode rather than in the even time sampling mode. From the velocity data gathered in this way histograms have been constructed and the first and second moments have been calculated.

The velocity measurements were performed in a perspex stirred tank, being 0.444 m in diameter and filled with distilled water at room temperature. The liquid surface was free. The vessel was equipped with four baffles with a width W = 0.077 T and mounted at a distance of 0.023 T (= 10 mm) from the wall. The torque exerted by the impeller was measured with a VibroMeter torque transducer, mounted in the shaft.

It is known that the flow in a stirred vessel is not fully stationary but contains high frequency periodicities due to the rotation of the impeller. This could not be taken into account and all experimental velocity and turbulence data presented here are time averages including this so-called pseudo turbulence.

Axial velocities could be measured without a problem, but due to refraction on the round vessel wall, determining the position of the measurement volume for the tangential velocities was a laborious task. Further, due to the fact that the measurement volumes for the axial velocity and for the tangential velocity did not have the same position, Reynolds stresses could not be measured. As a result of these experimental problems, tangential velocities and axial velocities, together with their fluctuations, have only been measured in the outflow of the impeller to generate impeller boundary conditions. For validation of the predicted flow patterns, however, only axial velocities have been measured at various positions in the vessel. The experimental problems mentioned above can be overcome by placing the round vessel in a square tank, filled with water. However, such a tank was not available. In all cases studied, the impellers were mounted at an impeller to bottom clearance of C = 0.3 T. The disc turbine (DT) was operated at N = 3Hz, the A315 and the pitched blade turbine (PBT) were operated at N = 6Hz. The diameters of the impellers are listed in table 1 in Chapter 1.

3.4 THEORY OF FLUID FLOW MODELING

The flow fields in the stirred tank reported in this paper were calculated with the commercially available general purpose code FLUENT, version 2.99. FLUENT solves the fluid flow equations on a finite difference grid. All calculations are performed for incompressible steady-state flow. The time averaged continuity equation reads:

$$\vec{\nabla}.\vec{u} = 0 \tag{1}$$

Here $\vec{u}$ denotes the time averaged velocity vector, and $\vec{u}'$ the time dependent fluctuating velocity component. Further, the time-averaged momentum balance can be written as:

$$\vec{\nabla}.(\vec{u}\vec{u}) = -\vec{\nabla}.\left(\frac{p}{\rho}\vec{\vec{I}}\right) + \vec{\nabla}.\left(\nu(\vec{\nabla}\vec{u} + (\vec{\nabla}\vec{u})^T)\right) - \vec{\nabla}.\overline{\vec{u}'\vec{u}'} \tag{2}$$

The first term on the right hand side of this equation denotes the divergence of the pressure, the second term is the divergence of the viscous stresses and the third term is the divergence of the Reynolds stress tensor.

Although exact balance equations for the Reynolds stress tensor can be derived, the set of equations is not closed due to the averaging process. Therefore the Reynolds stress tensor requires modeling. This can, for example, be done by using the so-called Boussinesq hypothesis, which models the Reynolds stresses as being proportional to the mean strain rate:

$$-\overline{\vec{u}'\vec{u}'} = -\frac{2}{3}k\,\vec{\vec{I}} + \nu_t(\vec{\nabla}\vec{u} + (\vec{\nabla}\vec{u})^T) \tag{3}$$

The turbulent viscosity ν_t depends on the turbulence structure only, and not on the fluid properties. In the k-ε model ν_t is calculated from:

$$\nu_t = c_\mu k^2/\varepsilon \tag{4}$$

The spatial distributions of the turbulent kinetic energy density k, defined as:

$$k = \frac{1}{2}\vec{u}'.\vec{u}' \tag{5}$$

and of the turbulent energy dissipation rate density ε are calculated from their respective balance equations. The model equation for k reads:

$$\vec{u}.\vec{\nabla}k = \vec{\nabla}.((\nu + \nu_t/\sigma_k)\,\vec{\nabla}k) + P_k - \varepsilon \tag{6}$$

The model equation for ε is:

$$\vec{u}.\vec{\nabla}\varepsilon = \vec{\nabla}.((\nu + \nu_t/\sigma_\varepsilon)\,\vec{\nabla}\varepsilon) + c_{\varepsilon 1}\frac{\varepsilon}{k}P_k - c_{\varepsilon 2}\frac{\varepsilon^2}{k} \qquad (7)$$

P_k denotes the production of k by the interaction with the mean strain rate:

$$P_k = -\overline{\vec{u}'\vec{u}'}:(\vec{\nabla}\vec{u}) \qquad (8)$$

Further c_μ, σ_k, σ_ε, $c_{\varepsilon 1}$ and $c_{\varepsilon 2}$ are model constants. The k-ε model, however, has a limited validity only. Especially in flows with a strong swirl, this model is known to be inaccurate. This asks for the development of so-called Reynolds stress models, in which Reynolds stress balance equations are solved. These RSM models can be simplified by using the Rodi assumption, (Rodi, 1980) which models the transport of the Reynolds stresses as being proportional to the transport of k. This leads to the so-called Algebraic Stress Model (ASM):

$$-\overline{\vec{u}'\vec{u}'} = \frac{2}{3}k\,\vec{I}\left[1 - \frac{(1-c_2)\frac{P_k}{\varepsilon}}{\frac{P_k}{\varepsilon}-(1-c_1)}\right] + \frac{1-c_2}{\frac{P_k}{\varepsilon}-(1-c_1)}\frac{k}{\varepsilon}\left(\vec{P} - \frac{2}{3}P_k\,\vec{I}\right) \qquad (9)$$

$$\vec{P} = -\left(\overline{\vec{u}'\vec{u}'}.(\vec{\nabla}\vec{u}) + (\overline{\vec{u}'\vec{u}'}.(\vec{\nabla}\vec{u}))^T\right) \qquad (10)$$

Here c_1 and c_2 are model constants. For reasons of comparison several flow computations were done with both the k-ε model and the ASM. The model constants for both the k-ε model and the ASM are given in table 1.

Table 1 The model constants used in the turbulence modeling.

c_μ	σ_k	σ_ε	$c_{\varepsilon 1}$	$c_{\varepsilon 2}$	c_1	c_2
0.09	1.00	1.30	1.44	1.92	2.20	0.45

3.5 THE COMPUTATIONAL MODEL

3.5.1 Impeller boundary conditions

Calculations were performed for a radially pumping disc turbine and for two axially pumping impellers, viz. a Lightnin A315 and a standard pitched blade impeller with six blades.

There are several possibilities for modeling the impellers. For example, axial flow impellers can be modeled as a momentum source using aerofoil theory (Pericleous and Patel (1987)). The flow through a disc turbine, on the other hand can directly be calculated by modeling the turbine blades as being at rest while having the tank rotating (Hutchings *et al.*, 1989). One of the problems with this procedure is that now the baffles require modeling. These two methods, however, have not yet been proven to yield correct predictions. Further, it was not possible to incorporate these models in FLUENT 2.99. Thus, in this work the impellers were modeled by prescribing experimental flow profiles as measured with the LDV system, in the outflow of the impeller.

For the disc turbine the u,v, and w-velocities, denoting the axial, radial and tangential velocities respectively, together with the turbulent kinetic energy k and dissipation rate ε have been prescribed on the vertical swept boundary of the impeller, using parabolic profiles according to the data presented by Ranade and Joshi (1990).

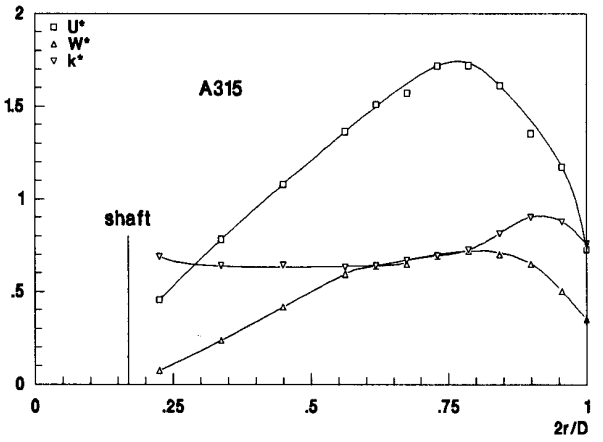

Figure 1 *Velocity and turbulence profiles in the outflow of the A315, experimental data.*

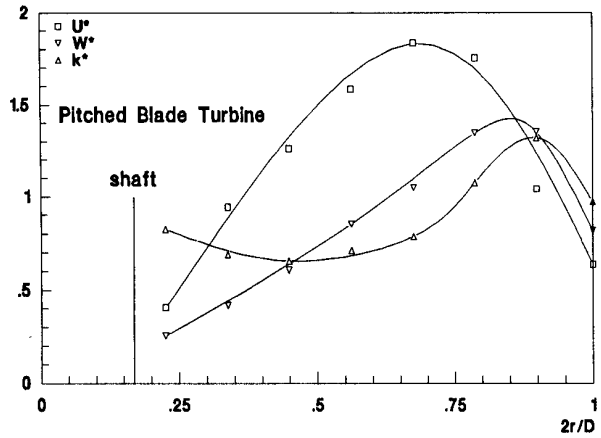

Figure 2 *Velocity and turbulence profiles in the outflow of the pitched blade turbine, experimental data.*

For the computations with the inclined blade impeller and the A315 impeller the velocity and turbulence profiles were prescribed at the bottom surface of the impellers, according to own experimental data (figs. 1 and 2). In these graphs all the mean velocities and k are made dimensionless with $N\ Fl_1\ D$, which is proportional the mean axial velocity in the impeller outflow:

$$u^* = \frac{u}{N\ Fl_1\ D} \qquad w^* = \frac{w}{N\ Fl_1\ D} \qquad k^* = \frac{\sqrt{2k}}{N\ Fl_1\ D} \tag{11}$$

For the axial flow impellers the pumping number Fl_1 is defined as:

$$Fl_1 = \frac{Q_1}{N\ D^3} = \frac{1}{N\ D^3} \int_0^{D/2} u(z=H-C+H_i/2)\ 2\ \pi\ r\ dr \tag{12}$$

H_i is the height of the impeller. A similar definition is used for the disc turbine:

$$Fl_1 = \frac{Q_1}{N\ D^3} = \frac{1}{N\ D^3} \int_{H-C-D/10}^{H-C+D/10} v(r=D/2)\ \pi\ D\ dz \tag{13}$$

The values of Fl_1 and Po are listed in table 2.

It should be noted that since the radial velocities could not be measured, the experimental k-values presented here were calculated as:

$$k = \frac{3}{4}\left(\overline{u'^2} + \overline{w'^2} \right) \tag{14}$$

The axial velocity profiles for the A315 and the PBT are very similar, with low velocities near the center and peaks in the velocities at about 0.4 D. The main difference between the two impellers lies in the profiles of the tangential velocities. The tangential velocity profile of the A315 is much flatter (fig. 1), and the A315 creates lower tangential velocities than the PBT (fig. 2). This can also be seen from the Swirl number which is a measure for the ratio between the flux of angular momentum and the flux of axial momentum:

$$S = \frac{\int_0^{D/2} u\, w\, r^2\, dr}{\frac{1}{2}D \int_0^{D/2} u\, u\, r\, dr} \tag{15}$$

The Swirl numbers, as calculated from the experimental data, for the A315 and the PBT are listed in table 2. The A315 converts less input energy in angular momentum than the PBT.

In all cases the turbulent kinetic energy k was prescribed according to the measurements, and the local energy dissipation rate ε was calculated, assuming that the turbulent length scale L_t:

$$L_t = k^{3/2}/\varepsilon \tag{16}$$

was proportional to the width W_b of the impeller blades:

$$\varepsilon = k^{3/2}/\frac{1}{4}W_b \tag{17}$$

The proportionality factor 1/4 was taken from Wu and Patterson (1989).

Table 2 Power number, Flow number and Swirl number for the three impellers.

	Po	Fl_l	S
A315	0.76	0.74	0.31
PBT	1.55	0.81	0.52
DT	5.10	0.76	--

3.5.2 The computational grid

The calculations were performed on two-dimensional grids, assuming rotational symmetry, and on three-dimensional grids. To check for possible grid dependency several grid sizes were tested: 50x25, 42x27 and 28x14 grid nodes for the two-dimensional calculations and 50x25x20, 40x25x25, 52x27x17 and 56x35x11 for the three dimensional calculations in (z,r,ϕ) coordinates. Here z denotes the distance from the liquid surface, r the radial distance from the center and ϕ is the tangential coordinate, being 0 at the baffle.

Due to computational restrictions grids with more than 25000 grid nodes could not be tested.

The three-dimensional calculations were done for a 90 degree segment of the vessel with cyclic cells at $\phi = -45^{\circ}$ and at $\phi = 45^{\circ}$. The no-slip condition was applied using a wall law at the vessel walls, the bottom, the baffles and the impeller shaft. The liquid surface was treated as a no slip surface. A typical computational grid is shown in fig. 3. All computations were done at non-uniform grids.

3.5.3 Computers, computing time and convergence

The computations were done at a Hewlett-Packard 9000-835 series minicomputer with 24 MB of RAM and a computing speed of 2 MFlops. On this computer one iteration for a non-uniform grid of 25000 grid nodes took ± 1 minute.

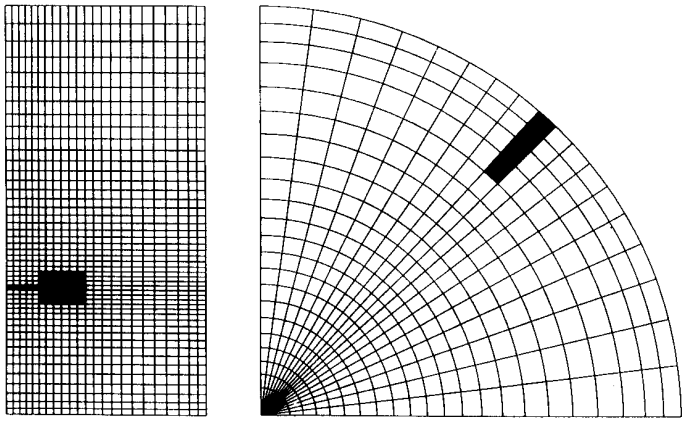

Figure 3 *Computational grid for the disc turbine, side view and top view.*

The convergence criterion used in all cases was that the sum of the normalized residuals was smaller than 1E-3. The influence of the convergence criterion has been tested by comparing the calculations for the PBT when converged to 1E-2, 1E-3 and 5E-5. From 1E-2 to 1E-3 the solution still changed. The step from 1E-3 to 5E-5 gave no improvement.

Probably due to numerical problems, physically unrealistic flow patterns were encountered for the flow in regions with a strong swirl and with very small axial and radial velocities, especially with the DT in the region below the shaft. As a result it was decided to perform the computations for the DT with a shaft running through the vessel bottom.

For the disc turbine 2000-3000 iterations were necessary to reach a converged solution when there was a small baffle-wall spacing. Without baffle-wall spacing the flow pattern was more complex and about 5000-6000 iterations were needed. With the PBT and the A315 the flow pattern is more complex, and depending on baffle geometry, 3000-7000 iterations were necessary.

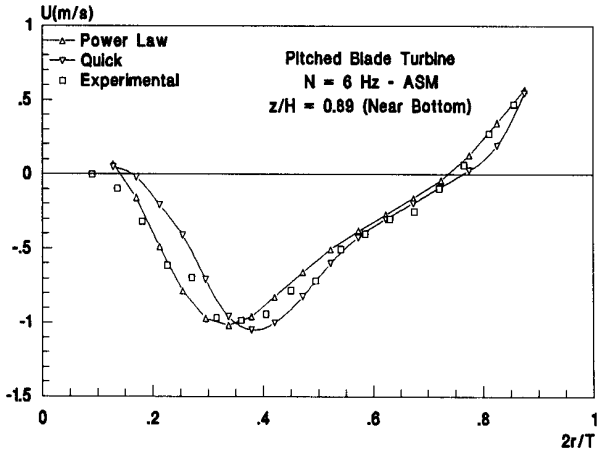

Figure 4 *Comparison between predicted and measured axial velocities.*

3.5.4 Numerical Schemes

FLUENT comprises two interpolation schemes, the Power Law scheme and the QUICK scheme (Quadratic Upstream Interpolation for Convection Kinematics). Both schemes were tested for the flow with a PBT and a 0.023T baffle-wall

spacing. The difference between the predictions with these schemes was small. This is illustrated in figure 4, where simulation results of the axial velocity are compared with experimental data. Here, the simulations with the Power Law scheme followed the experimental data slightly better. Since there seemed to be no advantage in using the QUICK scheme, and the computing time with this scheme was longer, it was decided to perform all further computations with the Power law scheme.

3.6 RESULTS CONCERNING THE MEAN FLOW

3.6.1 Disc Turbine

Figures 5a,b show the flow pattern for the disc turbine as calculated on a 3D grid with 50x25x20 nodes. Figure 5a shows the flow pattern in the plane midway between two baffles (ϕ = 45°), whereas the velocity vectors in the plane just in front of a baffle (ϕ = -3°) are shown in figure 5b. In both planes the flow is characterized by two main circulation loops, one on each side of the impeller. It can be seen that at ϕ = -3° the center of these loops lies more inwards, and closer to the radial jet coming from the impeller than at ϕ = 45°. As far as the present authors know this fact has not been reported before, but it shows that for an accurate numerical computation of the flow field full 3D-simulations are necessary.

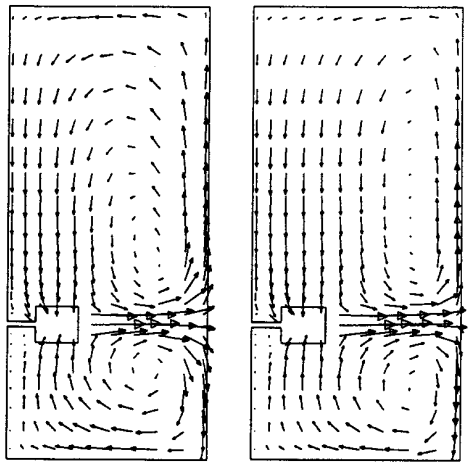

Figure 5a,b *Velocity vectors for the disc turbine, in front of the baffle (ϕ = -4°) and midway between the baffles (ϕ = 45°)*

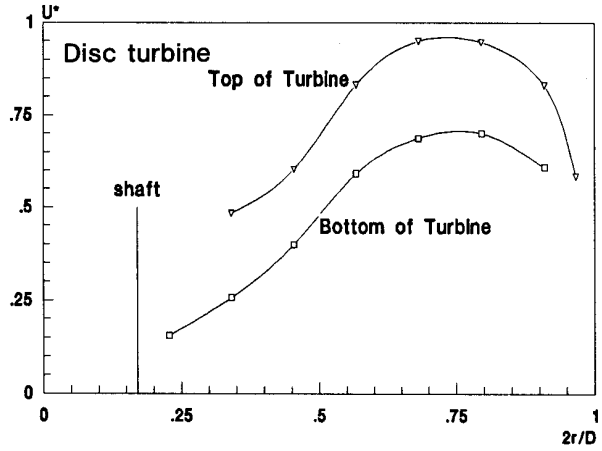

Figure 6 *Absolute value of the axial velocity at the top of the turbine and at the bottom of the turbine.*

Due to the fact that the turbine is mounted closer to the vessel bottom (at C = 0.3 T) than to the liquid surface, the average axial liquid velocity at the top of the impeller was 1.4 times that at the bottom. This is illustrated in figure 6 where the absolute values of the axial velocities on both sides of the turbine are plotted. This phenomenon probably results from the difference in friction above and below the impeller.

Figure 7 shows a comparison between the calculated axial velocity components and the measured axial velocities at different positions in the vessel. In general, the model predictions and the experimental data agree quite well thus giving confidence in the results for the mean velocities.

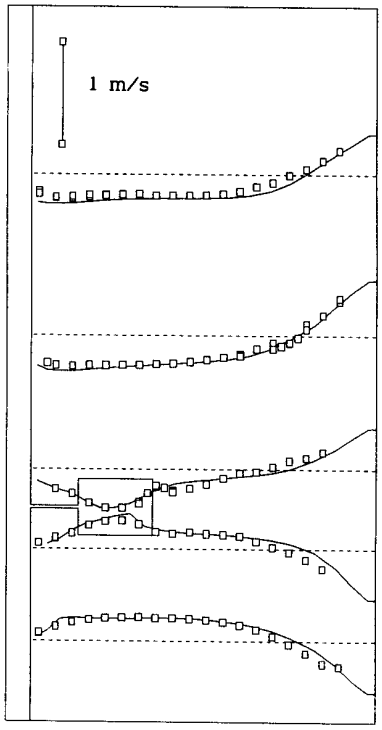

Figure 7 *Comparison between predicted and measured axial velocities. (□ experimental, —— simulation)*

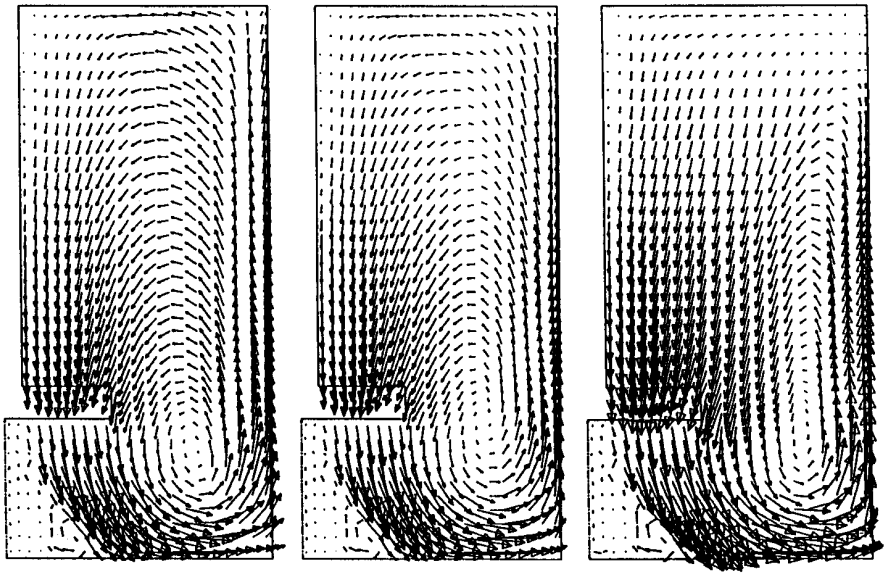

Figure 8a,b,c *Velocity vectors for the pitched blade turbine with 0.023 T wall-baffle spacing, in front of baffle (ϕ = -2°), behind baffle (ϕ = 13°), midway baffles (ϕ = 45°)*

3.6.2 Axial Flow Impellers

The flow pattern calculated for the PBT turned out to be very sensitive to the exact baffle geometry. The computations presented here were done with 40x25x25 grid nodes.

Figures 8a,b,c show the flow pattern for a PBT with baffles mounted a small distance from the wall (0.023 T baffle-wall spacing). Figure 8a shows the flow pattern just in front of the baffle (ϕ = -2°). In this plane the flow pattern consists of a large circulation loop, and a small recirculation loop below the impeller. A small distance behind the baffle (ϕ = +13°) the flow pattern is approximately the same, although the center of the large circulation loop is shifted slightly upwards, while the velocities are slightly smaller. The flow midway between the baffles (ϕ = 45°) is different from the flow pattern in front of the baffle. Now a small second recirculation loop has formed in the upper part of the vessel, and that the flow along the wall in the top of the vessel is directed downwards rather than upwards. In all planes a more or less dead zone with very small, partly upwards directed velocity vectors is found below the impeller.

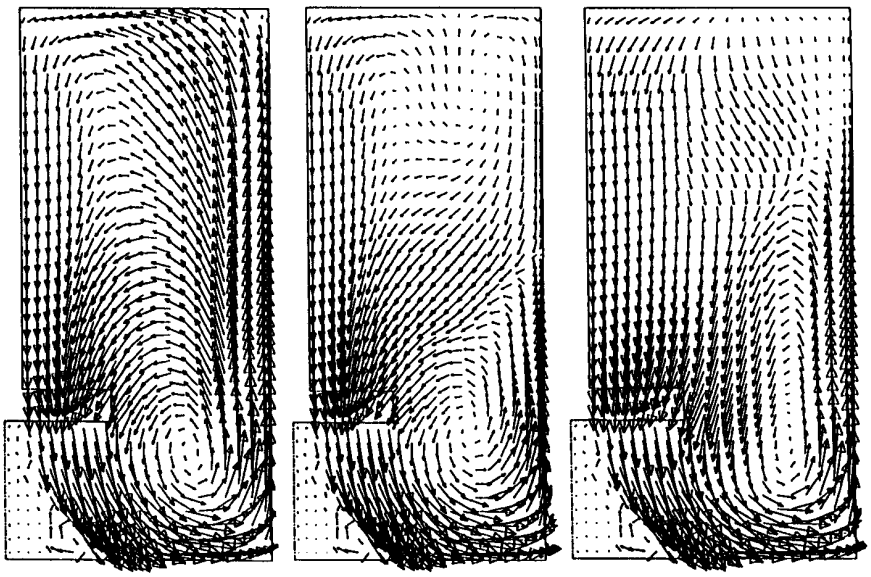

Figure 9a,b,c *Velocity vectors for the pitched blade turbine with zero wall-baffle spacing, in front of baffle (ϕ = -2°), behind baffle (ϕ = 13°), midway baffles (ϕ = 45°)*

The flow pattern with baffles mounted directly to the vessel wall, with zero spacing, is shown in figs. 9a,b,c. In front of the baffle (fig. 9a, ϕ = -2°) the flow pattern consists of a large circulation loop, and a small recirculation loop below the impeller, approximately the same as with 0.023 T baffle spacing. Just behind the baffle (ϕ = 13°), however, a second circulation loop has formed in the upper part of the vessel. In this region the flow along the wall is directed downwards, rather than upwards. At ϕ = 45° this secondary loop is already much smaller.

Thus it can be concluded that both with zero baffle-wall spacing and with 0.023 T baffle-wall spacing, a second circulation loop is formed in the upper part of the vessel, but that the position and size of this loop are different. This can be explained by looking at the velocity vectors, at two different heights in the vessel (fig 10a,b and 11a,b). It can be seen that with zero baffle-wall spacing a secondary circulation loop behind the baffle is found in the upper part of the vessel, with negative tangential velocities along the wall. With a small baffle wall spacing this does not occur, which explains why in this case the secondary circulation loop is much smaller.

The second recirculation loop extends about 50° away from the baffle.

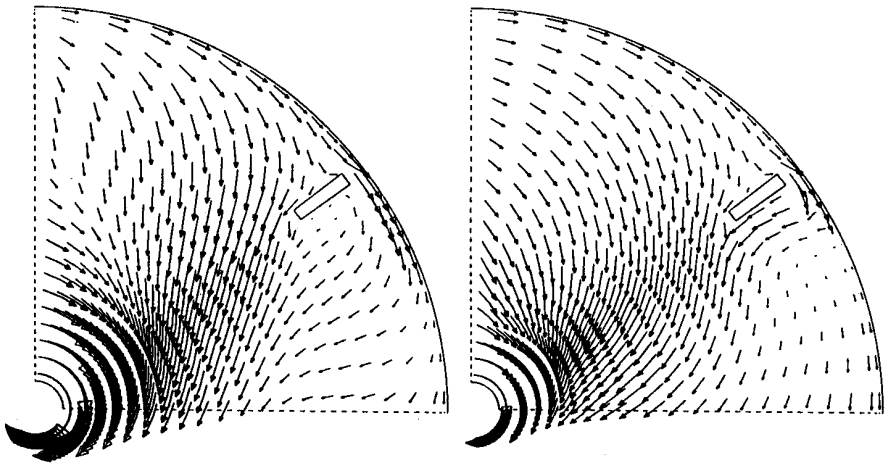

Figure 10a,b *Velocity vectors for the pitched blade turbine, top view, 0.023 T baffle-wall spacing, z/H = 0.28 (left) and z/H = 0.66 (right).*

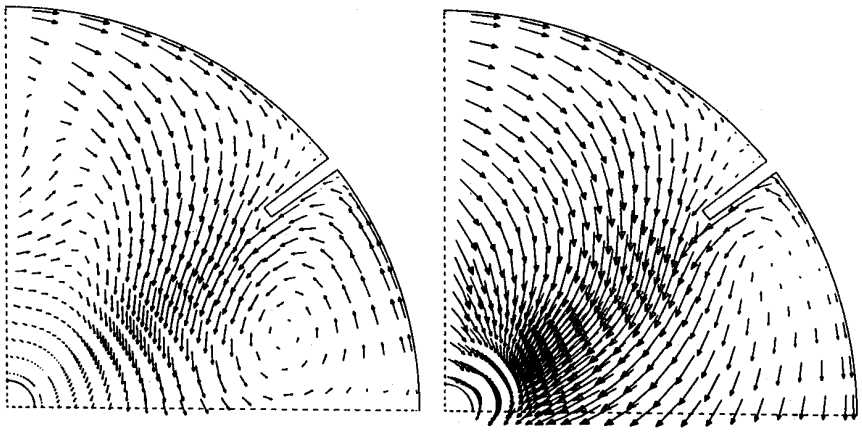

Figure 11a,b *Velocity vectors for the pitched blade turbine, top view, zero baffle-wall spacing, z/H = 0.28 (left) and z/H = 0.66 (right).*

Bakker and Van den Akker (1991) reported a value of 33°, but their calculations were done with 17 grid nodes in the tangential direction. Due to computational restrictions it could not be tested whether grid independence has yet been achieved.

It should be noted that when 2-dimensional calculations are done, assuming axisymmetry such secondary circulation loops are not found (fig. 12). This clearly shows the need of 3-dimensional calculations.

Figure 13 shows the measured axial velocities as a function of the axial coordinate near the vessel wall, midway between the baffles. It can be seen that the axial velocities change sign at $z/H \approx 0.35$ and that the liquid velocities are directed downwards in the upper part of the vessel. These experimental data explicitly prove the existence of this secondary circulation loop.

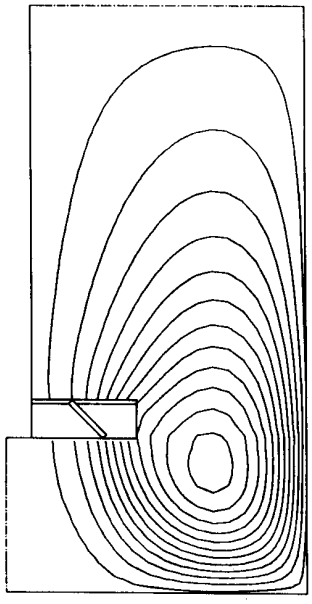

Figure 12 *Streamlines for the PBT. Simulations done on a two-dimensional grid, assuming rotational symmetry and zero tangential velocities.*

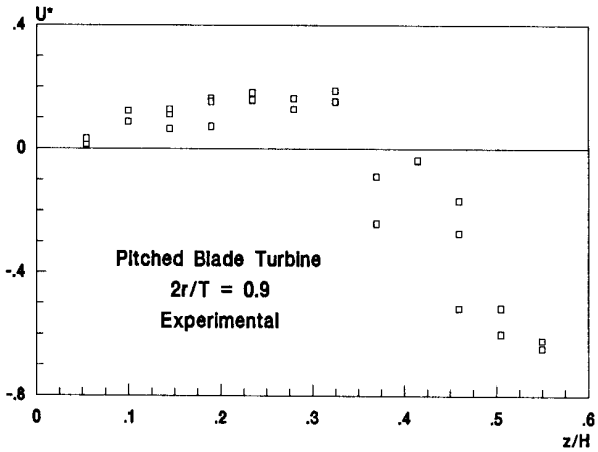

Figure 13 *Axial velocities as a function of z/H for the pitched blade turbine, midway between baffles, ϕ = 45°, 2r/T = 0.9, 0.023 T baffle-wall spacing, experimental data.*

Figure 14a shows a comparison between calculated and measured profiles of the axial velocity at several positions in the vessel for 0.023 T baffle-wall spacing. In general the model predictions agree quite well with the experimental data, except in the upper part of the vessel where according to the experimental data all mean velocities are directed downwards.

Thus it can be concluded that the predicted flow patterns are qualitatively correct, showing details not reported before in the literature, but that the quantitative accuracy in the upper part of the vessel could be improved even further.

The gross characteristics of the flow pattern induced by the A315 are the same as with the pitched blade turbine (fig. 14b). The main difference is that with the A315 no circulation below the impeller was measured, as with the PBT. However, the predicted data do not exactly follow the experimental data in the region below the impeller. This may be due to the convergence problems in regions with strong swirl and small axial velocities mentioned earlier. With the A315, there is also a second recirculation loop in the upper part of the vessel as with the PBT.

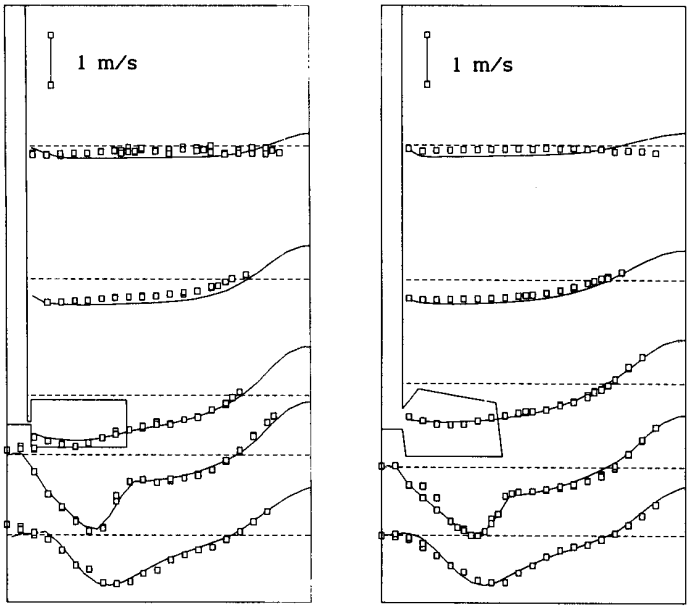

Figure 14a,b *Comparison between predicted axial velocities and measured axial velocities, pitched blade turbine (left) and A315 (right). (□ experimental and —— simulation).*

3.7 RESULTS CONCERNING THE TURBULENCE

3.7.1 Turbulence Distribution

To validate the predicted turbulence properties, experimentally determined profiles of RMS(u') (RMS = Root Mean Square) and computed profiles were compared. Figure 15 shows the comparison for the A315, as calculated with the aid of the ASM. The predicted values of RMS(u') compare better with the measured values in the regions near the baffles than in the regions above and below the impeller. This might be due to the fact that the flow pattern as induced by the rotating impeller will contain periodic high frequency velocity fluctuations, a phenomenon called pseudo-turbulence. These fluctuations will increase the measured values of RMS(u') in the inflow and outflow of the impeller, but may well be dampened out near the baffles. As a result, the predictions for RMS(u') will be more accurate near the baffles.

The values of k which are prescribed in the outflow of the impeller contain these periodic velocity fluctuations. However, RMS(u') is still under predicted near the vessel bottom, in the outflow of the impeller. This is probably due to the fact that the pseudo-turbulence and the real turbulence have got different dissipation rates. It may be worth investigating whether the use of the two-scale turbulence model proposed by Placek *et al.* (1986), with separate equations for the turbulent kinetic energy and the kinetic energy of the pseudo turbulence, gives better results.

The anisotropy of the turbulence is illustrated by figure 16. This

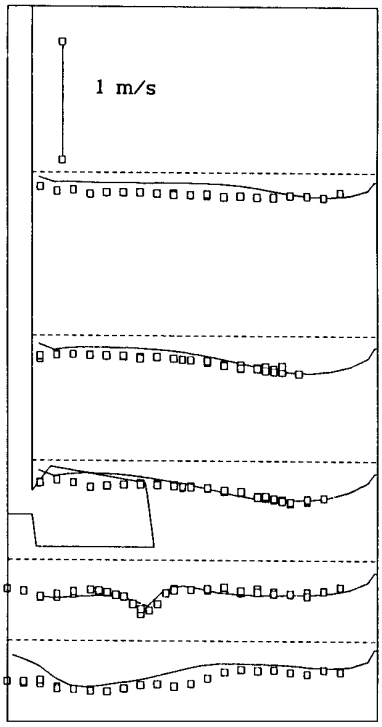

Figure 15 *Comparison between predicted and measured RMS(u') (□ experimental, —— simulation)*

graph shows a comparison between the predicted values of RMS(u'), RMS(v') and RMS(w') together with the measured values of RMS(u') and the value of $\sqrt{2k/3}$ as predicted with the k-ε model. The value of $\sqrt{2k/3}$ is a measure of RMS(u') as predicted by the k-ε model. It is clear that the values of RMS(u') as predicted by the ASM compare better with the experimental data than the value of $\sqrt{2k/3}$ as predicted by the isotropic k-ε model. Further there are large differences between the values of RMS(u'), RMS(v') and RMS(w'), thus showing the need for anisotropic turbulence models.

Contours of equal turbulent kinetic energy and dissipation rate, as calculated with the ASM, are plotted in figs. 17 and 18 for both the disc-turbine and the PBT. It can be seen that in both cases the highest turbulence intensities are found in the outflow of the impellers, and that both k and ε are much lower in the bulk of the vessel.

With the PBT a region of high values of both k and ε is found near the baffles, above the impeller. This is probably due to the large velocity gradients near the center of the main circulation loop and the interaction with the secondary flow loop in the top of the vessel. Large velocity gradients lead to an increased production P_k of turbulent kinetic energy and production $\vec{\vec{P}}$ of Reynolds stresses. (eq. 8, 10). As a consequence the production P_ε of ε also increases, since in the model equations it is assumed that P_ε is proportional to P_k:

$$P_\varepsilon \sim \frac{\varepsilon}{k} P_k \qquad (18)$$

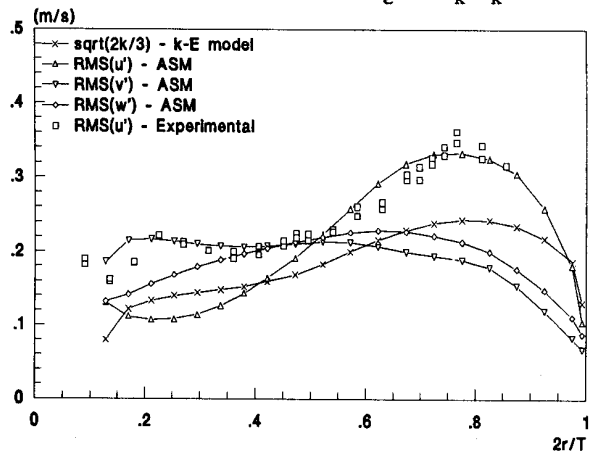

Figure 16 *Experimental data for RMS(u'), predicted data for RMS(u'), RMS(v') and RMS(w') with ASM and* $\sqrt{2k/3} \approx$ *RMS(u') with k-ε (just above A315, z/H = 0.64,* $\phi = 45^0$*)*

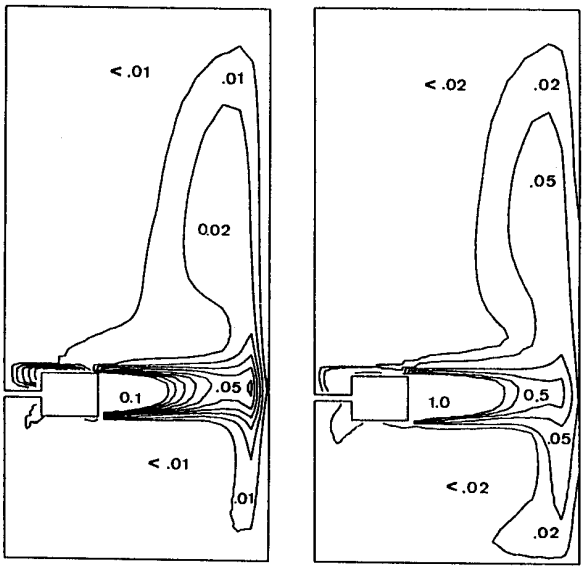

Figure 17a,b *Contours of constant k (m^2s^{-2}) and ε (m^2s^{-3}) for the disc turbine (3Hz), numbers denote minimum values in areas enclosed by contours.*

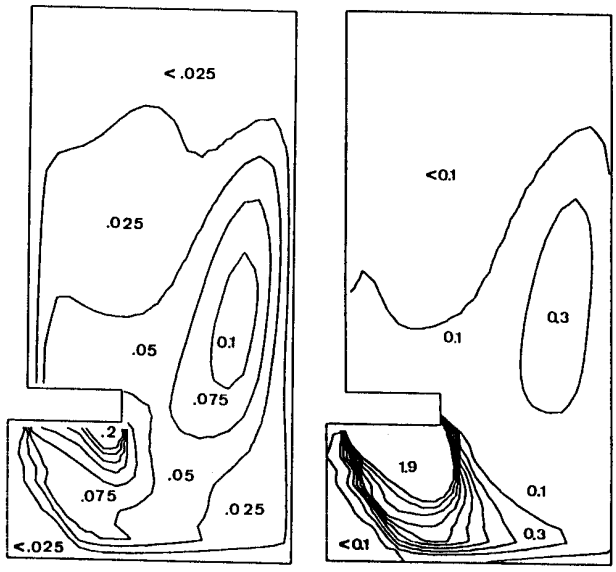

Figure 18a,b *Same as figure 17 but now for the pitched blade turbine (6Hz).*

3.7.2 Energetic Efficiency

The power consumption P of an impeller is given by:

$$P = Po\ \rho\ N^3\ D^5 \tag{19}$$

Here Po denotes the so-called power number which, for a given vessel geometry, is a function of impeller type only. A significant part of the energy input is dissipated in the impeller swept volume V_{imp} rather than in the liquid bulk. Since the local mixing in the liquid bulk may be determined by the local turbulence intensity, it is necessary to have a estimation of the fraction of the total energy input which is dissipated in the liquid bulk. Therefore the energetic efficiency η_e can be defined as:

$$\eta_e = 1 - \frac{V_{imp} <\varepsilon_{imp}> \rho}{P} \tag{20}$$

Here $<\varepsilon_{imp}>$ denotes the average energy dissipation rate per unit mass in the impeller zone. The energetic efficiency is difficult to measure since it requires measuring local values of ε. Therefore it is not surprisingly that different authors present different values for η_e. Experimental studies with the disc turbine resulted in values ranging from 40% to 70% (see the review by Ranade and Joshi, 1990a). This means that between 30% and 60% of the total energy input is dissipated in the impeller swept volume, which makes up only 1.2% of the total volume, thus leading to extremely large values of $<\varepsilon_{imp}>$. According to the experimental data from Ranade and Joshi (1989) the energetic efficiency for a pitched blade turbine ranges from 53% to 78% depending on blade width, impeller to bottom clearance and D/T ratio. For the A315 no data regarding η_e are available in the open literature.

It should be noted that η_e is not the same as the pumping efficiency defined by Bakker and Van den Akker (1990a). The pumping efficiency η_p is the fraction of the energy which is used in the main flow, and can thus be defined as the ratio of the gain in enthalpy of the fluid, $\Delta p.Q_l$, to the power input P by the impeller. The pressure rise Δp over the impeller as determined by, among other things, rotational speed N and impeller geometry is converted into velocity head of a circulatory flow:

$$\Delta p = K_w \frac{1}{2} \rho_l \bar{v}^2 \sim \rho_l \frac{Q_l^2}{T^2} \tag{21}$$

The proportionality constant K_w depends on the vessel geometry only and is not known in general. By using Po and Fl_l the following relation can be found:

$$\eta_p = \Delta p \frac{Q_l}{P} \sim \left(\frac{D}{T}\right)^4 \frac{Fl_l^3}{Po} \qquad (22)$$

In general the pumping efficiency will be lower than the energetic efficiency since the energy which is put into the generation of turbulent kinetic energy by the impeller and in trailing vortices shed from the impeller blades is included in the energetic efficiency but not in the pumping efficiency.

The predicted values for η_e both according to the calculations with the k-ε model and the ASM are listed in table 3. It can be seen that with the DT the predicted value of η_e compares well with the literature values, provided that the ASM is used. With the k-ε model, the predicted energy dissipation rates are significantly lower than with the ASM.

With the PBT the predicted η_e is on the low side, which might be due to an under predicted ε as a result of not taking the pseudo turbulence into account. The predicted η_e is higher for the A315 than for the PBT as a result of the profiled blades.

Table 3 Predicted values of η_e with k-ε and ASM.

	η_e(k-ε)	η_e(ASM)	Literature
A315	48%	57%	---
PBT	38%	45%	53%-78%
DT	45%	53%	40%-70%

3.8 STABILITY OF THE MEAN FLOW

All the calculations have been done assuming a steady state flow with normally distributed turbulent velocity fluctuations. This assumption turns out not always to be valid. Figure 19a shows an experimentally determined velocity distribution for the PBT at z/T = 0.45 and at 2r/T = 0.88, just above the impeller near the vessel wall. In this region the measured

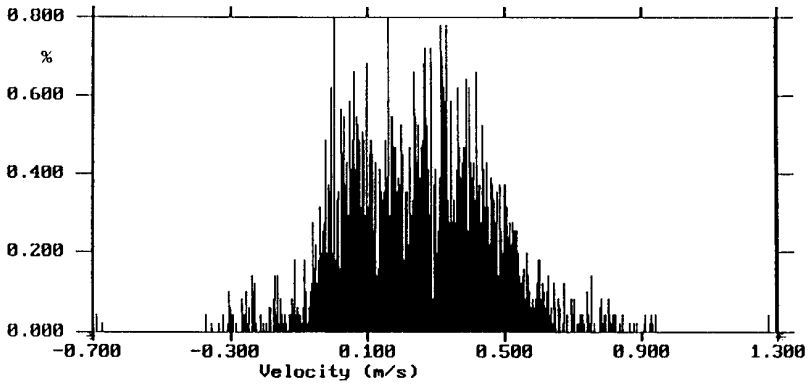

Figure 19a *Measured u-distribution, PBT, z/H = 0.45, 2r/T = 0.88, ϕ = 45^{o}*

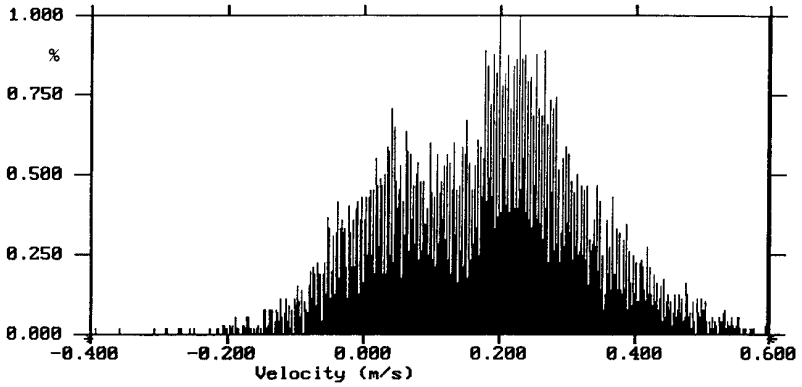

Figure 19b *Measured u-distribution, PBT, z/H = 0.25, 2r/T = 0.13, ϕ = 45^{o}*

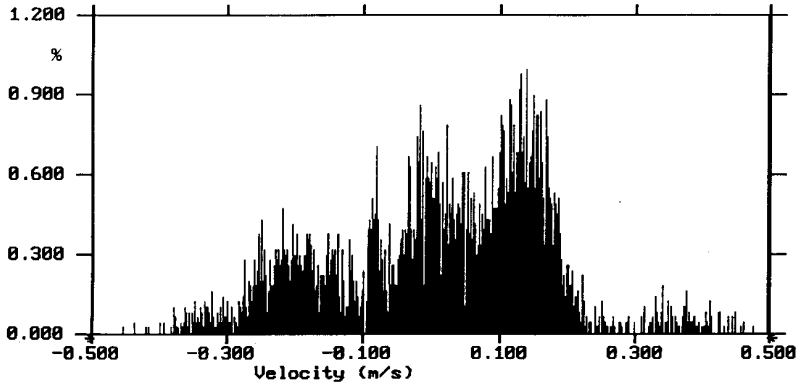

Figure 19c *Measured u-distribution, PBT, z/H = 0.10, 2r/T = 0.88, ϕ = 45^{o}*

velocities are indeed gaussian distributed. In the upper part of the vessel, at $z/H = 0.25$ at $2r/T = 0.13$, (fig. 19b), however, the measured liquid velocities turn out to have a bimodal distribution. This suggests that the flow in this region is bistable, and that it oscillates periodically. It would be interesting to see whether it is possible to resolve this oscillating behavior by performing time-dependent calculations. Unfortunately, due to computational restrictions this could not be tested.

Close to the liquid surface (fig. 19c, $z/T = 0.1$, $2r/T = 0.88$) the velocity distribution has even got three peaks, at a negative axial velocity, near zero, and at a positive axial velocity. This is probably a result of waves, running at the liquid surface. Thus, it is unlikely that any turbulence model will give a realistic picture of the flow in this part of the vessel.

Although skewed velocity distributions were sometimes observed with the DT and the A315, bimodal and trimodal distributions were only observed with the PBT in the upper part of the vessel. These deviations from gaussian turbulence might to some extent be responsible for the differences between the measured velocity and turbulence data and the predicted data in this region, as compared in figures 12 and 16. Whether this problem can be solved by performing transient calculations is not clear.

3.9 CONCLUSIONS

Both two-dimensional computations and three-dimensional computations of the single-phase flow in stirred vessels have been performed. In general it can be concluded that the flow pattern in stirred vessels is fully three-dimensional, exhibiting secondary recirculation loops and unexpected features not recognized before.

With the disc turbine it was found that the position of the center of the two main circulation loops is a function of the tangential coordinate ϕ. The predicted flow patterns for the disc turbine were found to match quite well with the experimental data. Further it was found that when the turbine is mounted closer to the vessel bottom than to the liquid surface ($C/T = 0.3$), the axial velocities at the top of the impeller are about 1.4 times those at the bottom of the impeller.

The flow pattern of the axial flow impellers turned out to be sensitive to the exact baffle configuration. Both with zero baffle-wall spacing and

with 0.023 T baffle-wall spacing a second circulation loop in the upper part of the vessel is formed. The exact size and position of this loop is determined by the baffle geometry. The existence of this secondary loop is proven by experimental data. With two-dimensional simulations this loop was not found, thus clearly showing the need of three-dimensional simulations. In general, the fluid flow predictions and the experimental data match quite well although in the upper part of the vessel the quantitative accuracy could be improved even further.

In the upper part of the vessel bimodal and trimodal velocity distributions were measured. This shows that the assumption of steady state flow with normally distributed turbulent velocity fluctuations is not always valid in this region. It might be necessary to perform transient flow field computations to reproduce these phenomena.

In case of a zero baffle-wall spacing a secondary circulation loop behind the baffle was found in the upper part of the vessel, with negative tangential velocities.

The flow patterns as generated by the A315 and the PBT look very similar. The main difference is that the A315 generates no secondary flow loop below the impeller. The tangential velocities in the outflow of the A315 are 50% lower than with the PBT leading to an increased pumping efficiency.

For all impellers the turbulence distribution is far from homogeneous, with high turbulence intensities in the outflow of the impellers and in the centers of the main circulation loops. It was found that the predicted overall energy dissipation rates compare reasonable with power measurements, but that with the ASM the predicted energy dissipation rates are about 15% higher than with the k-ε model. Thus for the prediction of turbulent mixing, the use of the ASM is necessary.

The use of single-phase flow pattern simulations as a basis for a description of the mixing processes in a stirred tank, can only be successful if the computations are done on a three-dimensional grid, with the aid of an anisotropic turbulence model.

CFD is a useful tool in the analysis of the flow in stirred mixing vessels. The computations in this paper have shown that it is even possible to discover flow features which otherwise would require very extensive sets of LDV measurements. A disadvantage at the present stage is that LDV data are required for prescribing impeller boundary conditions. Thus further research should concentrate on the development of accurate impeller models.

CHAPTER 4

A COMPUTATIONAL MODEL FOR THE GAS-LIQUID FLOW IN STIRRED REACTORS

ABSTRACT

In this chapter a model is described for calculating the gas-liquid flow in stirred vessels. The general-purpose code FLUENT is used for calculating the single-phase flow pattern. This flow pattern is used as input for an in-house code named GHOST! which calculates the distribution of the gas over the vessel on the basis of balance equations. A mathematical model for bubble break-up and bubble-coalescence, based on local turbulence intensity and local energy dissipation rate, is incorporated in this code. Details regarding modeling the impeller, bubble coalescence and bubble break-up are given in the paper. The GHOST! code is capable of calculating local void fraction, local bubble size, local interfacial area and local mass transfer. These local values can be integrated to yield the overall gas holdup and the overall mass transfer rate. There is a good agreement between computational results and measurements.

4.1 INTRODUCTION

The numerical computation of the flow field in stirred tank reactors has received attention since the beginning of the 1980's, starting with Harvey (1980) and Harvey and Greaves (1982a,b). Most times computations are limited to single-phase flow although stirred vessels are widely used for multiphase mixing. Full computation of the flow field of a liquid phase in which a gas is dispersed has not been possible so far. This was partly due to a lack of knowledge of bubble dynamics and the influence of bubbles on the turbulence structure, and partly due to computational restrictions.

In spite of the difficulties mentioned above, several attempts have been made to model the flow in a gassed stirred tank in a less rigorous way. Issa

and Gosman (1981) calculated the flow in a gassed stirred vessel equipped with a disc turbine. In their calculations they assumed a very small (0.5 mm), constant bubble diameter. Further they used very coarse grids and it was not possible to verify the results of their simulations because of a lack of experimental data.

Looney *et al.* (1985) presented a model for the turbulent flow of solid/liquid suspensions in stirred vessels. This model incorporated mass balance and momentum balance equations, together with a two-phase turbulence model. Although the model predicted the mean velocities for both phases reasonably well, the predictions of the turbulence intensities tended to separate from the experimental data. The predicted solids distributions could not be validated due to a lack of experimental data.

Pericleous and Patel (1987) calculated both the single-phase flow and the two-phase flow in a stirred tank. Their calculations were done for various impeller types and combinations of impellers. Due to the use of a simple one-equation turbulence model (based on the Prandtl mixing-length hypothesis), their velocity predictions had a limited accuracy only. Their two-phase calculations were done assuming a constant bubble size and a constant bubble slip velocity, and the results could not be verified with experimental data.

From 1986 onwards, Mann (1986, 1988) followed a different approach. He modeled the flow created by a disc turbine by a simple, 2-dimensional network of zones, and calculated the gas transport in this network by solving the continuity equation for the gas phase. Although his results are interesting and have a qualitative appeal, the simplified model of the flow pattern and the local turbulence makes extension of the model to other geometries difficult.

An extensive model was proposed by Trägårdh (1988). He incorporated the momentum exchange between the gas phase and the liquid phase, and models for local mass transfer and for the growth of microorganisms. However, his code was not capable of calculating the local bubble size and, like the other authors mentioned above, he did not take the influence of the turbulence on the bubble rise velocity into account.

In Chapter 2 it has been concluded that it is difficult to get insight in the processes occurring inside the gas-dispersion by measuring overall quantities. Since experimental measurements of the local gas holdup, bubble size etc. are very tedious and not always possible, there is a strong need of

models capable of calculating local gas holdup, local bubble size and local mass transfer rate.

In the current research project, the general purpose code FLUENT is used for calculating the single-phase flow in a stirred vessel equipped with either an axial flow impeller or a disc turbine (see Chapter 3). This flow pattern, including the turbulence distribution, is used as input for an in-house code named GHOST! (Gas Holdup Simulation Tool!) that calculates the distribution of the gas over the vessel on the basis of balance equations assuming that the influence of the gas on the liquid flow is negligible, which will be the case when the gas holdup is sufficiently low.

A mathematical model for bubble break-up and bubble coalescence, based on local turbulence intensity and local energy dissipation rate as calculated by FLUENT, is incorporated in this code. GHOST! is capable of calculating local values of void fraction, bubble size, interfacial area and mass transfer. Further details regarding the modeling steps are given below.

4.2 THE COMPUTATIONAL MODEL

4.2.1 Single-Phase Flow Pattern Computation

The single-phase flow pattern (liquid only) is calculated by solving the momentum equations and mass conservation equation with the aid of the general purpose code FLUENT. The Algebraic Stress Model (Rodi, 1980, Boysan, 1984) is used for calculating the turbulent Reynolds stresses. The computational procedures, grids, impeller boundary conditions etc. are all described in Chapter 3.

However, the assumption that the gassed linear liquid velocities are equal to the ungassed velocities

$$\vec{u}_{l,g} = \vec{u}_{l,u} \qquad (1)$$

will not be valid. It has repeatedly been reported that both the impeller power consumption (Chapter 2) and the pumping capacity of an impeller decrease on gassing. Joshi *et al.* (1982) proposed the following relation for this decrease in pumping capacity, assuming that the decrease in pumping capacity is proportional to the decrease in power consumption:

$$Fl_{l,g} = Fl_{l,u} \left(\frac{Po_g}{Po_u} \right) \quad (2)$$

Here $Fl_{l,u}$ and $Fl_{l,g}$ are the impeller pumping number in ungassed conditions and gassed conditions respectively. Po_u and Po_g are the ungassed and gassed power number. Thus, like Bakker and Van den Akker (1991), the gassed liquid velocities were calculated with:

$$\vec{u}_{l,g} = \vec{u}_{l,u} \frac{Po_g}{Po_u} \quad (3)$$

The values for Po_u and Po_g used here are experimentally determined values according to the measurement procedures described in Chapter 2. Further, the turbulence properties need to be corrected for the effects of gassing. Two effects are important. First, the energy dissipation rate decreases due to the decrease in the impeller power consumption. Second, there will be an increase in the energy dissipation rate due to the power input of the gas. The k and ε values as calculated by FLUENT for the ungassed conditions (ε_u and k_u) will be corrected for both effects.

The energy input per second for a single bubble P_b is given by:

$$P_b = \vec{F}_s . \vec{u}_s \quad (4)$$

Here $\vec{F}_s$ and $\vec{u}_s$ are the slip force vector and the slip velocity vector respectively. Therefore the total energy dissipation rate under gassed conditions will be:

$$\varepsilon_g = \varepsilon_u \left(\frac{Po_g}{Po_u} \right) + \frac{n_b P_b}{\rho_l (1-\alpha)} \quad (5)$$

In the computation of the turbulent kinetic energy under gassed conditions, the Taylor macro scale of turbulence is used:

$$L_t = \frac{k^{3/2}}{\varepsilon} \quad (6)$$

It is assumed that the turbulent kinetic energy which results from the energy input by the impeller has got the same Taylor length scale both under gassed

and ungassed conditions, in other words: the turbulence structure which results from the energy input by the impeller is not affected by the gas. Further it is likely that the energy input of the bubbles is dissipated through turbulent eddies containing the kinetic energy k_b and having a Taylor macro scale of the order of the bubble diameter:

$$d_b = k_b^{3/2} \left[\frac{n_b P_b}{\rho_l (1-\alpha)} \right]^{-1} \tag{7}$$

Now the following model equation for k under gassed conditions can be derived:

$$k_g = k_u \left(\frac{Po_g}{Po_u} \right)^{2/3} + \left[d_b \frac{n_b P_b}{\rho_l (1-\alpha)} \right]^{2/3} \tag{8}$$

Here d_b, α, ρ_l and n_b are the bubble diameter, the gas holdup, the liquid density and the bubble number density respectively. These model equations should be regarded as first order corrections and do not necessarily give a complete description of the physical mechanisms. For example, it is probable that the energy input by the gas bubbles will result in non-isotropic turbulence. However, the corrections for the influence of gassing on the mean velocities and the turbulence properties are small when the gas holdup is low. In this regime the model predictions are expected to be sufficiently accurate.

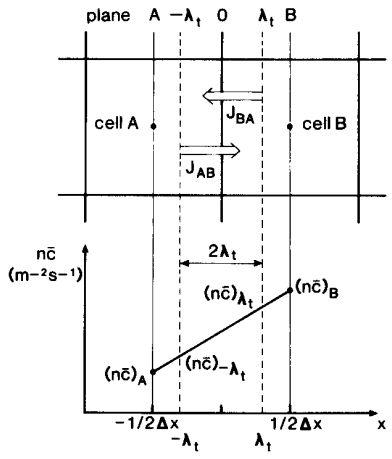

Figure 1 *Flux of random moving particles from cell A to cell B and vice versa*

4.2.2 Transport Equations for the Gas-Phase

The single-phase flow pattern as calculated by FLUENT is used for calculating the transport of the gas throughout the vessel using the model equations given below.

The continuity equation for the gas-phase reads:

$$\frac{\partial \alpha}{\partial t} + \vec{\nabla}.(\alpha\ \vec{u}_g) = S_g \tag{9}$$

Here $\vec{u}_g$ denotes the linear gas velocity and S_g is the gas source. In a stirred vessel S_g is non-zero at the sparger only. On performing the Reynolds decomposition and averaging the equation we get for a steady-state situation:

$$\vec{\nabla}.(\bar{\alpha}\ \bar{\vec{u}}_g) + \vec{\nabla}.\overline{(\alpha'\ \vec{u}_g')} = \bar{S}_g \tag{10}$$

The second term on the left-hand side describes the transport of gas due to the turbulent motion of the gas-phase and is not known in general. This leads to a so-called closure problem. This turbulent transport can be modeled on the analogy of the kinetic gas theory. Figure 1 shows the diffusional flux of randomly moving particles, as described by the kinetic gas theory (Pendlebury, 1985). In this figure n denotes the number density of the particles and $\bar{c}$ is the average of the fluctuating velocity of the particles. Further, λ_t denotes the so-called transport free path:

$$\lambda_t = C_\lambda \frac{1}{\sqrt{2}\ \pi\ d^2\ n} \tag{11}$$

where C_λ is a model constant of the order unity. The net particle flux J_{net} due to random motion from cell A to B is given by:

$$J_{net} = J_{AB} - J_{BA} = \frac{1}{4}\ (n\bar{c})_{-\lambda_t} - \frac{1}{4}\ (n\bar{c})_{\lambda_t} \tag{12}$$

GHOST! calculates the turbulent transport of the gas due to turbulent motion according to equation (12) where the average value of the particle velocity $\bar{c}$ equals the time average of the absolute value of the fluctuating component of the linear gas velocity:

$$\bar{c} = \overline{|\vec{u}_g'|} \tag{13}$$

When the equations are written out further, this model can be reduced to a diffusion type of closure, and equation (10) becomes:

$$\vec{\nabla}.(\bar{\alpha}\ \bar{\vec{u}}_g) - \vec{\nabla}.(\vec{\nabla}(\mathcal{D}\ \bar{\alpha})) = \bar{S}_g \tag{14}$$

The turbulent diffusion coefficient $\mathcal{D}$ is given by:

$$\mathcal{D} = \frac{1}{3}\lambda_t \overline{|\vec{u}'_g|} \tag{15}$$

Note that the turbulent diffusion coefficient in eq. (14) appears after the second $\vec{\nabla}$, thus reflecting the transport due to both gradients in mean gas holdup and due to gradients in the turbulence intensity. The latter effect has got its analogy in the kinetic theory of gases in a phenomenon called thermo-diffusion: diffusion due to gradients in temperature.

Further we assume that the average random fluctuating velocity of the gas phase is proportional to that in the liquid phase:

$$\overline{|\vec{u}'_g|} \sim \overline{|\vec{u}'_l|} \approx \sqrt{2k} \tag{16}$$

The linear gas velocity is calculated as the sum of the linear liquid velocity and the slip velocity between the two phases:

$$\vec{u}_g = \vec{u}_{l,g} + \vec{u}_s \tag{17}$$

Here $\vec{u}_{l,g}$ denotes the linear liquid velocity under gassed conditions. The computation of $\vec{u}_{l,g}$ was discussed in section 3.2.1. The slip velocity $\vec{u}_s$ can be calculated by a force balance on the bubbles (in (r, ϕ, z) coordinates):

$$-\rho_l V_b \frac{w^2}{r}\hat{r} - \rho_l g V_b \hat{z} = C_D \frac{1}{2}\rho_l |\vec{u}_s| \vec{u}_s \frac{\pi}{4} d_b^2 \tag{18}$$

Here V_b denotes the bubble volume, $\hat{r}$ is the unity vector in the radial direction and $\hat{z}$ is the unity vector in the axial direction. The force in the radial direction equals the centripetal force on the bubbles, while the force in the vertical direction is of course the buoyancy. The bubbles follow the main liquid flow in the circumferential direction.

The constant C_D is a function of the bubble Reynolds number and can be calculated from the correlations given by Morsi and Alexander (1972). Their correlations are strictly speaking only valid for particles moving in a stagnant liquid. To account for the influence of turbulence in our case, the bubble Reynolds numbers are calculated with a modified viscosity term.

This method was inspired by the work of Barnea and Mizrahi (1975) although these authors used the modified viscosity approach to correct for mutual hindrance effects in bubble clouds instead of for the influence of turbulence. The modified bubble Reynolds number is now given by:

$$Re_b = \frac{\rho_l \, |\vec{u}_s| \, d_b}{\eta_*} \tag{19}$$

Here η_* is the sum of the liquid viscosity and a term proportional to the turbulent viscosity:

$$\eta_* = \eta_l + C_* \, \rho_l \, \frac{k^2}{\varepsilon} \tag{20}$$

This extra term, incorporating the model constant C_*, is introduced to account for the decrease in slip velocity when a bubble is moving in a turbulent flow field instead of in a stagnant liquid. This decrease in slip velocity is due to the increased momentum transport around the bubble, and will be dependent on the ratio between the bubble size and the turbulent length scale. Thus C_* will be zero for bubbles smaller than the Kolmogorov length scale and will increase with bubble size. However, to prevent unnecessary complications the computations presented in this paper were performed with a constant value of C_*. Since not all turbulent eddies of all length scales will affect the momentum transport around the bubble, C_* will be smaller than the constant c_μ in the k-ε model described in Chapter 3.

4.2.3 Bubble Formation

The number of bubbles per dispersion volume n_b is related to the gas holdup and the average bubble volume in the volume element investigated:

$$n_b = \alpha / V_b \tag{21}$$

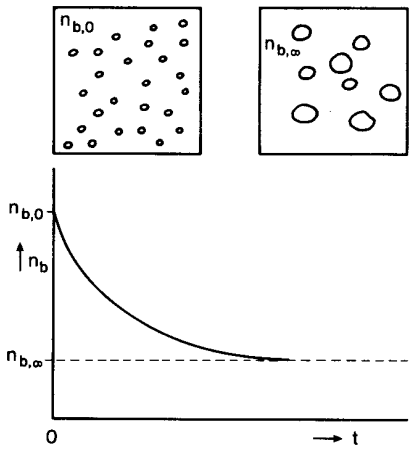

Figure 2 *Decrease in bubble number density in case the bubble formation process is coalescence dominated.*

The conservation equation for the bubble number density n_b reads:

$$\frac{\partial n_b}{\partial t} + \vec{\nabla}.(n_b \vec{u}_g) = \dot{n}_{b,c/b} + S_g/V_{b,in} \tag{22}$$

Here $\dot{n}_{b,c/b}$ denotes the change in n_b due to coalescence and breakup. An estimation for $\dot{n}_{b,c/b}$ can be made by performing some bubble cloud statistics. Think of a closed volume filled with a turbulent coalescing liquid containing a certain number of very small bubbles n_{b0}. Due to coalescence and breakup, the number of bubbles will gradually decrease, and the average bubble size will increase, until an equilibrium is reached at $n_{b\infty}$, see also figure 2. Such a process could be modeled assuming an exponential decrease in the number of bubbles:

$$\frac{\partial n_b}{\partial t} = \omega(n_{b\infty}-n_b) \tag{23}$$

In this equation ω denotes an average effective coalescence/breakup frequency. It is likely that this coalescence dominated process results in an average bubble size proportional to the maximum stable bubble size according to Hinze (1955):

$$d_{b\infty} = C_{b\infty} (12 \frac{\sigma}{\rho_l})^{3/5} \varepsilon^{-2/5} \tag{24}$$

A model constant $C_{b\infty}$ has been added in this equation. The bubble size in the outflow of the impeller directly calculated with equation (24), on basis of the average energy dissipation rate inside the impeller. Therefore $C_{b\infty}$ is estimated to be 0.4 from bubble size data reported by Greaves and Barigou (1988). Since the energy dissipation rate in the outflow of the impeller decreases faster than the bubble size can increase, the maximum stable bubble size in the bulk of the stirred vessel is larger than the average bubble size.

As a result the bubble formation process in the bulk is coalescence dominated. In this case the decrease in bubble number density is given by:

$$\frac{\partial n_b}{\partial t} = - X_c \, \ell \tag{25}$$

Here ℓ is the total number of bubble collisions, which can be calculated according to an analogy with the kinetic theory of gases:

$$\ell = \frac{3}{2} \sqrt{2} \, \frac{\alpha}{d_b} \, \overline{|\vec{u}'_g|} \, n_b \tag{26}$$

Further, X_c denotes the efficiency of the process. Only part of the collisions leads to coalescence. With increasing bubble size the chances that newly formed bubbles breakup again because they become too large will increase. Thus X_c will decrease when the ratio $n_{b\infty}/n_b$ increases. A first order approximation for X_c can be made:

$$X_c = C_\omega \left[1 - \frac{n_{b\infty}}{n_b} \right] \tag{27}$$

In this equation C_ω is a model constant the value of which depends, amongst other things, on the properties of the medium. The equations above can be combined to give the new conservation equation for n_b:

$$\frac{\partial n_b}{\partial t} + \vec{\nabla}.(n_b \, \vec{u}_g) = \omega \, (n_{b\infty} - n_b) + S_g / V_{b,in} \tag{28}$$

in which the average effective coalescence/breakup frequency is given by:

$$\omega = C_\omega \, \frac{3}{2} \sqrt{2} \, \frac{\alpha}{d_b} \, \overline{|\vec{u}'_g|} \tag{29}$$

Equations (28) to (29) are used for calculating the local bubble size in the bulk of the dispersion volume. The equations given above can also be combined to yield the equation for conservation of bubble volume:

$$\frac{\partial V_b}{\partial t} + \vec{u}_g.\vec{\nabla}V_b = \omega\, V_b\left(1 - \frac{V_b}{V_{b\infty}}\right) + \frac{1}{\alpha}\, S_g\, V_b\left(1 - \frac{V_b}{V_{b,in}}\right) \qquad (30)$$

4.2.4 Mass Transfer

When the local gas holdup and local bubble size are known, the mass transfer coefficient $k_l a$ can be calculated by using the equation for k_l given by Kawase and Moo-Young (1990):

$$k_l = 0.301\ (\varepsilon\nu)^{1/4}\ Sc^{-1/2} \qquad (31)$$

Sc is the Schmidt number. In the model equations given above it is assumed that the bubbles are spherical. The surface area of a spherical bubble is given by:

$$A_b = \pi\, d_b^{\,2} \qquad (32)$$

It is, however, more likely that the bubbles are ellipsoidal and have got a larger surface area than spherical bubbles. To check whether this suspicion is justified, the correlation of Wellek et al. (1966) for the ratio a/b between the long and short axis of an ellipsoidal bubble has been used:

$$a/b = 1 + 0.163\ Eo^{0.757} \qquad \left(Eo < 40;\quad \frac{g\,\mu^4\,\Delta\rho}{\rho^2\,\sigma^3} \le 1.10^{-6}\right) \qquad (33)$$

Here Eo denotes the Eötvös number, which is defined by:

$$Eo = \frac{\Delta\rho\ g\ d_b^{\,2}}{\sigma} \qquad (34)$$

The volume of an ellipsoidal bubble is given by:

$$V_b = \frac{4}{3}\,\pi\, a^2\, b \qquad (35)$$

The surface area of an ellipsoidal bubble can be calculated from:

$$A_b = 2\pi a^2 \left(1 + \frac{b}{a} \frac{\ln\left(a/b + \sqrt{a^2/b^2 - 1}\right)}{\sqrt{a^2/b^2 - 1}} \right) \qquad (0 < b/a < 1) \qquad (36)$$

Finally the local mass transfer coefficient per dispersion volume can be calculated from:

$$k_l a_d = k_l n_b A_b \qquad (37)$$

and the local mass transfer coefficient per liquid volume is given by:

$$k_l a = k_l a_d \frac{1}{1-\alpha} \qquad (38)$$

GHOST! reports the values for $k_l a_d$ and $k_l a$ as calculated assuming spherical bubbles, and as calculated assuming ellipsoidal bubbles. Since the ratio a/b is in general smaller than 1.3, the difference between the two methods was smaller than 1%.

4.2.5 The GHOST! Code

On basis of the equations above GHOST! (Gas Holdup Simulation Tool!) has been developed. GHOST! is a finite difference code, written in PASCAL, which is capable of calculating local values of void fraction, bubble size, interfacial area and mass transfer.

A flow scheme of GHOST! is given in figure 3. GHOST! starts with reading in the velocity-file. This is a FLUENT lineprint file converted to GHOST! format. This file contains the coordinates of the grid nodes, the mean velocities, k and ε.

The GHOST!-case file contains, amongst other things, the values of the model constants, the position of the sparger, the gas input, Po_u, Po_g, the properties of the liquid medium and the solution parameters. Important solution parameters are the convergence criterion, the maximum number of iterations and the under relaxation parameters.

The user can provide GHOST! with an initial guess for α and d_b assuming

homogeneous distributions, or a gas-file containing data from a previous calculation can be used. After the cell properties are calculated, the mean velocities and the k and ε values are corrected according to Po_g/Po_u.

In the main loop the important quantities are updated sequentially until the solution is converged. The convergence criterion used was that the relative change in α and d in successive iterations was smaller than 0.001 in each computational cell, and that the difference between the amount of gas escaping at the liquid surface and the amount of gas issuing from the sparger was also smaller than 0.1 %.

GHOST! generates two output files after the solution is converged. The gas-file contains the local values of α, d_b, k_la and $\vec{u}_s$. This file can be used as input file to provide GHOST! with an initial guess for further calculations but can also be converted to FLUENT format for graphics processing. The log-file contains the case file and a general list of results, as there are: the average values and maxima and minima of α, d_b, k_la, $d_b/d_{b\infty}$ and $\vec{u}_s$. Examples of other listed variables are: the rate of convergence, the values of several important quantities integrated over the impeller zone and the bubble size near the liquid surface.

The calculations can be performed on any type of 2D or 3D, uniform or non-uniform, cylindrical finite-difference grid. The staggered grid convention is used, which means that all the velocities are stored on the cell faces whereas the other properties are stored on the node centers. A first order upwind differencing scheme is employed for interpolation to the cell faces.

The computational algorithms are set up in a very flexible way and are not limited to any particular geometry, which means that a quick assessment of the influence of geometrical changes with respect to e.g. sparger position and impeller placement on gas holdup and mass transfer can be made.

4.3 EXPERIMENTAL

For the purpose of validation of the calculated gas holdup profiles, local gas holdup measurements were performed using a single-point optical fiber probe. The overall holdup was determined with the aid of an ultrasonic liquid level meter. The overall mass transfer coefficient k_la (per liquid volume) was measured with a dynamic method (Appendix A).

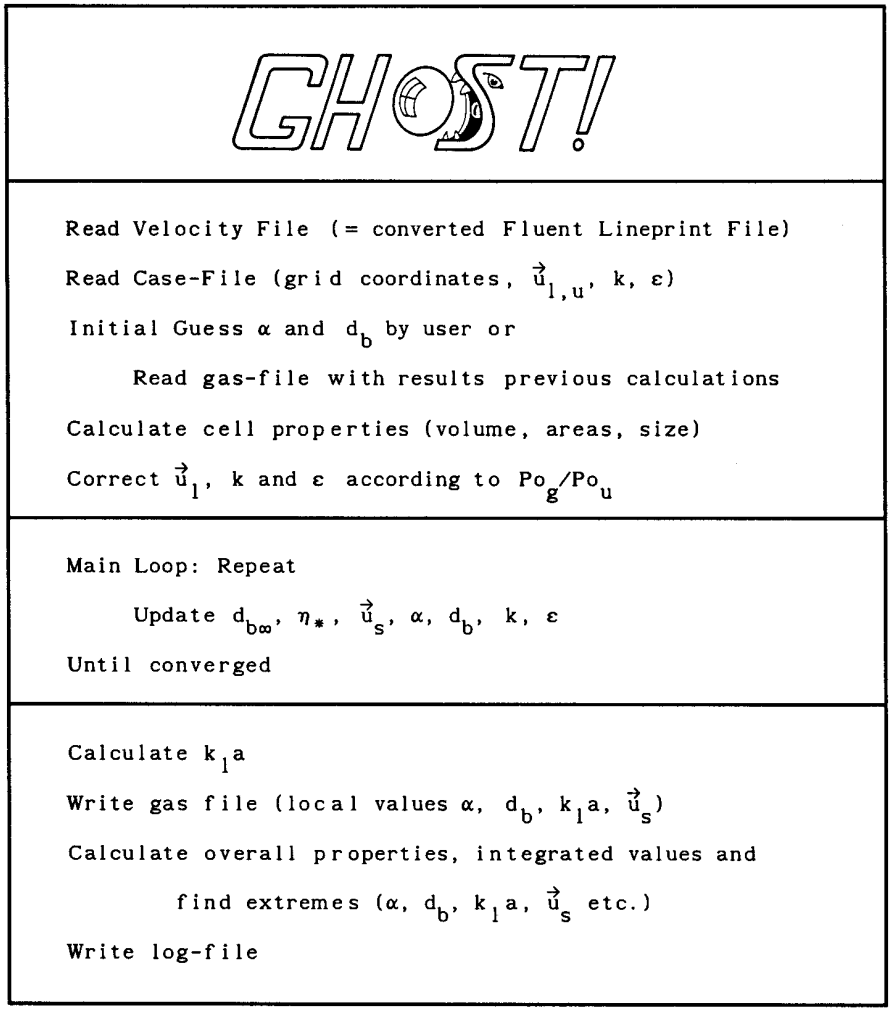

Figure 3 *Global flow scheme GHOST! (Gas Holdup Simulation Tool!).*

For measuring the bubble size an optical four point probe has been used. This measurement method was developed by Frijlink (1987), see also appendix B. However, due to the dimensions of this probe, bubbles smaller then 1.4 mm can not be measured. Further it is necessary that the probe is positioned in the direction of the main bubble flow. Due to this restrictions, the bubble size

could only be measured near the liquid surface. In this region the bubbles are large enough to be measured with the four point probe and the probe can easily be positioned along the direction of the main bubble flow.

All the experiments were done in perspex vessel of 0.444 m diameter. Impellers tested were a pitched blade impeller (PBT) with six blades, at 45° blade angle, a Lightnin A315 impeller, and a disc turbine (DT). Two sparger configurations were used, a large ringsparger (LRS, d_s/D = 0.75) mounted at a distance S = 0.6 D from the impeller and a small ringsparger (SRS, d_s=0.4 D) mounted at S = 0.2 D from the impeller. The impellers were mounted at a distance C = 0.75 D from the bottom. The impeller diameter was D = 0.4 T in all cases. The experimental details are listed in table 2. Both the A315 and the PBT were operated in the indirect loading regime. The PBT was tested at two different gassing rates.

Table 2 Experimental details. The computed values of $Fl_{l,g}$ are also listed. $Fl_{l,u}$ values are listed in Table 2 in Chapter 3.

	N(Hz)	V_{sg}(m/s)	P/V_l	Po_u	Po_g	Fl_g	$Fl_{l,g}$
1 DT (LRS)	5.55	0.0036	1520	5.00	3.59	0.019	0.55
2 A315 (LRS)	10.00	0.0036	1520	0.76	0.58	0.010	0.56
3 A315 (SRS)	9.95	0.0036	1520	0.76	0.59	0.010	0.57
4 PBT (LRS)	8.00	0.0036	1520	1.55	1.19	0.013	0.62
5 PBT (LRS)	8.00	0.0007	1950	1.55	1.52	0.002	0.79

Table 3 The model parameters used in the calculations presented in this Chapter.

C_*	$C_{b\infty}$	C_ω	C_λ
0.02	0.4	0.15	1.0

4.4 RESULTS

4.4.1 Overall Quantities

Several sets of model parameters were tested. The parameter set which gave the best results is listed in Table 3. It should be noted that Bakker and Van den Akker (1991) used C_ω = 0.2 instead of C_ω = 0.15 and $C_{b\infty}$ = 0.75 instead of $C_{b\infty}$ = 0.4. However, this led to under predicting the mass transfer coefficient $k_l a$, which is not the case with the present parameter set.

The simulations and the experimental data were found to match quite well, see Table 4. Both the overall gas holdup and the overall mass transfer coefficient $k_l a$ are predicted quite accurately, especially with the disc turbine and the PBT. With the A315 the predicted overall holdup is somewhat smaller than the measured one.

With the A315 the influence of sparger position was tested. Both experimental results and model calculations show that the overall gas holdup increases when the sparger is made smaller and mounted closer to the impeller. The experimental data show that the overall mass transfer coefficient also increases. This effect was already reported in Chapter 2 (see also Bakker and Van den Akker, 1990b) and was also found by Lally (1991). The model predictions, however, do not show this increase in $k_l a$ due to the fact that the increase in gas holdup leads to increased coalescence rates and thus to larger bubbles. This can be seen from the computed average

Table 4 Experimental and simulation results for the overall holdup (α), size bubbles leaving vessel ($<d_{b,out}>$) and the overall mass transfer ($k_l a$). The cases are numbered in the same order as in Table 2.

	α(%)		$<d_{b,out}>$(mm)		$k_l a$ (1/s)	
	Exp	Sim	Exp	Sim	Exp	Sim
1 DT	4.7±0.2	4.9	3.25	2.91	0.038	0.038
2 A315	4.6±0.2	4.2	3.76	3.59	0.035	0.036
3 A315	4.8±0.2	4.3		3.82	0.038	0.036
4 PBT	4.1±0.3	4.1	3.44	3.39	0.036	0.037
5 PBT	1.1±0.3	1.0		2.00	0.011	0.013

size of the bubbles which leave the vessel. As a consequence the interfacial area does not increase with increasing holdup in this case. This might mean that the coalescence rate model presented here shows a slightly too strong dependence on local holdup, but direct experimental verification is virtually impossible.

Note that although the gas holdup predicted with the disc turbine is quite high relative to the other two impellers, the difference in $k_l a$ between the impellers is smaller. This is due to the fact that with the DT most of the turbulent kinetic energy is dissipated in the relatively small volume around the impeller. A significant part of the gas in the vessel is thus found in regions with a low turbulence intensity and with low k_l values. These effects will be discussed in more detail in Chapter 5.

Part of the differences between the experimental data and the predicted data can be accounted for through experimental inaccuracies. In Table 4 the standard deviation in the measurements of the overall gas holdup is also listed. It is inevitable that the experimental data for the bubble diameter and the $k_l a$ contain inaccuracies also. However, the accuracy of these methods was difficult to estimate.

Further, certain assumptions in the model described above may also account for deviations between the model predictions and the experimental data. This will be discussed in more detail in section 4.5.

4.4.2 Local Gas Holdup

For verification of the modeling results measurements of the local gas holdup have been performed at various positions inside the vessel.

Figure 4 shows a comparison between the predicted local gas holdup and the experimentally determined values for the disc turbine. It can be seen that peaks in the gas holdup are found right above the sparger and in the lower circulation loop, near the vessel wall where gas and liquid are in counterflow. In general the predicted holdup profiles match the experimental data quite well, except in the upper part of the vessel near the shaft. According to the model predictions the holdup decreases in this region, something which is not confirmed by the experimental data. This might be due to an under predicted gas recirculation rate or, a too short recirculation loop.

The results for the A315 and the PBT are shown in figures 5 and 6. As

with the DT, peaks in the gas holdup are found near the sparger, and in the lower part of the vessel. Several regions can be distinguished. The predicted holdup profiles and the experimentally measured values match quite well in the lower part of the vessel near the wall. Good agreement is also achieved in the region above the impeller. Near the liquid surface the experimental and simulated profiles tend to separate. Visual observation of the vessel revealed that in this part of the vessel, the bubbles rise relatively undisturbed as if it were a bubble column. This might mean that in this region the gas-flow is strong relative to the liquid flow, and thus that the momentum transfer from gas to liquid can not be neglected.

Further, due to the fact that these axial flow impellers disperse the gas from strong trailing vortices (see figs. 5 and 6, below the impeller blade tip), peaks in the gas holdup are measured in the region which stretches from the impeller blade tip to the vessel bottom. Since no quantitative impeller model which predicts such vortices is available, these peaks could not be predicted. This leads to differences between the experimental data and the predicted profiles in this region.

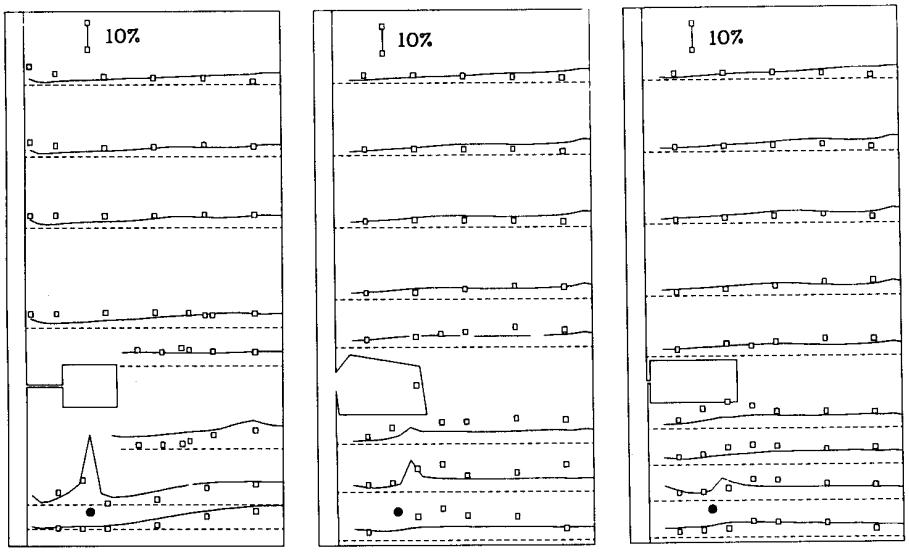

Figure 4,5,6 *Comparison between predicted and measured gas holdup profiles for the disc turbine, the A315 and the pitched blade turbine respectively. The black dot denotes the gas sparger. (□ experimental, —— simulation, ϕ = 45°, P/V = 1520 Wm^{-3}, v_{sg} = 0.0036 m/s,).*

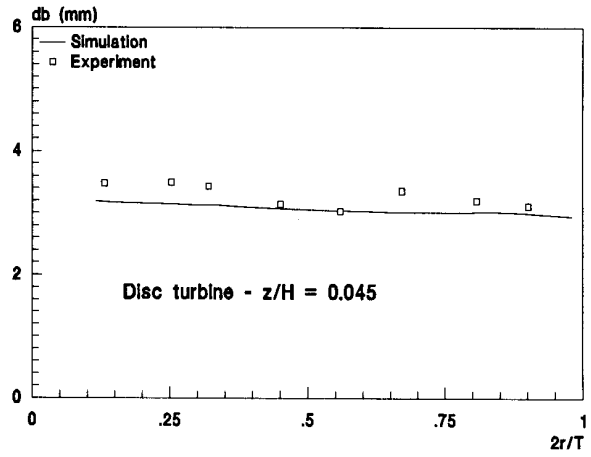

Figure 7 *Comparison between predicted and measured bubble size, disc turbine.*

4.4.3 Local Bubble Size

In figures 7, 8 and 9 the predicted bubble size and the experimentally determined bubble size are plotted as a function of the radial distance 2r/D at $\phi = 45^{\circ}$ and at z/H = 0.045 (P/V_l = 1520 Wm^{-3}, v_{sg} = 0.0036 ms^{-1}). All experimental data points are averages of 200 bubbles. It can be seen that GHOST! predicts for all three impellers that the bubble size increases slightly towards the shaft, as a result of coalescence. With the PBT and the A315 an increase in gas holdup is found near the shaft, where the liquid flow is directed downwards. This also leads to an increase in bubble size. The scatter in the experimental data points is too large to confirm this although in general there is a good agreement between the predicted bubble size and the experimental data.

Figure 10 shows a comparison between the experimental and predicted values of the bubble size near the vessel wall and near the liquid surface as a function of the circumferential coordinate ϕ. The simulations predict small three dimensional effects, with a local maximum in the bubble size at $\phi = 45^{\circ}$ (midway baffles). The experimental data do not show this maximum. However, the number of experimental data points is too limited for a detailed verification.

Figure 11 shows a measured bubble size distribution for the PBT. It can be seen that the bubble size distribution is fairly wide, with a standard deviation of 0.9 mm at an average bubble size of 3.3 mm.

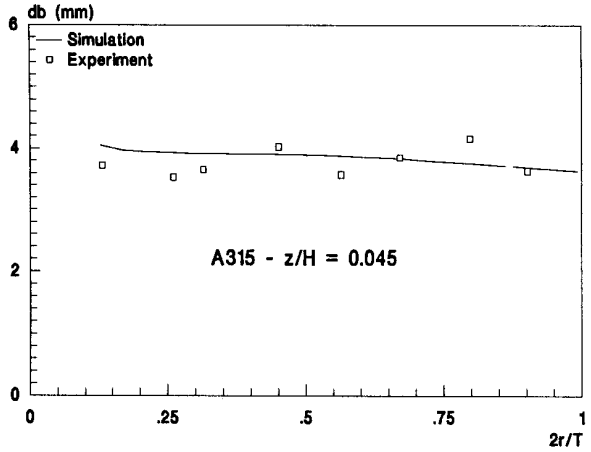

Figure 8 *Comparison between predicted and measured bubble size, A315.*

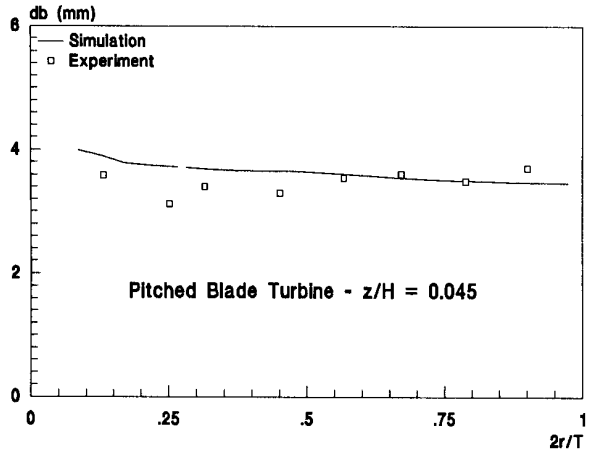

Figure 9 *Comparison between predicted and measured bubble size, PBT.*

Note that both the model predictions and the experimental data (see also table 4) show that there are significant differences in the size of the bubbles which leave the vessel. With the DT the bubble size is a bit smaller than with the axial flow impellers, due to the fact that with this impeller the gas bubbles first enter the impeller, which breaks them up, before they are distributed through the vessel. Further, the bubble path from the disc turbine to the liquid surface is shorter than from the sparger below an axial flow impeller to the liquid surface. Thus the bubbles have got less time to coalesce before they leave the vessel.

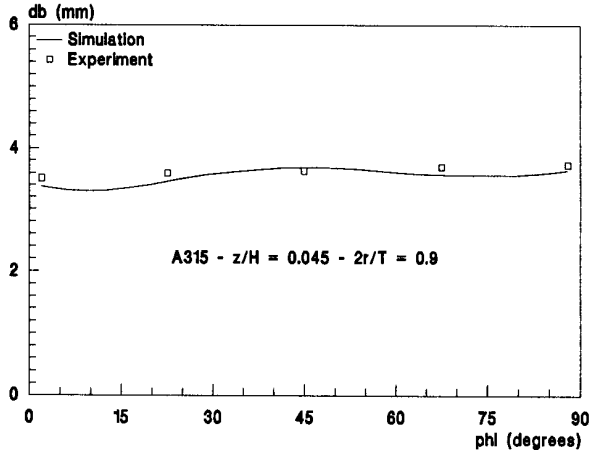

Figure 10 *Comparison between predicted and measured bubble size, A315*

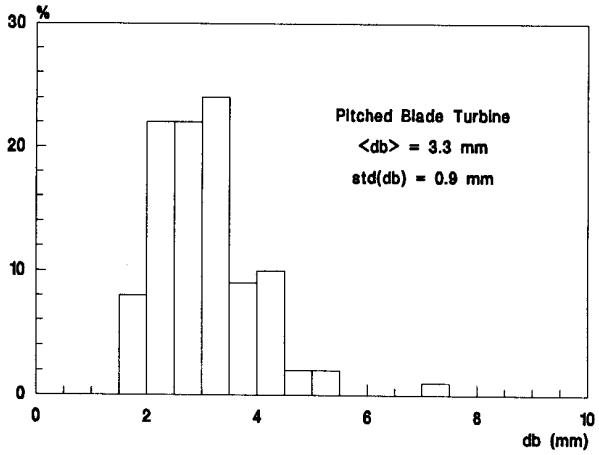

Figure 11 *Typical experimental bubble size distribution, PBT, ϕ = 45°, 2r/T = 0.9, z/H = 0.045*

The pitched blade turbine creates somewhat smaller bubbles than the A315. This might either be due to the lower gas holdup or to differences in the turbulence distribution, or both.

The fact that experimental and predicted values for $\langle d_{b,out} \rangle$ in table 4 do not quite match is partly due the fact that these averages are computed in

a different way. The experimental values are calculated as

$$\langle d_{b,out} \rangle = \frac{1}{N} \sum_{i=1}^{N} d_{b,i} \tag{39}$$

for all measured bubbles at z/H = 0.045 and ϕ = 45°. The predicted values are calculated as:

$$\langle d_{b,out} \rangle = \left[\frac{-1}{N_{b,out}} \int_0^{2\pi} \int_0^{R} \hat{z}.\vec{u}_g \; \alpha \; \frac{1}{V_b} \; d_b \; r \; dr \; d\phi \right]_{z=0} \tag{40}$$

Here $N_{b,out}$ denotes the total number of bubbles leaving the vessel per second. This surface integral gives the average diameter of all bubbles leaving the vessel.

4.5 DISCUSSION

A model has been presented with which local values of the gas holdup, bubble size, k_l, a and $k_l a$ can be calculated. The model predictions show an encouraging agreement with the experimental data. Depending on operating conditions the differences between the model predictions and the experimental results varies from 0% to ±20%. This means that this model can be used as a research tool, and when the results are handled with care also as a design tool.

The gassed stirred vessel is, however, a notoriously complex system. A lot of phenomena like bubble formation, turbulence, impeller pumping capacity, vortex shedding etc. have not been investigated in full detail.

As a consequence, the model presented in this paper had to be based on a number of assumptions. The most important assumption is that the influence of the gas on the liquid flow is small, and can be described with a decrease in pumping capacity of the impeller, the decrease being proportional to the decrease in power consumption of the impeller on gassing. As a result the model can only be applied with confidence at low gas flows. At higher gas flows both the momentum exchange between the gas flow and the liquid flow and a more advanced impeller model should be incorporated. The best way to model the impeller might be with the aid of experimental correlations for the

impeller pumping capacity as a function of the impeller speed and the gas flow through the impeller. When such data would be available, this would make the prediction of hydrodynamic transitions, such as the loading-flooding transition possible.

Another modeling problem is the way the gas is dispersed by the impeller. The experimental holdup data for the PBT and the A315 show that a significant amount of gas is dispersed from the trailing vortices, shed from the impeller blades. Unfortunately, the direct computation of the flow in trailing vortices is a far from trivial process, even in single-phase flow. As a consequence, models for the dispersion from such vortices will have to rely heavily on experimental data.

Further, in all the calculations steady-state flow is assumed. Bakker and Van den Akker (1990b), see also Chapter 2, already reported that at certain gassing rates with axial flow impellers transient flow patterns can occur. It will be clear that predicting the transient behavior of bubble clouds is still far away.

The model incorporates four model constants. The values of these constants have been chosen by comparing the simulation results for various parameter sets with the available experimental data. The number of data, however, is limited. To improve the accuracy of estimating the model constants, more experimental data for a wide range of situations should be made available.

It can be concluded that the model described in this paper is applicable, provided that the gas flow is low, as a tool to gain insight in the physical processes in the gas dispersion. For the prediction of hydrodynamic transitions and the flow at high gassing rates, the model should be extended further. Especially the quantitative modeling of the impeller remains a problem.

4.6 CONCLUSIONS

A model has been presented with which local values of holdup, bubble size and mass transfer can be calculated in a stirred vessel. All the model equations are incorporated in an in-house code named GHOST!, that is capable of performing both 2D and 3D computations on any type of cylindrical finite difference grid. The model allows for an assessment of effects on mass

transfer, gas holdup and bubble size of impeller type, impeller position, sparger position, aeration rate, etc.

The model predictions have been validated with experimental data regarding the local gas holdup, the local bubble size and several overall properties. In general, the model predictions compare quite well with the experimental data. In the outflow of the impeller the model predictions and the experimental data tend to separate, due to the lack of good impeller models.

Further research should concentrate on the development of suitable impeller models for gassed conditions and on the incorporation of the momentum exchange between the gas phase and the liquid phase. The estimation of the model constants also deserves further attention.

Experimental research in the area of gas-liquid mixing should concentrate on studying the local properties of the gas-liquid mixture.

The current state of the art in CFD makes the development of reliable two-phase codes possible, which can act as both a design tool and as a research tool.

CHAPTER 5

DESCRIPTION OF THE INTERNAL STRUCTURE OF STIRRED GAS-LIQUID DISPERSIONS

ABSTRACT

The internal structure of stirred gas-liquid dispersions has been investigated. Measurements of the local gas holdup were performed for different types of impellers under various circumstances. These data were combined with simulated data of the local gas holdup, local bubble size, local mass transfer rate and the local turbulence intensity to give an overall picture of the processes occurring in the stirred vessel.

It turns out that all impellers investigated create gas distributions which are far from homogeneous. Regions with a high gas holdup can exist close to regions containing very little gas. Due to the fact that the turbulence distribution is also far from homogeneous, the distribution of the mass transfer rate is also inhomogeneous. Peaks in the mass transfer rate are found in the outflow of the impellers, where both the gas holdup and the turbulence intensity are high. Low mass transfer rates are found in the liquid bulk. It is concluded that, given these inhomogeneous spatial gas and turbulence distributions, attempts to improve on the transfer rate should concentrate on trying to match the positions of the extremes of the spatial distributions.

5.1 INTRODUCTION

Despite a lack of knowledge about the processes occurring inside the gas-liquid dispersion in stirred vessels, a lot of researchers still concentrate on measuring and correlating overall quantities like the power

consumption and the overall gas holdup. This is not surprising since experimental determination of the local properties of the gas dispersion is a difficult and tedious task. However, the previous chapters have shown that the local mixing in a stirred tank can be unraveled by using a combination of advanced fluid flow modeling and modern experimental techniques.

Rather than being limited to measuring overall quantities, it is now possible to see how the internal structure of the gas-liquid dispersion is affected by a number of parameters. Important parameters are the impeller, the flow pattern it imposes and the power consumption. Further, several geometrical differences are important. Examples are the sparger position, the impeller to bottom clearance and the baffle geometry.

In this chapter the internal structure of the gas-liquid dispersion will be investigated. By combining experimental and simulation data about the local gas holdup, the local bubble size, the local interfacial area and the local mass transfer coefficient, a good picture about the processes occurring in the gas-liquid mixing vessel can be obtained.

5.2 LITERATURE

Due to the computational and experimental difficulties involved, only little information is available about the distribution of the gas and the local bubble size in stirred vessels. This is in sharp contrast with the number of papers which appeared about experimental studies to the single-phase flow pattern in stirred vessels, see for example the review by Ranade and Joshi (1990a).

Liquid velocity measurements in gassed stirred tanks were only recently performed by Patterson (1991). Although it is possible to measure both bubble velocities and bubble sizes with laser doppler velocimeters, this is still a very tedious measurement technique (Ohba *et al.*, 1986). Until now this technique has not been applied to the flow in gassed stirred vessels.

As a result of these experimental difficulties, design procedures and performance studies rely heavily on single-phase flow pattern studies (eg. Weetman *et al.*, 1986), performance comparisons based on the measurement of overall quantities (eg. Chapman *et al.*, 1983a and 1983b) and regime analyses (eg. Smith, 1985). The number of studies on the local gas-liquid flow in stirred gas-dispersions is still limited.

Nagase and Yasui (1983) reported local gas holdup measurements in the upper part of a vessel equipped with a disc turbine. The measurements were done with a suction probe and had a reported accuracy of 20%. According to their results, the liquid recirculation region above the impeller was smaller under gassed conditions than under ungassed conditions. They also reported a non-homogeneous gas distribution in this part of the vessel.

Greaves and Barigou (1988) reported local bubble size distributions, measured with the aid of a suction probe in a gassed stirred vessel equipped with a disc turbine. They showed that an increase in impeller speed resulted in a decrease in bubble size, whereas an increase in gassing rate had the opposite effect. These effects were stronger near the impeller than in the upper and lower regions of the vessel. Further they found that the shape of the bubble size distribution differed considerably from a normal distribution.

Mann and Hackett (1988) presented a model for calculating the local gas holdup in a stirred vessel equipped with a disc turbine. According to his simulations, the gas distribution in the mixing vessel was inhomogeneous with a low gas holdup below the impeller.

Hutchings *et al.* (1989) used the particle tracking option of FLUENT to show that the A315 impeller gave a better gas recirculation than the standard disc turbine.

Patterson (1991) performed LDV experiments under gassed conditions in a turbine stirred tank. It turned out that the axial liquid velocities near the tank wall increased on gassing. Further he used the particle tracking model incorporated in FLUENT for calculating the local gas holdup, but this led to an over prediction of the overall gas holdup.

5.3 METHODS OF ANALYSIS

In this Chapter the gas dispersion will be analyzed both computationally and experimentally. The gas-liquid flow simulations are all done with GHOST! (Gas Holdup Simulation Tool!), the code described in Chapter 4. GHOST! calculates the distribution of the gas in a stirred mixing vessel based on conservation equations and single-phase flow patterns calculated with the general fluid flow code FLUENT

In the experimental studies a single-point glass fiber probe was used

for measuring the local gas holdup. Bubble sizes were measured near the liquid surface with a four-point glass fiber probe (Appendix B).

A flat-bottomed stirred tank being 0.444 m in diameter was used in these investigations. This vessel was equipped with four baffles with a width W = 0.077 T and mounted at a distance of 0.023 T from the wall. Three impellers were tested, a disc turbine (DT), a pitched blade turbine (PBT) and a Lightnin A315 impeller. Two spargers were tested, a small ringsparger (SRS, d_s/D = 0.4) and a large ringsparger (LRS, d_s/D = 0.75).

The measurements and simulations were done at a superficial gas velocity of v_{sg} = 3.63E-3 m/s and an overall power consumption of P/V_l = 1520 W/m^3, unless noted otherwise. The cases studied are listed in more detail in table 2, Chapter 4.

In these studies, the A315 and the PBT were operated in the indirect loading regime with vortex/growing cavities (Chapter 2). The disc turbine was operated in the loading regime, with vortex/clinging cavities (Smith, 1985).

5.4 LOCAL GAS HOLDUP

It has been shown in Chapter 2 that various flow regimes can be distinguished in gassed mixing vessels. The present work is only concerned with those flow regimes in which the gassed flow pattern is steady and in which the gas is well dispersed. In this regime, the gas distribution is mainly determined by the liquid flow pattern as imposed by the impeller. As a result, different impellers will yield different gas distributions.

In Chapter 3 the flow patterns of both the PBT and the A315 impeller have been described. Both impellers generate a strong downwards directed axial flow, with a large main circulation loop, and a second recirculation loop in the upper part of the vessel, with downwards directed liquid velocities near the tank wall.

Figure 1 shows the experimentally determined local gas holdup for the A315 impeller with two different ring spargers, mounted at different positions. Several important features can be recognized. First of all it is clear that the gas distribution is far from homogeneous. The strong circulation loop in the lower half of the vessel results in a relatively high gas holdup in this region, whereas very little gas is found in the upper part of the vessel. The impeller tends to suck in the gas from the side, and

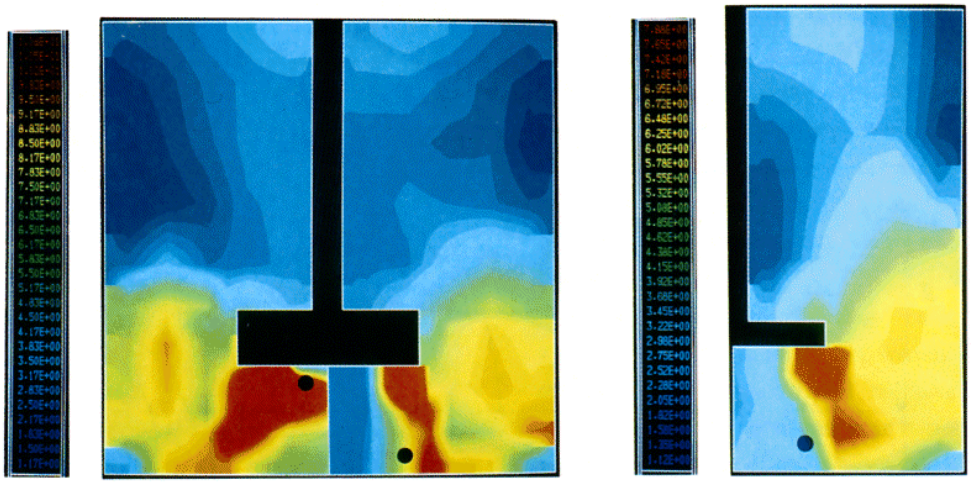

Figure 1a,1b,2 Local gas holdup, experimental,

A315-SRS, A315-LRS, PBT-LRS (V_{sg} = 0.0036 m/s).

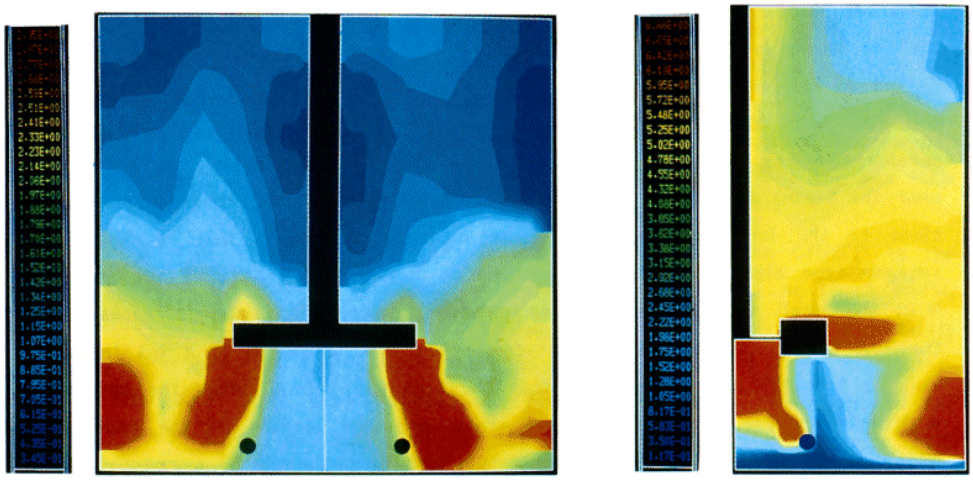

Figure 4b,4a, 6 Local gas holdup, experimental,

PBT-LRS-behind baffle, PBT-LRS-midway baffles (V_{sg} = 0.0007 m/s)

DT-LRS (V_{sg} = 0.0036 m/s).

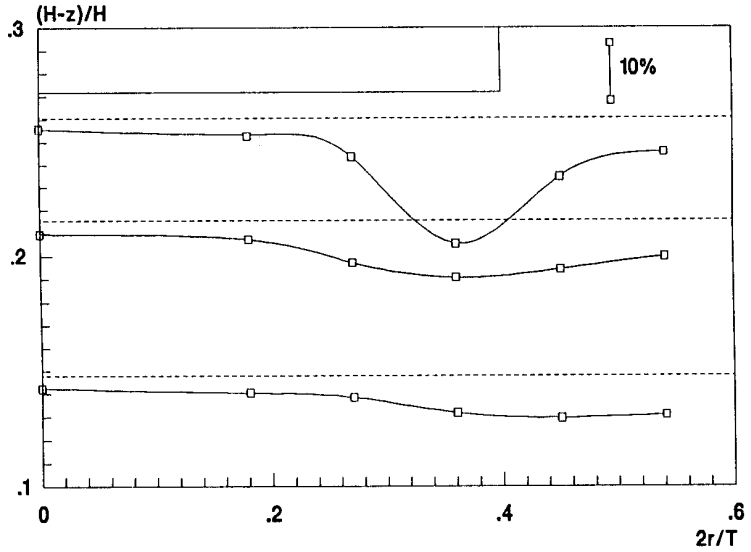

Figure 3 *Profiles of local gas holdup in the outflow of the pitched blade turbine, experimental data, ϕ = 45°, P/V_l = 1520 Wm^{-3}, v_{sg} = 0.0036 m/s*

disperses it from the trailing vortex near the impeller blade tip. A peak in the gas holdup is also found in the center of the lower circulation loop.

The sparger type has got a significant influence on the distribution of the gas. With the large ringsparger mounted close to the vessel bottom a considerable region with a very low gas holdup is found below the impeller, near the vessel center. On the other hand, the use of a small sparger mounted close to the impeller results in quite a large holdup in this region. The sparger type also influences the gas holdup in the upper part of the vessel. With the small sparger the gas recirculation recirculation rate decreases and the low gas holdup region in the upper part of the vessel is a bit larger. This is probably due to the fact that the high gas holdup below the impeller with this sparger, imposes a higher static pressure loading on the impeller, which might result in less pumping action and consequently in a reduced gas recirculation rate. This means that the net effect of sparger type on the overall gas holdup is quite small: the overall holdup is 4.8 % for the SRS and 4.6% for the LRS.

The gross characteristics of the gas distribution with the PBT are the same as with the A315 (fig. 2). The gas holdup is again low near the center

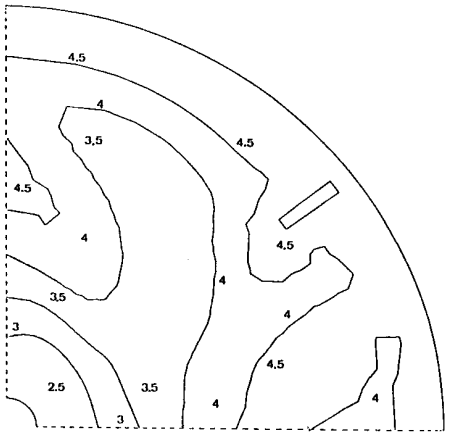

Figure 5 *Local gas holdup for the pitched blade turbine, top view, GHOST!-simulation, numbers denote minimum values in areas enclosed by contours, z/H = 0.66 (just above impeller), 1520 Wm^{-3}, v_{sg} = .0036m/s*

of the vessel, below the impeller, and high in the outflow of the impeller. The gas recirculation loop is a bit larger than with the A315. As with the A315 the gas is mainly dispersed from the trailing vortex at the impeller blade tip, see also figure 3.

A decrease in gassing rate, v_{sg} = 0.70E-3 m/s (fig. 4a) instead of 3.63E-3 m/s, was found to have only a small influence on the distribution of the gas. Behind the baffle (fig. 4b) a high gas holdup is found near the vessel wall. This is probably due to the vortexing action behind the baffle. It is also interesting to see that with the PBT a peak in the gas holdup is found just above the impeller blade tip. Visual observation of the vessel revealed that sometimes vortices are created behind the baffle, above the impeller, which disappear into the impeller and probably interact with the trailing vortex behind the impeller blades. In fact this means that the trailing vortices behind the impeller blades can have an upstream influence on the gas-liquid flow, provided that the gas flow rate is low.

Figure 5 shows the local gas holdup as calculated with GHOST! in the plane above the impeller (z/H = 0.66). It can be seen that at small radial distances the gas distribution above the impeller is approximately axisymmetric, but that this is not the case near the baffles.

The main differences between the gas distribution of the A315 and the PBT result from the fact that at the same power consumption the A315 generates a stronger axial flow than the PBT. This can be seen from the fact that with the A315 the jet coming from the impeller blades reaches the vessel bottom, whereas with the PBT the gas flow is more radially directed. Further the larger axial liquid velocities with the A315 lead to a larger recirculation rate, and consequently to a somewhat larger overall gas holdup than measured with the PBT.

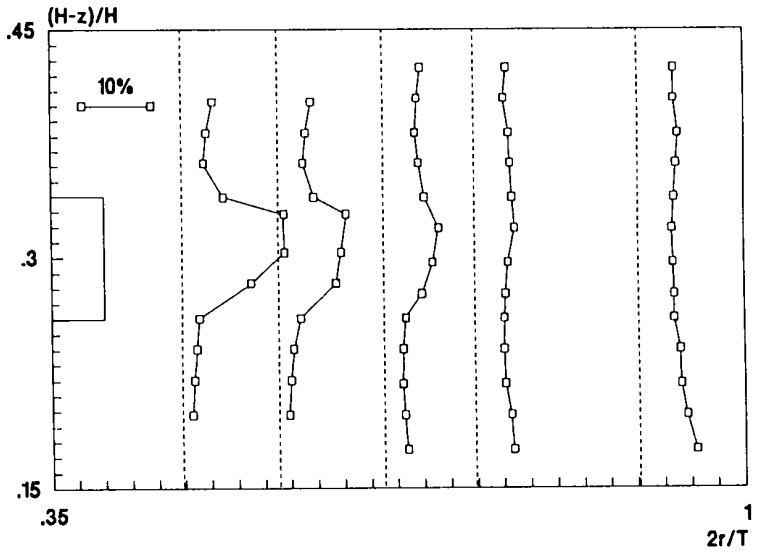

Figure 7 *Profiles of local gas holdup in the outflow of the disc turbine, experimental data, ϕ = 45°, P/V_l = 1520 Wm^{-3}, v_{sg} = 0.0036 m/s*

The single-phase flow pattern generated by the radially pumping disc turbine consists of two main circulation loops, one on either side of the impeller. The gas distribution with a disc turbine differs considerably from that with an axial flow impeller (fig. 6), although with the disc turbine the gas dispersion is far from homogeneous as well. The gas holdup is high in the outflow of the impeller (see also fig. 7), and extremely low in the region stretching from the blade tip to the vessel bottom. Due to the strong rotation in the neighborhood of the impeller, the gas issuing from the sparger moves inwards. This leads to a high gas holdup in the center of the vessel below the impeller. Another interesting feature is that a high gas holdup is found near the vessel wall, in the lower part of the vessel. This is due to the fact that the gas and the liquid are in counterflow in this region. Further it should be noted that near the liquid surface, the gas holdup increases towards the shaft due to centripetal forces.

Figure 7 shows the gas holdup in the outflow of the disc turbine. It can be seen that near the impeller blade the gas holdup profiles are asymmetrical, with a larger gas holdup near the top of the impeller. This means that more gas is distributed from the top of the cavity than from the bottom.

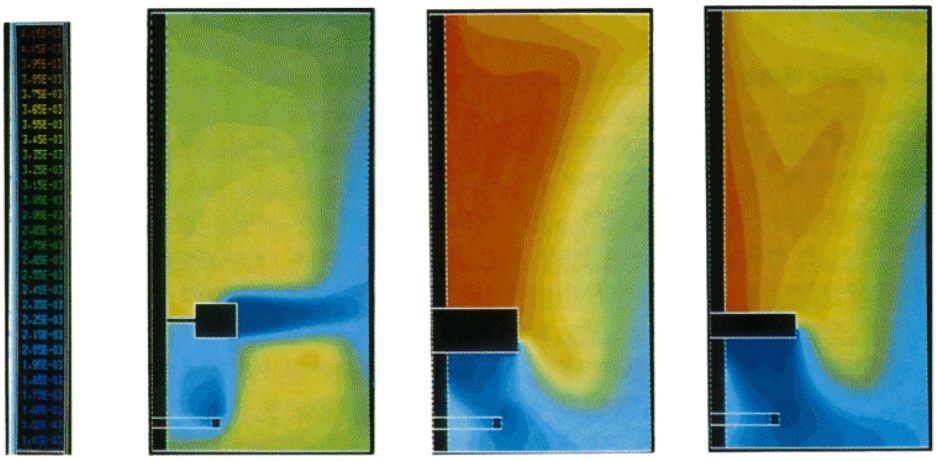

Figure 8,9,10 Bubble size simulation, DT, A315 and PBT.

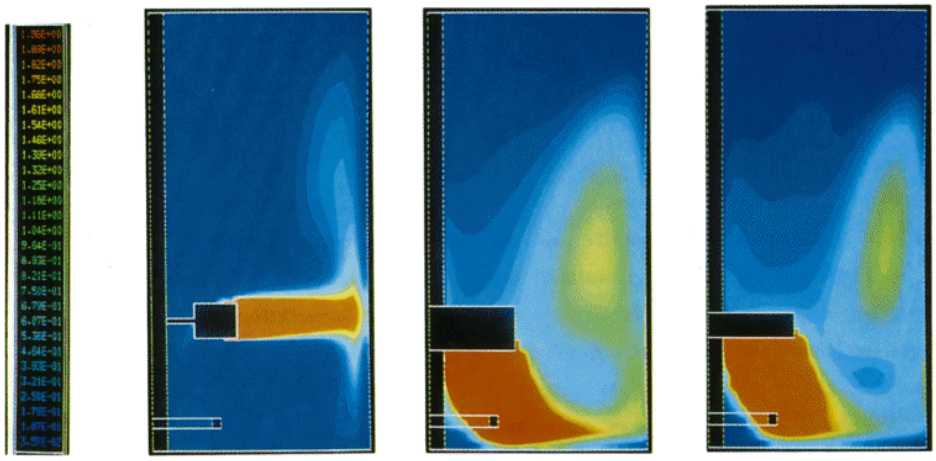

Figure 11,12,13 Energy dissipation rate, simulation, DT, A315 and PBT.

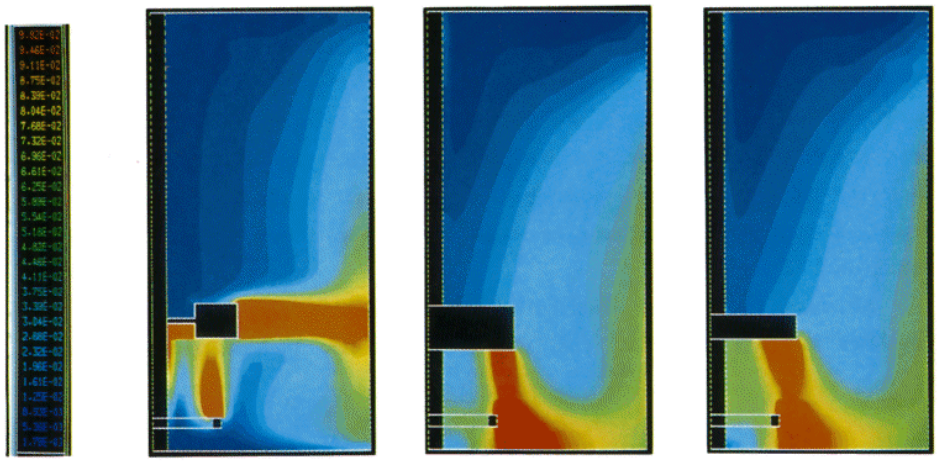

Figure 15,16,17 Mass transfer rate, simulation, DT, A315 and PBT.

5.5 LOCAL BUBBLE SIZE

According to the model presented in Chapter 4 the local bubble size is determined by several mechanisms and quantities.

Especially important are the local gas holdup and the turbulence intensity. A high gas holdup leads to large coalescence rates because of the large number of bubble collisions. A high turbulence intensity (read: the kinetic energy contained in the eddies with a wave-length of the order of magnitude of the bubble diameter) will lead to increased bubble break-up, but also to increased coalescence as a result of an increase in the number of collisions. It will depend on the bubble size, the maximum stable bubble size, the gas holdup and the turbulence intensity which of the two mechanisms dominates.

A small bubble size leads to reduced slip velocities, which leads to an increase in gas holdup and consequently to an increase in bubble collision and coalescence rate. Further, the impeller breaks up the gas bubbles, and acts as a source of small bubbles. Thus there are several mechanisms interacting, some of them mutually counteracting. The final spatial bubble size distribution is a complex function of the convective bubble transport, bubble break-up by the impeller and the local turbulence intensity.

Figure 8 shows the simulated local bubble size for a disc turbine. Due to the experimental difficulties involved these simulations could only be verified near the top surface of the vessel, in which region the simulations matched the experimental data quite well (Chapter 4).

Figure 8 clearly shows that bubble size is smallest in the outflow of the impeller. As a result of coalescence, bubble size increases along the main circulation loops in the upper part of the vessel. Large bubble sizes are also found in the high gas holdup region in the lower part of the vessel, near the tank wall. The bubble size is smaller again near the sparger and in the low gas holdup region, extending from the impeller tip to the vessel bottom. This overall picture of the local bubble size is confirmed by the data presented by Greaves and Barigou (1988). Their experimental data also show the increase in bubble size near the tank wall in the lower part of the vessel, a fact which can now be explained for in terms off the high gas holdup in this region.

Although the spatial distribution of the bubble size with axial flow impellers is quite different from that with the disc turbine, bubble size is

determined by the same mechanisms. From figures 9 and 10 it can be seen that with both the A315 and the PBT bubble size is small in the outflow of the impeller and that, as with the disc turbine, bubble size increases along the main circulation loop, due to coalescence.

This can further be illustrated by looking at the maps of the turbulence intensity, of which the turbulent energy dissipation rate is a measure, see figs. 11, 12 and 13. Although for all three impellers the bubble size is small in the region with a large energy dissipation rate (the outflow of the impeller) there is no direct link between the bubble size and the energy dissipation rate in the liquid bulk. As expected, in so-called coalescing systems, like air water, bubble break-up occurs mainly in the impeller region and bubble coalescence is the dominating mechanism in the liquid bulk, with the local gas holdup and local turbulence intensity determining the effective coalescence rate.

This effect is illustrated by the bubble size near the liquid surface. From figure 14 it can be seen that in this region the smallest bubbles are found with the disc turbine. This is due to the fact that with the disc turbine, all the gas first enters the impeller before it is distributed through the vessel, and the relatively short path the bubbles have to follow to get near the liquid surface.

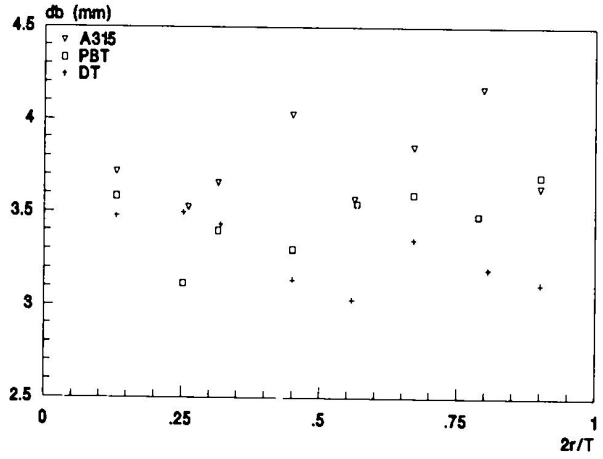

Figure 14 *Experimental bubble size near liquid surface, impeller comparison, z/H = 0.045, ϕ = 45°, P/V = 1520 Wm^{-3}, v = 0.0036 m/s*

5.6 LOCAL MASS TRANSFER RATE

The local mass transfer rate k_la is determined by both the local values of the interfacial area a and the mass transfer coefficient k_l. The local value of the interfacial area follows from the local gas holdup and the local bubble size, which are each described in the previous sections. The mass transfer coefficient k_l does not so much depend on the bubble properties. Since the main resistance for mass transfer is on the liquid side it is mainly the local turbulence intensity which determines k_l. Since the process of surface renewal in the stagnant liquid film around the bubble will depend on the small scale turbulence, Kolmogorov's theory can be used to derive an equation for k_l in which k_l is proportional to the turbulent energy dissipation rate ε to the power 1/4 (Kawase and Moo-Young, 1990). The k_la maps will be compared with the maps of ε, to be able to see the influence of the local turbulence.

Figure 11 shows the local energy dissipation rate for the disc turbine, while figure 15 shows the local mass transfer rate. It can be seen from figure 11 that the energy dissipation rate is very high in the outflow of the impeller, and decreases fast along the circulation loops. The highest k_la values are also found in the outflow of the impeller because of the high gas holdup and the small bubbles. Due to the fact that along the circulation loops the bubble size increases and at the same time the energy dissipation rate decreases, k_la also decreases along these loops. A peak in k_la is further found in the high gas holdup regions in the outflow of the sparger.

The complex flow structure generated by the pitched blade turbine leads to a more complex distribution of the energy dissipation rate than with the disc turbine. It can be seen from figure 13 that ε is high in the outflow of the impeller, but that there is also a significant amount of turbulence generation in the upper part of the vessel, due to three dimensional flow effects. As a result, the turbulence distribution for the pitched blade turbine is somewhat more homogeneous than with the disc turbine. The conclusions drawn for the disc turbine can, however, also be applied to the pitched blade turbine. Because of the combination of a high turbulence intensity with a high gas holdup, made up of small bubbles, the mass transfer rate is very high in the outflow of the impeller. In the liquid bulk, where the energy dissipation rate is low, and the bubble size has increased due to coalescence, lower k_la values are found (fig. 17).

The overall picture of the A315 is very much the same as with the pitched blade turbine. Also with the A315 the highest turbulence intensities and $k_l a$ values are found in the outflow of the impeller (figure 12, 16).

Since the spatial distributions described before are non-homogeneous, there is a need for quantification of the degree of non-homogeneity. Although it may seem possible to use the maxima and minima in the spatial distributions for this purpose it should be borne in mind that peak values follow from local events, eg. vortex formation, and are not necessarily a measure for the rate of homogeneity throughout the vessel. Further, it is very likely that peak values are grid dependent. As a result, it was decided to compare values integrated over the impeller volume for getting an impression of the degree of homogeneity.

Since with all three impellers the highest $k_l a$ values were found in the outflow of the impeller, the fraction of the overall mass transfer which takes place in the outflow of the impeller has been calculated. For the disc turbine the volume from the shaft to the vessel wall, just including the impeller has been taken. For the pitched blade turbine and the A315 the volume from the top of the impeller, extending to the vessel bottom is used.

Table 1 shows the liquid volume of the impeller outflow $V_{l,io}$, the gas holdup $V_{g,io}$, the mass transfer rate in the impeller outflow $k_l a_{io}$, and the integrated energy dissipation rate ε_{io}, each as a percentage of the overall values.

The data in Table 1 clearly show that each impeller creates inhomogeneous spatial distributions, especially with respect to the energy dissipation rate. It can be seen that for all three impellers a significant portion of the overall mass transfer takes place in the outflow of the impeller. For the disc turbine almost 1/3 of the overall mass transfer takes place in just 7.8 % of the liquid volume. For the axial flow impellers these values are lower, showing the effects of the less inhomogeneous turbulence distribution.

It is interesting to see that the historic development of impellers, from the DT to the PBT and later to the A315, is towards impellers which create less inhomogeneous spatial distributions.

Table 1 Liquid volume, gas volume, mass transfer rate and energy dissipation rate in the impeller and the outflow of the impeller as a percentage of the whole. Data from computer simulations with FLUENT and GHOST!.

	$V_{l,io}$(%)	$V_{g,io}$(%)	$k_l a_{io}$(%)	ε_{io}(%)
DT	7.8	10.1	31	87
PBT	4.9	4.8	14	68
A315	5.0	4.3	12	59

5.7 DISCUSSION

The spatial distributions of various important quantities have been studied experimentally and by means of computer simulations. The main conclusion which can be drawn is that the spatial gas distribution is far from homogeneous for all three impellers investigated. Although at a first glance, this might seem a problem, that is not necessarily the case since the turbulence distribution generated by the impellers is also inhomogeneous. Since it is the local turbulence intensity at small turbulent length scales which determines the value of the mass transfer coefficient k_l it is advantageous to concentrate the gas in regions with a high turbulence intensity. In fact, this is why the disc turbine is capable of creating a mass transfer rate as high as that of the axial flow impellers, despite the relatively weak liquid flow, since with this impeller all the gas enters the impeller before it is dispersed.

It is also interesting to see that a strong liquid flow, as generated by the A315, does not necessarily lead to a more homogeneous gas distribution. It turns out that with the A315, and also with the PBT, a strong gas recirculation loop in the lower part of the vessel is formed. This results in a high gas holdup in this region. The gas holdup in the upper part of the vessel, however, is relatively low. It would be interesting to see how the gas distribution would change when a second impeller would be added.

It is doubtful if it will ever be possible to create a gas dispersion in

a stirred vessel which is really homogeneous. There will always exist regions where gas and liquid are in countercurrent flow and regions where both phases are in cocurrent flow. This fact, in combination with pressure differences and centripetal forces, inevitably leads to spatial variations in the local gas holdup.

A similar argument can be applied to the turbulence distribution. The turbulence levels in the impeller region will always be higher than in the liquid bulk due to blade friction and vortex formation, even though carefully designed profiled blades can increase the energetic efficiency of the impeller.

The overall mass transfer rate follows directly from the spatial distribution of $k_l a$. Since the $k_l a$ distribution is directly linked to the local α, d_b and ε values, optimization of the mass transfer performance will have to concentrate on matching the positions of the extremes in these spatial distributions. Given the fact that the gas distribution will always be non-homogeneous, the turbulence distribution should also be non-homogeneous, and vice-versa.

This does, however, not imply that one should aim at creating non-homogeneous gas and turbulence distributions. As a guideline one should aim at creating a mixture which is as homogeneous as possible, making use of the knowledge that full homogeneity will never be achieved in the optimization process.

It is not useful to design a system which is optimized with respect to one of the variables mentioned above. For example, a homogeneous turbulence distribution may well be disadvantageous when the α and d_b distributions are not adjusted accordingly. This is a difficult task, since the interaction between α, d_b and ε is very complex. Computer simulation is probably the only practical solution to this problem.

This principle of optimizing $k_l a$ by matching the positions of extremes happens, to some extent, automatically with the disc turbine, since with this impeller the input gas will always be dispersed from the impeller before leaving the vessel. With axial flow impellers this is not necessarily the case, and the mass transfer performance can be improved by adjusting the positions of the impeller and the sparger. The use of special sparger types, which generate small bubbles at the gas inlet should also be considered, especially with axial flow impellers. It will be clear that the improvements in mass transfer rate which can be expected are larger with non-coalescing

liquids, since then an increase in turbulence intensity will not necessarily lead to an increase in coalescence rates and bubble size.

In general it can be concluded that there is room for further optimization of stirred vessels with respect to mass transfer. There is no physical reason why the overall mass transfer rate should only depend on the overall power consumption and the overall gas input. There are, however, several opposing mechanisms which dampen out the effects of large changes in the flow structure on the overall mass transfer rate. Examples are the decrease in impeller pumping capacity at a high pressure loading, and increased coalescence at high turbulence intensities and small bubble sizes.

The improvements which can be expected are in the order of magnitude of 5%-10% around the average. Since these improvements are only little higher than the inaccuracies in the present $k_l a$ measurement methods and computer simulations, more fundamental research remains necessary.

5.8 CONCLUSIONS

The gas dispersion in a stirred mixing vessel has been investigated both experimentally and computationally.

The spatial distributions of the important quantities (gas holdup, bubble size, mass transfer rate and turbulence) are all far from homogeneous. This seems to be a fundamental property of gassed stirred tanks.
With all three impellers investigated, the highest mass transfer rates are found in the outflow of the impeller.

With the disc turbine almost 1/3 of the total mass transfer rate takes place in the impeller outflow. With the axial flow impellers the spatial $k_l a$ distribution is a bit more homogeneous, leading to about 14% of the total mass transfer taking place in the impeller outflow.

In the investigated flow regimes, with the A315 and the PBT, the gas is dispersed from the trailing vortices shed from the impeller blades. Peaks in the holdup are found in these vortices. At low gassing rates, peaks in the holdup are also found just above the blades of the PBT, indicating that these vortices also have got an upstream effect on the gas-liquid flow.

The outflow of the disc turbine is asymmetric. The gas holdup is higher at the top of the impeller.

Mass transfer performance can be improved by matching the positions of the extremes in the spatial distributions of the important quantities. The knowledge that full homogeneity will never be achieved should be used in the design and optimization process.

The approach followed in this paper, combining CFD with local measurements important quantities, seems to be the only method to gain further insight in the processes occurring in a stirred tank.

APPENDIX A

THE K_LA MEASUREMENT METHOD

A.1. General description

Transport of a gas, mostly oxygen, from the gas phase to the liquid phase is the primary goal of gas-liquid mixing. The Oxygen Transfer Rate (OTR) is given by:

$$OTR = k_l\, a\, (\frac{c_g}{m} - c_l) \qquad (1)$$

Here k_l denotes the liquid side mass transfer coefficient, a is the specific surface area per liquid volume (m^2/m^3), c_g and c_l are the oxygen concentration in the gas phase and liquid phase respectively, and m is the partition coefficient. Since it is difficult to measure k_l and a separately, they are usually taken together in the total mass transfer coefficient k_la. There are several methods to measure k_la. The method chosen here is a dynamic method. In this method the stirred vessel is first gassed with nitrogen, to remove the oxygen from the liquid phase. At t = 0, when the oxygen concentrations in both the gas-phase and and the liquid phase are zero, the gas input is switched from nitrogen to air. The response of the oxygen concentration in the liquid phase is then measured with an oxygen probe. Analysis of this signal allows for determining the mass transfer coefficient k_la. Several methods are available to analyze this signal.

A.2. First order model.

The transport of oxygen from the gas-phase to the liquid phase can be described by means of the model illustrated in figure 1.

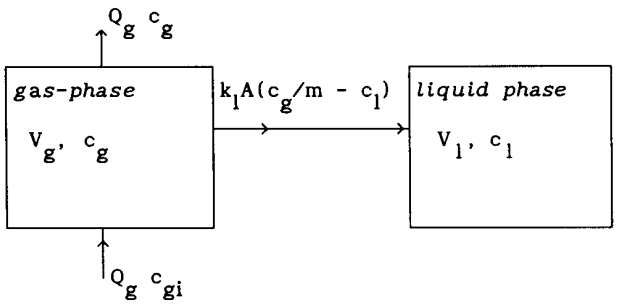

Figure 1 *Schematic view of the oxygen transport from gas-phase to liquid phase.*

In the first order model it is assumed that when the gas input is switched from nitrogen to air, the oxygen concentration in the gas-phase switches instantaneously to the oxygen concentration in the inlet gas c_{gi}. In this case c_l can be calculated from the following balance equation:

$$\frac{\partial c_l}{\partial t} = k_l a \left(\frac{c_{gi}}{m} - c_l\right) \tag{2}$$

which has got the following solution:

$$c_l(t) = \frac{c_{gi}}{m} \left(1 - \exp(-k_l a\ t)\right) \tag{3}$$

Since the measured oxygen concentration c_{lm} differs from the real oxygen concentration due to the response time τ of the oxygen probe (here τ = 5s), which can be modeled by:

$$\frac{\partial c_{lm}}{\partial t} = \frac{1}{\tau} \left(c_l - c_{lm}\right) \tag{4}$$

the mass transfer coefficient can be calculated by fitting the measured signal to the solution of equations (3) and (4):

$$c_{lm}(t) = \frac{c_{gi}}{m} \left(1 - \frac{k_l a\ \tau}{k_l a\ \tau - 1} \exp(-t/\tau) + \frac{1}{k_l a\ \tau - 1} \exp(-k_l a\ t)\right) \tag{5}$$

by means of a non-linear least squares regression method.

A.2. The second order method

The main disadvantage of the first order method is that the assumption that the oxygen concentration in the gas phase is constant throughout the experiment will lead to an increased inaccuracy when both $k_l a$ and the gas residence time are large. This problem can be solved by taking the response of the oxygen concentration in the gas-phase into account. When the gas phase is assumed to be perfectly mixed, the following balance equations can be written:

$$\frac{\partial c_g}{\partial t} = \frac{Q_g}{V_g}(c_{gi} - c_g) - k_l a \frac{V_l}{V_g}\left(\frac{c_g}{m} - c_l\right) \tag{6}$$

$$\frac{\partial c_l}{\partial t} = k_l a \left(\frac{c_g}{m} - c_l\right) \tag{7}$$

These equations can be solved by means of Laplace transformations (Van der Aart, 1989):

$$c_l(t) = \frac{c_{gi}}{m}\frac{k_l a\, Q_g}{V_g}\left(\frac{1}{r_1 r_2} + \frac{1}{r_1 - r_2}\left(\frac{1}{r_1}\exp(r_1 t) - \frac{1}{r_2}\exp(r_2 t)\right)\right) \tag{8}$$

with:

$$r_1 = \frac{1}{2}\left(-a + \sqrt{a^2 - 4b}\right) \tag{9}$$

$$r_2 = \frac{1}{2}\left(-a - \sqrt{a^2 - 4b}\right) \tag{10}$$

$$a = k_l a + \frac{Q_g}{V_g} + \frac{k_l a\, V_l}{m V_g} \tag{11}$$

$$b = \frac{Q_g}{V_g} k_l a \tag{12}$$

And for the measured oxygen concentration the following equation is found:

$$c_{lm}(t) = \frac{c_{gi}}{m} \frac{k_l a \; Q_g}{V_g} \left(\frac{1-\exp(-t/\tau)}{r_1 r_2} + \frac{1}{r_1 - r_2} \left(\frac{\exp(r_1 t) - \exp(-t/\tau)}{(r_1 \tau + 1)\; r_1} \right.\right.$$

$$\left.\left. - \frac{\exp(r_2 t) - \exp(-t/\tau)}{(r_2 \tau + 1)\; r_2} \right)\right) \qquad (13)$$

Figure 2 shows a comparison between the $k_l a$ values as measured with the first order method and as measured with the second order method. It can be seen that for low $k_l a$ the difference between the two methods is negligible, but that it is not possible to measure values larger than 0.06 s^{-1} with the first order method. Therefore all experimental $k_l a$ values in this thesis are determined by fitting (13) to the measured c_l-signal.

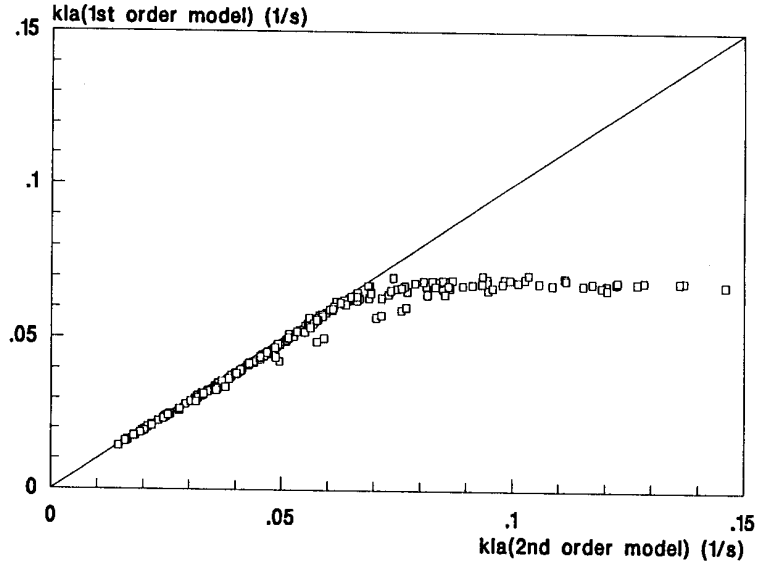

Figure 2 *Experimental $k_l a$-values as measured according to the 1st order method compared with the $k_l a$-values according to the 2nd order method, based on the same signals.*

APPENDIX B

OPTICAL FIBER PROBES

B.1. Single-point probes

In this work optical fiber probes are used for measurement of local values of the gas-holdup and the bubble size in the gas dispersion. The operating principle of such an optical probe is illustrated in figure 1. Due to differences in the refraction index, light which is send in the probe will be reflected when the probe tip is surrounded by air, whereas the light will leave the probe when it is surrounded by water. When a gas-bubble is pierced by such a probe, the resulting signal will look as in figure 2. When the signal is high, the probe is in gas. The time T the probe is in gas is determined by the bubble chord length and the bubble velocity. The rise time of the signal is, among other things, determined by the bubble velocity (fig 3). Therefore it has been tried to measure bubble velocities by means of measuring the rise time of this signal, and using this velocity and the time T for determining the bubble size. However, it turned out that this method was too inaccurate for practical use in stirred vessels.

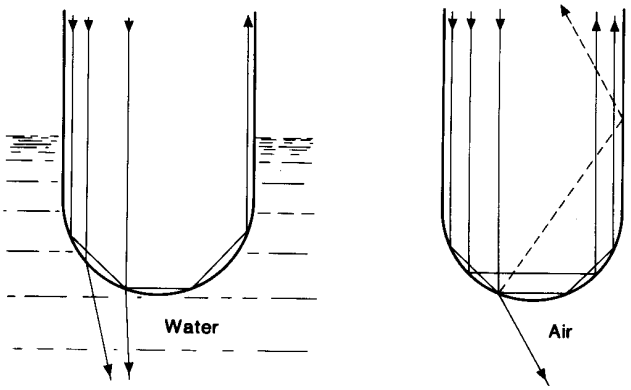

Figure 1 *Reflection and refraction of light in a fibertip surrounded by water and in a fibertip surrounded by air*

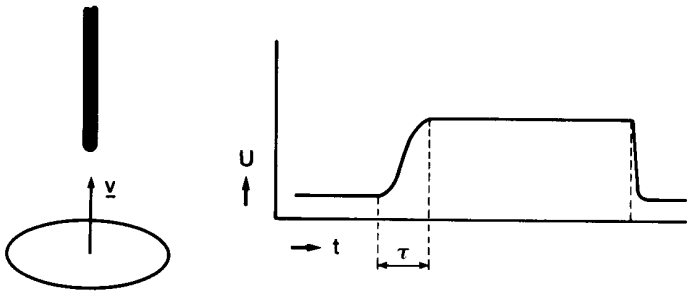

Figure 2 *Probesignal U when a bubble is pierced, τ is the rise time of the signal*

Thus, the single-point probes were used for measuring the local gas-holdup only. This was done by placing the probe in the gas-liquid dispersion, and measuring the fraction of the time the probe tip is surrounded by gas. In all cases the probe was aligned as well as possible with the main flow. This is necessary to prevent too many bubbles from bouncing away from the probe. In general the local holdup values, integrated over the vessel agreed quite well with the overall holdup as measured with an ultrasonic liquid level meter. For example with an A315 impeller at N = 10Hz and v_{sg} = 0.01m/s the measured overall holdup was 4.8% and the integrated local holdup was 4.6%. The fact that the integrated local holdup is a little lower might be caused by small bubbles which bounce from the probe tip, and which are not detected.

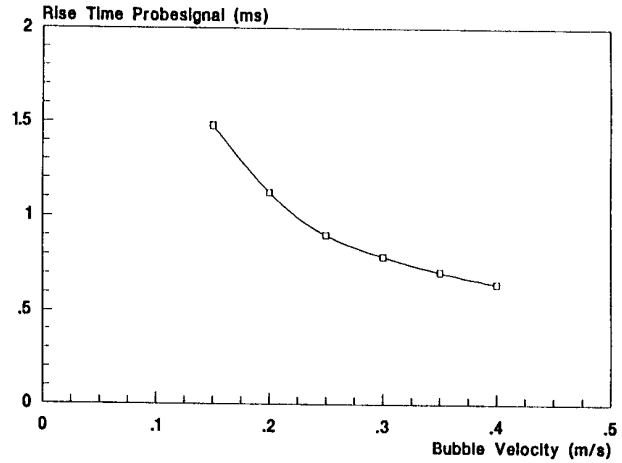

Figure 3 *Signal rise time as a function of bubble velocity.*

B.2. Four-point probes

Frijlink (1987) developed a system for the measurement of local bubble sizes, based on four-point optical probes. The aim of this probe is to select only bubbles which are pierced along the principal vertical axis. The operating principle of these probes is illustrated in figure 4.

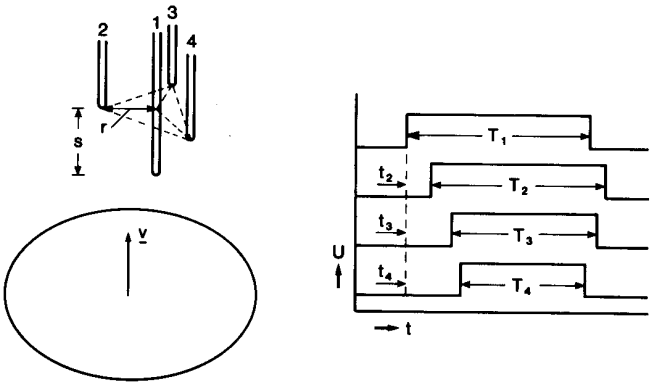

Figure 4 *The four point probe for bubble size measurements.*

When a bubble is pierced by the probe, the electronic measurement system will check whether the three delay times t_1, t_2 and t_3 are within 20% of the average pulse length. When this is true, a first approximation of the bubble velocity and the bubble diameter can be made. The bubble velocity is approximated by:

$$v = \frac{3\,S}{t_2 + t_3 + t_4} \qquad (1)$$

and the bubble diameter is approximated by:

$$d = v\,T_{max} \qquad (2)$$

Here T_{max} denotes the maximum of the four pulse length T_1, T_2, T_3 and T_4; S is the distance between the surrounding tips and the central tip. These first approximations are used for calculating a correction on v and d which takes the curvature of the bubble surface into account.

Assuming spherical bubbles, the bubble velocity v_b and the bubble diameter d_b are then given by:

$$v_b = \frac{2\,S + d - \sqrt{d^2 - 4\,r^2}}{2\,\bar{t}} \tag{3}$$

$$d_b = v_b\,T_{max} \tag{4}$$

Here r denotes the radius of the probe. A more extensive discussion of this measurement method and the signal analysis is given by Frijlink, who also showed that bubble sizes measured in this way compare very well with photographic measurements. The radius r of the probe was r = 0.6mm and the distance between the central tip and the surrounding tips was S = 1.4mm. In the present project, this probe was used to measure bubble sizes near the top surface of the vessel. In this region the bubbles were large enough to be measured by the four-point probe.

NOMENCLATURE

Symbols

a	Long axis of ellipse	(m)
a_d	Interfacial surface area	(m^{-1})
A	Surface area	(m^2)
A_b	Area of one impeller blade	(m^2)
$A_{b,\perp}$	Projected area of one impeller blade	(m^2)
b	Short axis of ellipse	(m)
B_w	Impeller blade width	(m)
c	Oxygen concentration	(kgm^{-3})
c_μ	Model constant	(-)
$c_{\varepsilon 1}$	Model constant	(-)
$c_{\varepsilon 2}$	Model constant	(-)
c_1	Model constant	(-)
c_2	Model constant	(-)
C	Impeller to bottom clearance	(m)
C_∞	Model constant	(-)
C_ω	Model constant	(-)
C_*	Model constant	(-)
C_λ	Model constant	(-)
d	Diameter	(m)
d_{hub}	Impeller hub diameter	(m)
d_s	Sparger diameter	(m)
D	Impeller swept diameter	(m)
$\mathcal{D}$	Diffusion coefficient	(m^2s^{-1})
Eo	Eötvös number	(-)
ℓ	Number of bubble collisions	($m^{-3}s^{-1}$)
$\vec{F}_s$	Slip force vector	(N)
F_T	Axial force exerted by the impeller (thrust)	(N)
Fl_l	Impeller pumping number (Q_l/ND^3)	(-)
Fl_g	Gas flow number (Q_g/ND^3)	(-)
H	Liquid height	(m)

H_i	Impeller height	(m)
$\vec{\vec{I}}$	Unit tensor	(-)
J	Particle/bubble flux	($m^{-2}s^{-1}$)
k	Turbulent kinetic energy per fluid mass	(m^2s^{-2})
k_l	Liquid side mass transfer coefficient	(ms^{-1})
k_la	Overall volumetric mass transfer coefficient	(s^{-1})
K_w	Friction coefficient	(-)
L_t	Turbulent length scale	(m)
m	Partition coefficient	(-)
n_b	Number of impeller blades (Chapter 2)	(-)
n_b	Bubble number density (Chapter 4)	(m^{-3})
$\dot{n}_{b,c/b}$	Change in bubble number density due to coalescence/breakup processes	($m^{-3}s^{-1}$)
N	Impeller rotational speed	(s^{-1})
N_b	Number of bubbles	(-)
$<\Delta p_f>$	Average pressure increase at impeller	(Pa)
$<\Delta p_b>$	The average pressure difference between the two sides of an impeller blade	(Pa)
p	Pressure	(Nm^{-2})
P	Power consumption	(W)
$\vec{\vec{P}}$	Reynolds stress production tensor	(m^2s^{-3})
P_k	Production of k by interaction with mean strain rate	(m^2s^{-3})
Po	Impeller power number ($P/\rho N^3D^5$)	(-)
Q_g	Gassing rate	(m^3s^{-1})
Q_l	Liquid flow rate	(m^3s^{-1})
r	Radial coordinate (outwards positive)	(m)
$\hat{r}$	Unit vector in radial direction	(-)
$R_{b,\perp}$	Projected blade area ratio	(-)
S	Impeller-sparger separation	(m)
S	Swirl number	(-)
S_g	Gas source	(m^3s^{-1})
Sc	Schmidt number ($\nu/\mathcal{D}$)	(-)
SR	Solidity ratio	(-)
T	Vessel diameter	(m)
u	Axial velocity (downwards positive)	(ms^{-1})
$\vec{u}$	Time-averaged velocity vector	(ms^{-1})

$\vec{u}'$	Fluctuating component of the velocity vector	(ms^{-1})
$\vec{u}_s$	Slip velocity vector	(ms^{-1})
v	Velocity	(ms^{-1})
v	Radial velocity (outwards positive)	(ms^{-1})
v_{sg}	Superficial gas velocity $(4Q_g/(\pi T^2))$	(ms^{-1})
$\langle v_{ax} \rangle$	Average axial liquid velocity out of the impeller plane	(ms^{-1})
V	Volume	(m)
V_{imp}	Impeller swept volume	(m^3)
w	Tangential velocity (with impeller positive)	(ms^{-1})
W	Baffle width	(m)
W_b	Width of impeller blade	(m)
X_c	Net efficiency of the coalescence process	(-)
z	Axial coordinate, 0 at liquid surface	(m)
$\hat{z}$	Unit vector in axial direction	(-)

Greek Symbols

α	Gas holdup	(-)
ε	Turbulent energy dissipation rate	(m^2s^{-3})
ε_{imp}	Turbulent energy dissipation rate in impeller region	(m^2s^{-3})
$\langle\varepsilon\rangle$	Average energy dissipation rate (P/V_l)	(W/m^3)
ϕ	Tangential coordinate (0° at baffle)	$(^\circ)$
η	Dynamic viscosity	(mPas)
η_e	Energetic efficiency	(-)
η_P	Pumping efficiency	(-)
η_*	Effective viscosity	(Pas)
λ_t	Transport free path	(m)
ν	Kinematic viscosity	(m^2s^{-1})
ν_t	Turbulent viscosity	(m^2s^{-1})
ρ	Density	(kgm^{-3})
σ_k	Model constant	(-)
σ_ε	Model constant	(-)
τ	Time constant oxygen probe	(s)
ω	Effective coalescence/breakup frequency	(s^{-1})

Subscripts

c	Critical, at the indirect/direct loading transition
b	Referring to bubble
d	Referring to dispersion (volume)
js	Just suspended
g	Gas, under gassed conditions or referring to gas phase
l	Referring to liquid phase
lm	Measured in liquid phase
u	Ungassed conditions
i	In inlet gas
in	At gas input
net	Referring to net particle flux
out	Leaving the vessel
∞	Referring to maximum stable bubble size

Abbreviations

ASM	Algebraic Stress Model
CFD	Computational Fluid Dynamics
DT	Disc Turbine (Rushton Turbine)
LRS	Large ring sparger
LDV	Laser Doppler Velocimetry
OTR	Oxygen Transfer Rate
PBT	Downwards pumping Pitched Blade Turbine, 6 blades at 45° blade angle
PS	Pipe sparger
QPS	Quadruple pipe sparger
RMS	Root Mean Square
RSM	Reynolds Stress Model
SRS	Small ring sparger

Vector Notation

$\vec{X}.\vec{Y} = x_i y_i$

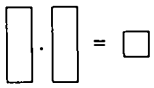

$\vec{X}\times\vec{Y} = \vec{Z}$

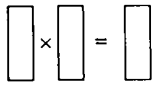

$\vec{X}\vec{Y} = \vec{\vec{Z}} \qquad z_{ij} = x_i y_j$

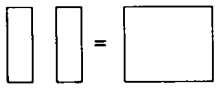

$\vec{\vec{A}}:\vec{\vec{B}} = a_{ij} b_{ji}$

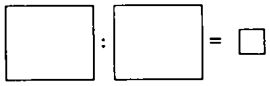

$\vec{\vec{A}}.\vec{B} = \vec{C} \qquad c_i = a_{ik} b_k$

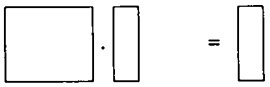

$\vec{\vec{A}}.\vec{\vec{B}} = \vec{\vec{C}} \qquad c_{ij} = a_{ik} b_{kj}$

LITERATURE

Bakker A., Van den Akker H.E.A. (1990a)
The Use of Profiled Axial Flow Impellers in Gas-Liquid Reactors
Proceedings Fluid Mixing IV, Bradford U.K., September 11-13 1990, I.Chem.E.Symposium Series No. 121, 153-166

Bakker A., Van den Akker H.E.A. (1990b)
Gas Liquid Contacting with the Lightnin A315 Impeller, Effects of Flow Pattern
AIChE Annual Meeting, Chicago, November 11-16, Session on Industrial Mixing and Scale-Up, Unpublished

Bakker A., Van den Akker H.E.A. (1991)
A Computational Study on Dispersing Gas in a Stirred Reactor
Proc. 7th Eur.Conf.Mixing, Brugge, Belgium, September 18-20, 199-207

Barnea E., Mizrahi J. (1975)
A Generalized Approach to the Fluid Dynamics of Particulate Systems, Part 2: Sedimentation and Fluidisation of Clouds of Spherical Liquid Drops
Can.J.Chem.Eng. 53, 461-469

Boysan F. (1984)
Mathematical Modelling of Cyclone Separators
Selected Topics in Two-Phase Flow, Lecture Series no. 9, Trondheim, May 25

Chapman C.M., Nienow A.W., Cooke M., Middleton J.C. (1983a)
Particle-Gas-Liquid Mixing in Stirred Vessels; Part 2: Gas-Liquid Mixing
Chem.Eng.Res.Des. 61, 82-95

Chapman C.M., Nienow A.W., Cooke M., Middleton J.C. (1983b)
Particle-Gas-Liquid Mixing in Stirred Vessels; Part 4: Mass Transfer and Final Conclusions
Chem.Eng.Res.Des. 61, 182-185.

Colenbrander G.W. (1989)
Turbulentiemodellen: Wonder- of Lapmiddel?
I^2-Procestechnologie 3, 31 (in Dutch)

Frijlink J.J. (1987)
Gassed Suspension Reactors
PhD Thesis, Delft University of Technology, The Netherlands

Frijlink J.J., Bakker A., Smith J.M. (1990)
Suspension of Solid Particles with Gassed Impellers
Chem.Eng.Sci. 45, 1703-1718

Greaves M., Barigou M. (1988)
The Internal Structure of Gas-Liquid Dispersions in a Stirred Reactor
Proc. 6th Eur.Conf. Mixing, Pavia, Italy, May 22-24, 313-320

Harvey P.S. (1980)
PhD Thesis, University of Bath, United Kingdom

Harvey P.S., Greaves M. (1982a)
Turbulent Flow in an Agitated Vessel; Part 1: A Predictive Model
Trans.I.Chem.E. 60, 195-200

Harvey P.S., Greaves M. (1982b)
Turbulent Flow in an Agitated Vessel; Part 2: Numerical Simulation and Model Predictions
Trans.I.Chem.E. 60, 201-210
Hinze J.O. (1955)
Fundamentals of the Hydrodynamic Mechanism of Splitting in Dispersion Processes
AIChE Journal 1, 289-295
Hutchings B.J., Weetman R.J., Patel B.R., (1989)
Computation of Flow Fields in Mixing Tanks with Experimental Verification
ASME Annual Meeting, San Francisco, December 10-15,
Issa R.I., Gosman A.D. (1981)
The Computation of Three-Dimensional Turbulent Two-Phase Flow in Mixer Vessels
Proc. 2nd Int.Conf. Num.Meth.Lam.Turb.Flows, Venice, Italy
Joshi J.B., Pandit A.B., Sharma M.M. (1982)
Mechanically Agitated Gas-Liquid Reactors
Chem.Eng.Sci. 37, 813-844
Kawase Y., Moo-Young M. (1990)
Mathematical Models for the Design of Bioreactors: Application of Kolmogoroff's Theory of Isotropic Turbulence
Chem.Eng.J. 43, B19-B41
Kresta S.M., Wood P.E. (1991)
Prediction of the Three-Dimensional Turbulent Flow in Stirred tanks
AIChE Journal 37, 448-460
Koen C. (1990)
Personal communication
Lally K.S. (1991)
Personal communication
Lally K.S., Post T.A. (1991)
Axial Flow Mixing Impeller Improves Bioreactor Performance
MIXING XIII, Organized by the Engineering Foundation, Banff, Canada, June 10-15, Unpublished
Laufhütte H.D., Mersmann A.B. (1985)
Dissipation of Power in Stirred Vessels
Proceedings 5th. Eur.Conf.Mixing, Wurzburg, Germany, June 10-12, 331-340
Looney M.K., Issa R.I., Gosman A.D., Politis S. (1985)
Modelling of the Turbulent Flow of Solid/Liquid Suspensions in Stirred Vessels
Fifth Int.Conf. on Mathematical Modelling, Berkeley, July 29-31
Mann R. (1986)
Gas-Liquid Stirred Vessel Mixers: Towards a Unified Theory Based on Networks-of-Zones
Chem.Eng.Res.Des. 64, 23-34
Mann R., Hackett L.A. (1988)
Fundamentals of Gas-Liquid Mixing in a Stirred Vessel: An Analysis Using Networks of Zones
Proceedings 6th. Eur.Conf.Mixing, Pavia, Italy, May 24-26, 321-328
McFarlane C. (1989)
Power Characteristics and Gas-Liquid Hydrodynamics of the Prochem Maxflo-Hydrofoil Impeller
MIXING XII, Organized by the Engineering Foundation, Potosi, Missouri, U.S.A. Unpublished

Middleton J.C., Pierce F., Lynch P.M. (1986)
Computations of Flow Fields and Complex Reaction Yield in Turbulent Stirred Reactors and Comparison with Experimental Data
Chem.Eng.Res.Des. 64, 18-22

Morsi S.A., Alexander A.J. (1972)
An Investigation of Particle Trajectories in Two-Phase Flow Systems
J. Fluid Mechanics 2, 193-208

Nagase Y., Yasui H. (1983)
Fluid Motion in a Gas-Liquid Contactor with Turbine Agitators
The Chemical Engineering Journal 27, 37-47

Nienow A.W., Konno M., Bujalski W. (1986)
Studies on Three-Phase Mixing: A Review and Recent Results
Chem.Eng.Res.Des. 64, 35-42

Nienow A.W. (1990)
Gas-Dispersion Performance in Fermenter Operation
Chemical Engineering Progress 2, 61-71

Ohba K., Yuhara T., Matsuyama H. (1986)
Simultaneous Measurements of Bubble and Liquid Velocities in Two-Phase Bubbly Flow Using Laser Doppler Velocimeter
Bulletin of JSME 29, 2487-2493

Oldshue J.Y., Post T.A., Weetman R.J., Coyle C.K. (1988)
Comparison of Mass Transfer Characteristics of Radial and Axial Flow Impellers
Proceedings 6th. Eur.Conf.Mixing, Pavia, Italy, May 22-24, 345-350

Oldshue J.Y. (1989)
Fluid Mixing in 1989
Chemical Engineering Progress 5, 33-42

Patterson G.K. (1991)
Measurements and Modelling of Flow in Gas Sparged Agitated Vessels
Proc. 7th Eur.Conf.Mixing, Brugge, Belgium, September 18-20, 209-215

Pendlebury J.M. (1985)
Kinetic Theory
Adam Hilger Ltd, Bristol, England, ISBN 0-85274-796-9

Pericleous K.A. Patel M.K. (1987)
The Modelling of Tangential and Axial Agitators in Chemical Reactors
Physico Chemico Hydrodynamics 8, 105-123

Placek J., Tavlarides L.L. (1985)
Turbulent Flows in Stirred Tanks; Part 1: Turbulent Flow in the Turbine Impeller Region
AIChE Journal 31, 1113-1120

Placek J., Tavlarides L.L., Smith G.W., Fort I. (1986)
Turbulent Flows in Stirred Tanks; Part 2: A Two Scale Model of Turbulence
AIChE Journal 32, 1771-1785

Ranade V.V., Joshi J.B. (1989a)
Flow Generated by Pitched Blade Turbines 1: Measurements Using Laser-Doppler Anemometer
Chem.Eng.Comm. 81, 197-224

Ranade V.V., Joshi J.B., Marathe A.G. (1989b)
Flow Generated by Pitched Blade Turbines 2: Simulation Using k-ε Model
Chem.Eng.Comm. 81, 225-248

Ranade V.V., Joshi J.B. (1990a)
Flow Generated by a Disc-Turbine; Part 1: Experimental
TransIChemE 60, 19-33

Ranade V.V., Joshi J.B. (1990b)
Flow Generated by a Disc-Turbine; Part 2: Mathematical Modelling and Comparison with Experimental Data
TransIChemE 60, 34-50
Rodi W. (1980)
Turbulence Models and Their Application in Hydraulics - A State of the Art Review
International Association for Hydraulic Research, Delft, The Netherlands
Salzman R.N., Webster W., Muratore G., Page K. (1988)
A New Mixer for the Chemical Process Industries
Proceedings 6th. Eur.Conf.Mixing, Pavia, Italy, May 22-24, 79-84
Smith J.M. (1985)
Dispersion of Gases in Liquids
"Mixing of Liquids by Mechanical Agitation", Eds. Ulbrecht J.J and Patterson G.K., Gordon and Breach Science Publishers, ISSN: 0734-1644, ISBN: 2-88124-112-3
Smith J.M., Warmoeskerken M.M.C.G., (1985)
Gas-Liquid Reactors with the Leeuwrik and Other Profiled Impellers
Research Proposal STW-DTN 40.0566
Trägårdh Ch. (1988)
A Hydrodynamic Model for the Simulation of an Aerated Agitated Fed-Batch Fermenter
Proc. 2nd Int.Conf.Bioreactor Fluid Dynamics, Cambridge U.K., September 21-23, 117-134
Van der Aart L.C.J. (1989)
Een Theoretisch en Experimenteel Onderzoek naar Dynamische Meetmethoden van de Volumetrische Stofoverdrachtscoefficient in een Gas-Vloeistof Dispersie
Graduation Thesis, Delft University of Technology, Dutch
Van Oossaanen (1974)
Calculation of Performance and Cavitation Characteristics of Propellers Including Effects of Non-Uniform Flow and Viscosity
Ph.D. Thesis, Delft University of Technology, The Netherlands
Van't Riet (1975)
Turbine Agitator Hydrodynamics and Dispersion Performance
Ph.D. Thesis, Delft University of Technology, The Netherlands
Van 't Riet K., Bruijn W., Smith J.M. (1976)
Real and Pseudo Turbulence in the Discharge Stream from a Rushton Turbine
Chem.Eng.Sci. 31, 407-412
Vermeulen P.E.J., Pohlmann J.W. (1980)
Ontwikkeling van de Leeuwrikschroef
Internal report MT-TNO, Ref.nr. 80-015586, Dutch
Warmoeskerken M.M.C.G., Smith, J.M. (1989)
The Hollow Blade Agitator for Dispersion and Mass Transfer
Chem.Eng.Res.Des. 67, 193-198
Warmoeskerken M.M.C.G., Speur J., Smith, J.M. (1984)
Gas-Liquid Dispersion with Pitched-Blade Turbines
Chem.Eng.Comm. 25, 11-29
Warmoeskerken M.M.C.G. (1986)
Gas-Liquid Dispersing Characteristics of Turbine Agitators
Ph.D. Thesis, Delft University of Technology, The Netherlands
Weetman R.J., Oldshue J.Y. (1986)
Power, Flow and Shear Characteristics of Mixing Impellers
Proceedings 6th. Eur.Conf.Mixing, Pavia, Italy, May 24-26, 35-42

Weetman R.J. (1989)
Mixing Apparatus
European Patent Application 89109743.8
Weetman R.J. (1989)
Mass-Transfer Mixing System Especially for Gas-Dispersion in Liquids or Liquid Suspensions
US-Patent 4882098
Wellek R.M., Agrawal A.K., Skelland A.H.P. (1966)
Shape of Liquid Drops Moving in Liquid Media
AIChE Journal 12, 854-862
Wu H., Patterson G.K. (1989)
Laser-Doppler Measurements of Turbulent Flow Parameters in a Stirred Mixer
Chem.Eng.Sci. 44, 2207-2221
Zwietering Th.N. (1958)
Suspending of Solid Particles in Liquid by Agitators
Chem.Eng.Sci. 8, 244-253